

ABSTRACT

Title of Dissertation: SURFACE PHYSICS MODELLING AND
EVALUATION OF 6H-SILICON CARBIDE
METAL-OXIDE-SEMICONDUCTOR
FIELD EFFECT TRANSISTORS
WITH EXPERIMENTAL CORROBORATION

Stephen Kirkman Powell, Doctor of Philosophy, 2003

Dissertation directed by: Professor Neil Goldsman
Department of Electrical and Computer Engineering

The relatively recent commercial availability of silicon carbide (SiC) wafers has significantly increased the possibility of electronics based on SiC metal-oxide-semiconductor field effect transistor (MOSFET) design. However, current state-of-the-art SiC MOSFETs possess interface deformities that not only severally degrade SiC MOSFET performance but also complicate the modelling of the surface scattering mechanisms, rendering the conventional modelling techniques insufficient.

At the time of this writing, little research towards developing tools that characterize the transport physics of experimentally observed SiC MOSFET behavior has been done. In this work I develop and implement a methodology capable of providing insight into the performance of this promising technology.

In order to bridge the gap between theoretical physics and real world experimentation, I have developed a simulation tool capable of solving the drift-diffusion heat flow equations specialized for SiC MOSFETs. The simulator utilizes techniques such as finite difference approximation, linear iteration, and the Smart Newton method. With this simulator I am able to determine and predict details about the surface transport that are not readily accessible using conventional experimental techniques. Using the methodology presented above, I have succeeded in developing a tool that characterizes the physical transport mechanisms indigenous to current state-of-the-art SiC MOSFETs and achieves agreement with experimental data. In short, the gap between theory and experiment has been bridged, and its results provide valuable insight into the roles of various surface scattering mechanisms, including interface trap occupation, surface roughness, and temperature effects.

SURFACE PHYSICS MODELLING AND EVALUATION OF
6H-SILICON CARBIDE METAL-OXIDE-SEMICONDUCTOR
FIELD EFFECT TRANSISTORS
WITH EXPERIMENTAL CORROBORATION

by

Stephen Kirkman Powell

Dissertation submitted to the Faculty of the Graduate School of the
University of Maryland, College Park in partial fulfillment
of the requirements for the degree of
Doctor of Philosophy
2003

Advisory Committee:

Professor Neil Goldsman, Chair/Advisor
Professor P. S. Krishnaprasad
Professor C. Martin Peckerar
Professor Omar M. Ramahi
Professor Lourdes G. Salamanca-Riba

©Copyright by
Stephen Kirkman Powell
2003

DEDICATION

To Jermaine and Stephana ... Daddy's home.

ACKNOWLEDGEMENTS

Thank you to my advisor, Professor Neil Goldman. I would also like to thank Professor Krishnaprasad, Professor Peckerar, Professor Ramahi, and Professor Salamanca-Riba for taking time out of their busy schedules in order to participate in this part of my academic journey. To my collaborators at Army Research Laboratory, thank you for your financial support and invaluable input.

TABLE OF CONTENTS

1	Introduction	1
1.1	What's Been Done Before?	2
1.2	What's to Come?	3
2	Drift-Diffusion Modelling for Silicon Carbide MOSFETs	6
2.1	Drift-Diffusion in Silicon Carbide	6
2.1.1	Poisson's Equation	7
2.1.2	Current Continuity	13
2.1.3	Boundary Conditions	32
2.2	Chapter Summary	37
3	Experimentation and Simulation of 6H-SiC MOSFETs	39
3.1	Device Design	40
3.2	Experimental Setup	41
3.3	Experimental Results	44
3.4	Simulation Process	47
3.4.1	Interface Charge Model	47
3.4.2	Methodology and Results	52

3.5	The Fixed Oxide Charge Discrepancy	56
3.6	Chapter Summary	58
4	High Temperature Modelling and Beyond	81
4.1	Heat Conduction	82
4.1.1	Thermal Conductivity	83
4.1.2	Self-Consistency of Drift-Diffusion and Heat Flow	85
4.1.3	High Temperature Modelling	86
4.2	High Temperature Results	91
4.3	Improving Surface Quality	93
4.4	Scalability of SiC MOSFETs	99
4.5	Chapter Summary	100
5	Numerical Methods for Drift-Diffusion Heat Flow Simulation in SiC MOS-	
	FETs	129
5.1	Simulation Flow	130
5.1.1	Phase One - Scoping the Device	130
5.1.2	Phase Two - The Vectorized Gauss-Seidel Engine	131
5.1.3	Phase Three - The Smart Newton Engine	133
5.1.4	Phase Four - Calculation of Current and Temperature	135
5.2	Discretization of Equations	136
5.3	Numerical Methods	142
5.4	Chapter Summary	160

6	Summary and Closing Remarks	168
6.1	The Method Behind the Madness	168
6.2	SiC MOSFET Characterization	169
6.3	Closing Remarks and What's Left to Do	171
	REFERENCES	172

LIST OF FIGURES

2.1	MOSFET Boundaries	38
3.1	Device profile for 6H-SiC MOSFETs studied in this work	59
3.2	Interface trap density of states profile and electron Fermi distribution	60
3.3	Product of interface trap density of states and electron Fermi distri- bution	61
3.4	Log plot of I_D vs. V_{GS} for device A1 at room temperature	62
3.5	Linear plot of I_D vs. V_{GS} for device A1 at room temperature	63
3.6	I_D vs. V_{DS} for device A1 at room temperature	64
3.7	Log plot of I_D vs. V_{GS} for device A2 at room temperature	65
3.8	Linear plot of I_D vs. V_{GS} for device A2 at room temperature	66
3.9	Linear plot of I_D vs. V_{DS} for device A2 at room temperature	67
3.10	Log plot of I_D vs. V_{GS} for device A3 at room temperature	68
3.11	Linear plot of I_D vs. V_{GS} for device A3 at room temperature	69
3.12	I_D vs. V_{DS} for device A3 at room temperature	70
3.13	Log plot of I_D vs. V_{GS} for device B1 at room temperature	72
3.14	Linear plot of I_D vs. V_{GS} for device B1 at room temperature	73
3.15	I_D vs. V_{DS} for device B1 - room temperature	74

3.16	Log plot of I_D vs. V_{GS} for device B2 at room temperature	75
3.17	Linear plot of I_D vs. V_{GS} for device B2 at room temperature	76
3.18	I_D vs. V_{DS} for device B2 at room temperature	77
3.19	Log plot of I_D vs. V_{GS} for device B3 at room temperature	78
3.20	Linear plot of I_D vs. V_{GS} for device B3 at room temperature	79
3.21	I_D vs. V_{DS} for device B3 at room temperature	80
4.1	I_D vs. V_{GS} for device A3 - various temperatures	102
4.2	I_D vs. V_{GS} for device A3 - various temperatures, linear scale	102
4.3	I_D vs. V_{DS} for device A3 - 100 Celsius	103
4.4	I_D vs. V_{DS} for device A3 - 200 Celsius	103
4.5	I_D vs. V_{GS} for device A3 - various temperatures with corrected v_{sat}	104
4.6	I_D vs. V_{DS} for device A3 - 100 Celsius with corrected v_{sat}	105
4.7	I_D vs. V_{DS} for device A3 - 200 Celsius with corrected v_{sat}	105
4.8	I_D vs. V_{GS} for $50\mu m$ by $4\mu m$, device C1 - room temperature	106
4.9	I_D vs. V_{DS} for $50\mu m$ by $4\mu m$, device C1 - room temperature	106
4.10	I_D vs. V_{GS} for $50\mu m$ by $4\mu m$, device C1 - 100 Celsius	107
4.11	I_D vs. V_{DS} for $50\mu m$ by $4\mu m$, device C1 - 100 Celsius	107
4.12	I_D vs. V_{GS} for $50\mu m$ by $4\mu m$, device C1 - 200 Celsius	108
4.13	I_D vs. V_{DS} for $50\mu m$ by $4\mu m$, device C1 - 200 Celsius	108
4.14	I_D vs. V_{GS} for $50\mu m$ by $4\mu m$, device C1 - various temperatures	109
4.15	I_D vs. V_{DS} for $50\mu m$ by $4\mu m$, device C1 - various temperatures	109
4.16	Occupied Interface Trap Density, device C1 - various temperatures	110

4.17 I_D vs. V_{GS} for $50\mu m$ by $4\mu m$, device C2 - room temperature, linear scale	112
4.18 I_D vs. V_{DS} for $50\mu m$ by $4\mu m$, device C2 - room temperature	112
4.19 I_D vs. V_{GS} for $50\mu m$ by $4\mu m$, device C3 - room temperature, linear scale	113
4.20 I_D vs. V_{DS} for $50\mu m$ by $4\mu m$, device C3 - room temperature	113
4.21 I_D vs. V_{GS} for $50\mu m$ by $4\mu m$, device C4 - room temperature, linear scale	114
4.22 I_D vs. V_{DS} for $50\mu m$ by $4\mu m$, device C4 - room temperature	114
4.23 I_D vs. V_{GS} for $50\mu m$ by $4\mu m$, device C1 with improved surface roughness, $V_{DS} = 0.25V$ - room temperature, linear scale	116
4.24 I_D vs. V_{DS} for $50\mu m$ by $4\mu m$, device C1 with improved surface roughness, $V_{GS} = 6V$ - room temperature	116
4.25 I_D vs. V_{GS} for $50\mu m$ by $4\mu m$, device C4 with improved surface roughness, $V_{DS} = 0.25V$ - room temperature, linear scale	117
4.26 I_D vs. V_{DS} for $50\mu m$ by $4\mu m$, device C4 with improved surface roughness, room temperature	117
4.27 I_D vs. V_{DS} for $50\mu m$ by $4\mu m$, device C4 with improved surface roughness - 100 Celsius	118
4.28 I_D vs. V_{DS} for $50\mu m$ by $4\mu m$, device C4 with improved surface roughness - 200 Celsius	118

4.29 I_D vs. V_{DS} for $50\mu m$ by $4\mu m$, device C4 with improved surface roughness - Various Temperature	119
4.30 I_D vs. V_{GS} for $50\mu m$ by $4\mu m$, Comparison of surface qualities - room temperature	120
4.31 Initial Doping Profile for $50\mu m$ by $1\mu m$ device	122
4.32 I_D vs. V_{GS} for $50\mu m$ by $1\mu m$ - room temperature, linear scale . . .	123
4.33 I_D vs. V_{DS} for $50\mu m$ by $1\mu m$ - room temperature	123
4.34 I_D vs. V_{GS} for $50\mu m$ by $0.5\mu m$ - room temperature, Linear Scale . .	124
4.35 I_D vs. V_{GS} for $50\mu m$ by $0.25\mu m$ - room temperature, Linear Scale .	125
4.36 I_D vs. V_{GS} for $50\mu m$ by $0.5\mu m$ with improved surface roughness - room temperature, linear scale	126
4.37 I_D vs. V_{DS} for $50\mu m$ by $0.5\mu m$ with improved surface roughness - room temperature	126
4.38 I_D vs. V_{GS} for $50\mu m$ by $0.25\mu m$ with improved surface roughness - room temperature, linear scale	127
4.39 I_D vs. V_{DS} for $50\mu m$ by $0.25\mu m$ with improved surface roughness - room temperature	127
4.40 I_D vs. V_{GS} for $50\mu m$ by $1\mu m$, $0.5\mu m$, and $0.25\mu m$ - room temperature, linear scale	128
4.41 I_D vs. V_{DS} for $50\mu m$ by $1\mu m$, $0.5\mu m$, and $0.25\mu m$ - room temperature	128
5.1 Drift-diffusion heat flow simulation flow chart	161
5.2 Initializing the simulator - Phase 1	162

5.3	Vectorized Gauss-Seidel Engine - Phase 2	163
5.4	Update Flow	164
5.5	Smart Newton Engine Flow - Phase 3	165
5.6	Current Calculation and Heat Flow - Phase 4a	166
5.7	Terminating the Simulation - Phase 4b	167

LIST OF TABLES

2.1	Low-field Bulk Mobility Parameters for 6H- and 4H-Silicon Carbide Using a Caughey-Thomas Based Model	22
2.2	Interface Charge Density Mobility Parameters for 6H- and 4H-Silicon Carbide MOSFETs	25
2.3	Theoretical Surface Phonon Parameters for 6H and 4H-Silicon Car- bide MOSFETs	27
2.4	Theoretical Thornber High Field Parameters for 6H- and 4H-Silicon Carbide	30
3.1	Dimensions for Cree Research 6H-SiC MOSFETs studied in this work	40
3.2	Experimentally extracted effective electron channel mobilities for set A, $V_{DS} = 0.25V$	45
3.3	Experimentally extracted effective electron channel mobilities for set B, $V_{DS} = 0.25V$	45
3.4	Experimental charge density values of set A	46
3.5	Experimental charge density values of set B	46
3.6	Modelling parameters for set A devices	55
3.7	Modelling parameters for set B devices	56

3.8	Experimental and simulated values of N_f for set A	57
3.9	Experimental and simulated values of N_f for set B	57
4.1	Bandgap model values for 6H- and 4H-silicon carbide	87
4.2	Model values for MOSFETs of set C	94
4.3	Model values for MOSFETs of set C (continued)	94

Chapter 1

Introduction

The relatively recent commercial availability of SiC wafers has significantly increased the possibility of electronics based on silicon carbide (SiC) metal-oxide-semiconductor field effect transistor (MOSFET) design. As with silicon (Si), silicon dioxide (SiO₂) can now be grown on a silicon carbide substrate, thus enabling the fabrication of SiC MOSFET technology. By analogy with Si MOSFETs, the realization of SiC MOSFETs provides the potential for extending the microelectronic revolution to high power and high temperature applications (exceeding the 70 degree Celsius limit of most Si based integrated circuits). However, as was the case with early Si MOSFETs, current state-of-the-art SiC MOSFETs have SiO₂ interfaces which are subject to a number of deformities including high concentrations of localized surface traps (averages on the order of $10^{12} \text{ cm}^{-2} \text{ eV}^{-1}$). The presence of these surface deformities not only severely degrades SiC MOSFET performance but also complicates the modelling of the surface scattering mechanisms, rendering the conventional modelling techniques insufficient. Phenomena of particular concern include the effects of interface traps and interface roughness (also called surface roughness) scattering, as well as temperature induced performance degradation. In

order to further develop SiC MOS technology, research towards developing tools that characterize the physics of SiC MOSFET operation, particularly the deformities associated with the SiC/SiO₂ interface, must be done. It is my goal to design and implement a methodology capable of providing insight into the performance of this relatively young technology.

1.1 What's Been Done Before?

Until this work[1] there has not been a rigorous investigation attempting to link both the theoretical transport physics and experimental device performance of SiC MOSFETs. Physics based simulations of deep submicron 4H-SiC MOSFETs have been presented by Dubaric *et al.* [2], but this effort assumes that there are no interface charges at the semiconductor/oxide interface. However, experimental work, in addition to my own finding conclude that the surface charge significantly contributes to the observed device performance. Simulations comparing the device performance of β -SiC and Si have been performed by Roldán *et al* [3], and unlike the simulations of the novel devices in [2], Roldán *et al.* includes the effects of a net interface charge. However, their interface trap model is not energy dependent. I will show later in this work that energy dependent modelling of the interface trap occupation is indeed important and must be included in order to properly characterize the MOS surface. In addition, these works have not produced results that are in agreement with experimental data, but I have accomplished this. Other researchers have focused their attention on modelling future high power MOSFETs

[4, 5]. However, in order to yield surface mobility values which are in agreement with experimental data of state-of-the-art SiC MOSFETs, parameters in their models are adjusted without any physical justification, so a description of the transport physics is lost.

Due to the unpredicted poor performance of SiC enhancement mode MOSFETs, much research has centered around the study of the SiC/SiO₂ interface and its characteristics [6, 7, 8, ?, 9, 10, 11]. It is my goal to first replicate these experimental findings then use my validated model to predict the performance of next and future generation silicon carbide MOSFETs. Experimentalists have attempted to describe MOSFET surface transport by using high level analytical models to extract effective mobility values [12, 13, 14, 15, 16, 17, 18], but these high level models cannot distinguish among the various scattering processes inherent to the mobility, nor can they quantify the behavior of the mobility at points along the channel. Furthermore, they give no insight into the impact of quantities such as electron concentration, electrostatic potential, lattice heating, and carrier generation on the MOSFET transport. Using the methodology described in this dissertation, I provide a tool capable of providing the information that the above mentioned efforts do not.

1.2 What's to Come?

In order to obtain the most liberty, it is necessary for me to develop a simulation tool that is tailored towards handling the numerical complexities encountered

when modelling wide bandgap (WBG) materials like SiC and the complexities of surface transport complexities inferred from experimental data. The drift-diffusion equations, including all material characteristics and transport models specialized for SiC MOSFETs, are presented in the next chapter. The details of the numerical translation of the analytical drift-diffusion heat flow set and the implementation for solving these equations are discussed in chapter 5.

To my knowledge, no drift-diffusion based simulator has been used to match experimental data while maintaining the clarity of the underlying surface transport physics of the SiC MOSFET. So, I investigate the correctness of my simulator by using it to match experimental data. Matching of experimental data will serve as a calibration technique from which I will extract characteristics of the experiment devices. As of this writing, no other work has been done to achieve this specific task. The details of this process are contained in chapter 3.

In order to make confident predictions about the future performance capabilities of SiC MOSFETs, I must first calibrate my simulation tool to existing experimental data. Once I have obtained a model that is representative of the experimental data, I predict the performance of future SiC MOSFETs. By using the simulator in this manner, I have produced a drift-diffusion based technology computer aided design (TCAD) tool capable of aiding in the design of next generation SiC MOSFETs. This investigation includes room temperature and elevated temperature performance of SiC MOSFETs with improved surface quality. Also investigated is the scalability of SiC MOSFETs for the purpose of large scale inte-

grated (LSI) circuit design. These results are presented in chapter 4 of this work.

Summarizing, a simulation tool has been developed, calibrated by experimental data, and used to give further insight into the design and performance of current state-of-the-art and future generation SiC MOSFETs. Knowledge gained and contributions include high temperature, surface defect degradation, and submicron device performance characterization of state-of-the-art and future generation SiC MOSFETs.

Drift-Diffusion Modelling for Silicon Carbide MOSFETs

In this chapter I will present the drift-diffusion model which serves as the basis for all numerical simulations of silicon carbide (SiC) metal-oxide-semiconductor field effect transistor (MOSFET) devices presented in this work. I begin by reviewing the drift-diffusion equations and all of the scattering mechanisms associated with drift-diffusion. I also present specifics concerning drift-diffusion based modelling of SiC MOSFETs. Special emphasis is placed on the discussion about mobility modelling for drift-diffusion transport.

2.1 Drift-Diffusion in Silicon Carbide

The drift-diffusion equations, consisting of Poisson's equation, the current continuity equation for electrons, and the current continuity equation for holes, serve as the basic building blocks for semiconductor electron device modelling and can be derived directly from Maxwell's equations for electromagnetic radiation and the Boltzmann transport equation of kinetic theory [19], [20]. In this section, I discuss in detail the various aspects of the drift-diffusion model and, more impor-

tantly, how this model is used to help characterize the current status of a relatively new semiconductor device - the silicon carbide MOSFET. Using the drift-diffusion model, I am able to extract physical surface attributes of state-of-the-art devices in an effort to understand the current condition of these devices and the realizable potential of next generation SiC MOSFETs.

2.1.1 Poisson's Equation

The first of these equations, Poisson's equation, relates electrostatic potential, ϕ , to the net charge density, ρ . Poisson's equation is given by the following:

$$\vec{\nabla} \cdot (\epsilon \vec{\nabla} \phi) = -\rho. \quad (2.1)$$

ρ is the net charge density and ϵ is the dielectric permittivity of the material in which the charge is present. Within the semiconductor lattice bulk, the charged particle concentration consist of negatively charged electron concentrations (n), positively charged hole concentrations (p), and ionized impurity concentrations caused by activated dopant atoms (C). The ionized impurities can be further separated into positively charged donors concentrations (N_d^+) and negatively charged acceptor concentrations (N_a^-). Substituting these values in for the net charge concentration ρ , Poisson's equation takes on the following form:

$$\vec{\nabla} \cdot (\epsilon \vec{\nabla} \phi) = q(n - p - C) \quad (2.2)$$

where q is the charge magnitude of a single electron and

$$C = N_d^+ - N_a^- . \quad (2.3)$$

Inclusion of the ionized impurity concentrations is sometimes approximated by setting the values for ionized donor and acceptor concentrations equal to the initial deposited values. However, calculations and experiments on the thermal excitation energy of donors and acceptors in silicon carbide show that knowledge of the ionized impurity concentration, as opposed to only the concentration of the impurity atoms initially deposited, is crucial when characterizing junction barrier heights. This is important since the fabrication and functionality of semiconductor devices is based on the ability to construct and manipulate semiconductor barrier heights. Calculating incomplete ionization in SiC MOSFETs begins with Shockley's relationship between the initial doping concentration and ionized doping concentration [21]. Specifically,

$$N_d^+(\varepsilon_f, \vec{r}) = \frac{N_d(\vec{r})}{1 + g_d \exp\left(\frac{\varepsilon_f - \varepsilon_d}{k_B T}\right)} \quad (2.4)$$

for donors and

$$N_a^-(\varepsilon_f, \vec{r}) = \frac{N_a(\vec{r})}{1 + g_a \exp\left(\frac{\varepsilon_a - \varepsilon_f}{k_B T}\right)} \quad (2.5)$$

for acceptors. N_d and N_a are the initial donor and acceptor concentrations, respectively, while N_d^+ and N_a^- are the ionized (activated) donor and acceptor concentrations, respectively. g_d is the ground-state degeneracy of donor impurity levels,

and g_a is the ground-state degeneracy of acceptor impurity levels. Finally, ε_d is the inner-gap energy level for donor impurity states; likewise, ε_a is for acceptors. ε_f is the Fermi energy value. k_B and T are the Boltzmann constant and ambient temperature, respectively.

Since the drift-diffusion model is expressed in terms of real space as opposed to energy space, translation of the above expression to *real-space only* is required. By using Boltzmann statistics, this translation is possible. For non-degenerate semiconductor material at thermal equilibrium (by non-degenerate I mean that a particular carrier concentration is much less than its respective effective density of states value) the relationship between the electron concentration, hole concentration, and the inner-gap energy level is given by the following equations:

$$n(\varepsilon_f) = N_c \exp\left(\frac{\varepsilon_f - \varepsilon_c}{k_B T}\right) \quad (2.6)$$

and

$$p(\varepsilon_f) = N_v \exp\left(\frac{\varepsilon_v - \varepsilon_f}{k_B T}\right) \quad (2.7)$$

where N_c is the conduction band effective density of states, and ε_c is the conduction band minimum. Similarly, N_v is the valence band effective density of states, and ε_v is the valence band maximum.

Taking the expression for ionized donor concentration and expanding the exponential term in the denominator to include the conduction band minimum, ε_c . Equation 2.4 becomes

$$N_d^+(\varepsilon_f, \vec{r}) = \frac{N_d(\vec{r})}{1 + g_d \exp\left(\frac{\varepsilon_f - \varepsilon_c}{k_B T}\right) \exp\left(\frac{\varepsilon_c - \varepsilon_d}{k_B T}\right)}. \quad (2.8)$$

Dividing Equation 2.6 by the conduction band effective density of states and substituting the new expression into Equation 2.8, I obtain

$$N_d^+(\varepsilon_f, \vec{r}) = \frac{N_d(\vec{r})}{1 + g_d \frac{n(\varepsilon_f)}{N_c} \exp\left(\frac{\Delta_d}{k_B T}\right)} \quad (2.9)$$

where $\Delta_d = \varepsilon_c - \varepsilon_d$ is a fixed value equal to the thermal ionization energy of the donor impurity atom.

The Fermi level is a byproduct of thermal equilibrium. Consequently, it is improper to speak of a Fermi level when stimulus, such as a voltage or current, is being applied to disturb the thermal equilibrium of the semiconductor. To handle these nonequilibrium cases, two related parameters called quasi-Fermi levels were introduced. The quasi-Fermi levels for electrons and hole are defined in such a way that maintain the relationship between the intrinsic carrier concentration and the electron and hole concentrations, respectively. Specifically, the the quasi-Fermi levels are defined as

$$\varepsilon_{f_n}(\vec{r}) = \varepsilon_i + k_B T \ln \frac{n(\vec{r})}{n_i} \quad (2.10)$$

for electrons and

$$\varepsilon_{f_p}(\vec{r}) = \varepsilon_i - k_B T \ln \frac{p(\vec{r})}{n_i} \quad (2.11)$$

for holes. $\varepsilon_{f_n}(\vec{r})$ and $\varepsilon_{f_p}(\vec{r})$ are the position dependent electron and hole quasi-Fermi levels for electrons and holes, respectively, and ε_i is the intrinsic Fermi level. Additionally, dividing by the electron charge ($-q$), the following expressions are obtained for the electron and hole quasi-Fermi potential, respectively:

$$\psi_n(\vec{r}) = \phi_i - \frac{k_B T}{q} \ln \frac{n(\vec{r})}{n_i} \quad (2.12)$$

for electrons and

$$\psi_p(\vec{r}) = \phi_i + \frac{k_B T}{q} \ln \frac{p(\vec{r})}{n_i} \quad (2.13)$$

where

$$\phi_i = -\frac{\varepsilon_i}{q}. \quad (2.14)$$

It is a well known result that, for non-degenerate material, the Maxwellian distribution of electrons given in Equation 2.6 can be expressed in terms of the electrostatic potential and the electron quasi-Fermi potential and leads to the following spacial relationship among the electron concentration, the electrostatic potential, and the electron quasi-Fermi potential:

$$n(\vec{r}) = n_i \exp\left(\frac{\phi(\vec{r}) - \psi_n(\vec{r})}{V_T}\right) \quad (2.15)$$

where n_i is the intrinsic electron-hole pair concentration, $\psi_n(\vec{r})$ is the quasi-Fermi potential, and V_T is the thermal voltage given by $V_T = \frac{k_B T}{q}$. Substituting the expression in terms of energy (Equation 2.6) with the real space expression (Equation 2.15), I obtain the equation given below:

$$N_d^+(\vec{r}) = \frac{N_d(\vec{r})}{1 + g_d \frac{n(\vec{r})}{N_c} \exp\left(\frac{\Delta_d}{k_B T}\right)}. \quad (2.16)$$

A similar expression is obtained for ionized acceptor atoms where Δ_a is the thermal ionization energy of acceptor impurities.

$$N_a^-(\vec{r}) = \frac{N_a(\vec{r})}{1 + g_a \frac{p(\vec{r})}{N_v} \exp\left(\frac{\Delta_a}{k_B T}\right)}. \quad (2.17)$$

Because of the hexagonal lattice structure of 4H- and 6H-silicon carbide, impurity atoms can occupy one of several different types of sites in the crystal. For 6H-SiC, the dopant at a specific location may exist at the hexagonal site (h) or either cubic site (k_1, k_2). To obtain the ionized doping concentration as a function of position the average contribution from the three sites is used

$$N_d^+(\vec{r}) = \frac{\delta_h N_d(\vec{r})}{1 + g_d \frac{n(\vec{r})}{N_c} \exp\left(\frac{\Delta_d^h}{k_B T}\right)} + \frac{\delta_{k_1} N_d(\vec{r})}{1 + g_d \frac{n(\vec{r})}{N_c} \exp\left(\frac{\Delta_d^{k_1}}{k_B T}\right)} + \frac{\delta_{k_2} N_d(\vec{r})}{1 + g_d \frac{n(\vec{r})}{N_c} \exp\left(\frac{\Delta_d^{k_2}}{k_B T}\right)} \quad (2.18)$$

where δ_x is the probability of a site being ionized at the x^{th} site and Δ_d^x is the ionization energy for that site. In 6H-SiC $\delta_h = \delta_{k_1} = \delta_{k_2} = \frac{1}{3}$. Likewise, in 4H-

SiC, the dopant at a specific location may exist at the hexagonal site or the cubic. Similar to the 6H-SiC scenario, the ionized doping concentration as a function of position uses the average contribution from the two sites ($\delta_h = \delta_k = \frac{1}{2}$)

$$N_d^+(\vec{r}) = \frac{\delta_h N_d(\vec{r})}{1 + g_d \frac{n(\vec{r})}{N_c} \exp\left(\frac{\Delta_d^h}{k_B T}\right)} + \frac{\delta_k N_d(\vec{r})}{1 + g_d \frac{n(\vec{r})}{N_c} \exp\left(\frac{\Delta_d^k}{k_B T}\right)}. \quad (2.19)$$

Values for site ionization energy are given in [22]. A similar expression is applicable for acceptors. These expressions for ionized dopants are inserted into the Poisson equation and the bulk mobility model which is discussed later in this chapter. It is worth noting that the inclusion of incomplete ionization in the Poisson equation makes it nonlinear in the variables n and p , and thus considerably more complicated to solve.

2.1.2 Current Continuity

The current continuity equation for electrons, which the divergence of particle current density to its respective time varying charge concentration and net particle generation, is given by

$$q \frac{\partial n}{\partial t} = \vec{\nabla} \cdot \vec{J}_n - q(R_n - G_n). \quad (2.20)$$

The analogous expression for holes is given by

$$-q \frac{\partial p}{\partial t} = \vec{\nabla} \cdot \vec{J}_p + q(R_p - G_p). \quad (2.21)$$

\vec{J}_n and \vec{J}_p are the net electron and hole current densities, respectively, while R_n and R_p and G_n and G_p are the net recombination and generation rates for both electrons and holes, respectively. The current continuity equations simply state that total current flow into or out of a volume of space is equal to the time varying charge density within that volume plus any additions generation at charge generation or recombination that may occur.

Drift and Diffusion

In order to understand the nature of carrier transport within the context of the drift-diffusion model, two separate processes must be considered - carrier drift and diffusion. The contribution of carrier transport due to drift velocities is described by the following:

$$\vec{J}_{n_{drift}} = -qn\vec{v}_n \quad (2.22)$$

where \vec{v}_n is the average velocity of electrons due to an applied electric field. Furthermore, this velocity can be expressed in terms of electron mobility, μ_n , and applied electric field, \vec{E} ,

$$\vec{v}_n = -\mu_n\vec{E}. \quad (2.23)$$

The random motion of electrons in the semiconductor causes electrons to migrate from a position of high concentration to a position of low concentration. This process is called diffusion. The diffusion component of carrier transport is

due to gradients in the electron concentration throughout the semiconductor and is described by the following:

$$\vec{J}_{n_{diff}} = q\nabla(nD_n). \quad (2.24)$$

D_n is the electron diffusion coefficient and can be related to the electron mobility using the Einstein relation:

$$D_n = \mu_n \frac{k_B T}{q} \quad (2.25)$$

where T is the temperature and k_B is Boltzmann's constant.

Combining both drift and diffusion components, the total expression for electron carrier transport is given by

$$\vec{J}_{n_{total}} = \vec{J}_{n_{drift}} + \vec{J}_{n_{diff}} = qn\mu_n\vec{E} + q\vec{\nabla}(nD_n), \quad (2.26)$$

and a similar expression for hole carrier transport is given by

$$\vec{J}_{p_{total}} = \vec{J}_{p_{drift}} + \vec{J}_{p_{diff}} = qp\mu_p\vec{E} - q\vec{\nabla}(pD_p), \quad (2.27)$$

where the hole diffusion coefficient D_p equals $\mu_p \frac{k_B T}{q}$; μ_p is the hole mobility, k_B is Boltzmann's constant, and T is temperature.

Using the analytical definition of electrostatic potential, $\vec{E} = -\vec{\nabla}\phi$, and substituting it appropriately into the equations, the drift-diffusion equation set is given by

$$\vec{\nabla} \cdot (\epsilon \vec{\nabla} \phi) = q(n - p - C) \quad (2.28)$$

$$q \frac{\partial n}{\partial t} = \vec{\nabla} \cdot \vec{J}_n - q(R_n - G_n) \quad (2.29)$$

$$-q \frac{\partial p}{\partial t} = \vec{\nabla} \cdot \vec{J}_p + q(R_p - G_p) \quad (2.30)$$

where current densities are defined as

$$\vec{J}_n = -qn\mu_n \vec{\nabla} \phi + q\vec{\nabla} (D_n n) \quad (2.31)$$

$$\vec{J}_p = -qp\mu_p \vec{\nabla} \phi - q\vec{\nabla} (D_p p). \quad (2.32)$$

It is apparent from the equations given above that recombination, generation, and mobility play important roles in carrier transport physics of the drift-diffusion model. In the following, I spend some time describing these transport phenomena and the modelling used to describe their physical behavior.

Recombination and Generation

For this work bulk recombination mechanisms due to both trap centers (Shockley-Read-Hall) and direct particle recombination (Auger) are modelled. The generation of free particles due to avalanche generation, specifically impact ionization generation, are also included.

Shockley-Read-Hall Recombination Rate Capture and emission of holes and electrons by traps that reside in the mid-band energy zone is modelled using the well-known Shockley-Read-Hall (SRH) representation for recombination given by

$$R^{SRH} = \frac{np - n_i^2}{\tau_p(n + n_i) + \tau_n(p + n_i)} \quad (2.33)$$

where τ_n and τ_p are the minority carrier lifetimes of electrons and holes, respectively.

Lifetimes as a function of doping are given by the following equation:

$$\tau_{n,p} = \frac{\tau_{no,po}}{1 + \left(\frac{N_d^+ + N_a^-}{N_{n,p}^{ref}} \right)^{\alpha_{n,p}}}, \quad (2.34)$$

where $\tau_{no,po}$ is the intrinsic minority carrier lifetime, $\gamma_{n,p}$, $N_{n,p}^{ref}$, and $\alpha_{n,p}$ are empirical modelling parameters.

By examining the SRH expression for trap related recombination, it is evident that the recombination process is mainly a function of minority carrier lifetime. For example, let us assume that we are given a slab of n-type semiconductor material. If we apply a voltage to this slab and measure the current going through the material, the following conditions, in conjunction with the mass action law, are true:

$$n \gg p \quad (2.35)$$

$$np \gg n_i^2 \quad (2.36)$$

and

$$\tau_n \sim \tau_p \quad (2.37)$$

where n and p are the electron and hole concentrations, respectively, and n_i is the intrinsic electron-hole pair concentration. For the third condition, $\tau_n \sim \tau_p$, I mean that the carrier lifetimes differ by no more than a few orders of magnitudes.

Applying the aforementioned conditions to the SRH recombination model, we find that the expression simplifies to the following:

$$R^{SRH'} = \frac{p}{\tau_p}. \quad (2.38)$$

Though this result is not revolutionary, it does give valuable insight into one of the potential benefits of silicon carbide based majority carrier devices. Using the mass action law, we find that under thermal equilibrium conditions, the following must be true:

$$np = n_i^2. \quad (2.39)$$

Substituting reasonable values for n-type doping (10^{18} donor atoms per cubic centimeter) and intrinsic carrier concentration (depending on the poly-type, the intrinsic carrier concentration of SiC can vary by several orders of magnitude), we find that the hole concentration in the slab is approximately equal to 10^{-30} holes per cubic centimeter. Even with the addition of new holes due to low-level injection, this value will most likely not exceed 10^{-20} cm^{-3} . This finding shows that we need

10^{20} cm^3 of our n-type slab to observe the presence of one hole. Consequently, our material is most likely hole-free, so there is virtually no SRH recombination. So, for a silicon carbide majority carrier device such as our n-type slab, more electrons remain *alive* for transport due to the absence of SRH recombination.

Auger Recombination Rate Due to the indirect band-gap characteristic of silicon carbide, recombination of conduction band electrons and valence band holes without the intervention of some other lattice interaction is unlikely and therefore infrequent. However, for the sake of completeness, this direct recombination, too, is included. In the direct recombination process, a free electron in the conduction band combines with a free hole in the valence band, and the pre-combined net momentum of the two particle system is carried off by a third free particle which can be an electron or hole. Modelling of this type of recombination is done by using the Auger model given by

$$R^{Auger} = (np - n_i^2) (C_n n + C_p p) \quad (2.40)$$

where $C_{n(p)}$ is the coefficient representing interactions in which the remaining carrier is an electron (hole). Extracted and derived values for these recombination models in silicon carbide are found in [23].

Impact Ionization Generation Some carriers in the devices may reach very high transport speeds. These high-speed particles are also high in energy, and this energy may contribute to the generation of excess electron-hole pairs. The

generation occurs when the high energy particle collides with a bonded particle resulting in one additional free electron and one additional free hole. This type of generation is referred to as avalanche or impact ionization generation. Impact ionization models for each semiconductor material vary slightly, but most models have the basic form of [24]

$$G^{II} = \frac{1}{q} \left(\alpha_n |\vec{J}_n| + \alpha_p |\vec{J}_p| \right) \quad (2.41)$$

$$(2.42)$$

where

$$\alpha_{n,p} = \alpha_{n,p}^{\infty} \exp \left(\frac{-b_{n,p}}{|\vec{E}|} \right). \quad (2.43)$$

G^{II} is the net impact ionization generation rate, $\alpha_{n(p)}$ is the per unit length generation coefficient for electrons (holes), and $b_{n(p)}$ is the electric field at which impact ionization generation becomes significant.

Mobility in SiC MOSFETs

In this section I present a mobility model for silicon carbide (SiC) metal-oxide-semiconductor field effect transistors (MOSFETs) in order to analyze and characterize the effects of various scattering mechanisms on device performance. To achieve this I build on the work of previous investigators who studied electron transport in bulk semiconductors including silicon MOSFETs[25, 26, 27]. I separate the overall SiC MOSFET mobility into a high-field component ($\mu_{h,f}$), and a low-field

component (μ_{lf}) then divide the low-field mobility into effects that are due to: 1) low-field bulk interactions – μ_b ; 2) surface Coulombic interface charge interactions – μ_{sc} ; 3) surface phonon interactions – μ_{sp} ; and 4) surface roughness interactions – μ_{sr} . After obtaining an expression for the low field mobility, I present a form for the high-field mobility. The high and low-field mobilities are then correlated using Thornber’s scaling relationship [28].

Using Mathiessen’s rule[29], which states that the local mobility is inversely proportional to the sum of the individual scattering rates, the following general expression for the inverse mobility is obtained:

$$\frac{1}{\mu} = \frac{1}{\mu_{lf}} + \frac{1}{\mu_{hf}} = \frac{1}{\mu_b} + \frac{1}{\mu_{sc}} + \frac{1}{\mu_{sp}} + \frac{1}{\mu_{sr}} + \frac{1}{\mu_{hf}} \quad (2.44)$$

I quantify this relation for SiC MOSFETs by developing a specific expression for each of the aforementioned contributions which affect mobility where μ_{lf} is the low field mobility and can be further divided into bulk mobility μ_b , interface charge mobility μ_{sc} , surface roughness mobility μ_{sr} , and surface phonon mobility μ_{sp} . Also included is the high field mobility μ_{hf} .

Bulk Mobility Low-field bulk mobility depends largely on acoustic phonon and ionized impurity scattering[26]. Empirical investigations have shown that the integrated effects of these scattering mechanisms can be described phenomenologically using the Caughey-Thomas model for bulk mobility[30]. I use Caughey-Thomas-like model and adapt it for SiC MOSFETs. To achieve this I use specific values

	6H-SiC	4H-SiC
$\mu_{max} (cm^2 V^{-1} sec^{-1})$	500 [31]	1071 [31]
γ_b	0.45 [31]	0.40 [31]
$N_{ref} (cm^{-3})$	1.11×10^{18} [31]	1.94×10^{17} [31]

Table 2.1: Low-field Bulk Mobility Parameters for 6H- and 4H-Silicon Carbide Using a Caughey-Thomas Based Model

for the model parameters using extracted data from Monte Carlo calculations and experiment[6, 31, 32]:

$$\mu_b = \frac{\mu_{max}}{1 + \left(\frac{N_d^+ + N_a^-}{N_{ref}}\right)^{\gamma_b}}. \quad (2.45)$$

$N_d^+ + N_a^-$ is the ionized doping concentration. Mentioned earlier in this chapter, the thermal ionization energies for dopants, especially acceptors, is rather large in silicon carbide resulting in a lower percentage of ionized dopants. Based on the equation above, this fact leads to the conclusion that silicon carbide based devices should experience less ionized impurity mobility degradation in non-depleted regions. Parameter values used in this model are given in Table 2.1.

Surface Charge To account for the effect of surface interface charge scattering on mobility I build on previous work, which argued that the following relationship was applicable to the Si-SiO₂ interface during weak inversion[33]:

$$\mu_{sc} \propto \frac{\Gamma_{sc} T}{N_T} \quad (2.46)$$

N_T is the sum of all surface charge densities (*i.e.* fixed oxide charge density and

trapped interface charge density, $N_f + N_{it}$). Using semi-classical perturbation theory the coefficient Γ_{sc} (*cgs*) is given by[33]:

$$\Gamma_{sc} = \frac{q}{m_c} \left(\frac{\frac{1}{2}(\epsilon_{ins} + \epsilon_{semi})}{q^2} \right)^2 \left(\frac{hk_B}{\pi^3} \right) \quad (2.47)$$

where m_c is the electron conductivity effective mass, h is Planck's constant, k_B is Boltzmann's constant, and $\epsilon_{ins(semi)}$ is the relative permittivity of the insulator (semiconductor). Values used to calculate theoretical Γ_{sc} for 6H- and 4H-silicon carbide are given in Table 2.2.

As more electrons populate the inversion layer, the net effect of the surface charge on electron transport is reduced; consequently, the surface charge component of mobility is increased. This effect is called screening because the inversion layer electrons nearest to the surface screen the other electrons from the Coulombic effects of the surface interface charge. Though the mobility model given in [33] is both completely physical and computationally tractable, it neglects to include the effects of screening due to inversion layer occupation; in short, another model is needed. Lombardi *et al.*[25] present a comprehensive surface mobility model for silicon MOSFETs. In their work a surface charge mobility component showing the trend of the screening effect is given, but this form is not complete enough to be included in a device transport model. Hiroki *et al.*[34] present a MOSFET mobility model that implements the surface charge effects with inversion layer screening as described by Schwarz and Russet[35]. However, the parameter used to account for this phenomenon is also used to describe surface phonon and roughness scattering

making the isolation of each mechanism impossible. Desiring to benefit from the physical intuition associated with the work of Sah *et al.* while still accounting for carrier screening effects on mobility, I modify the model given by [33] by introducing an additional term that is modelled after the Cahy-Thomas implementation of ion scattering effects for bulk mobility. The model is given by

$$\mu_{sc} = \frac{\Gamma_{sc} T}{N_T} \left(1 + \frac{n}{n_{scr}} \right)^{\zeta_{sc}} \quad (2.48)$$

where Γ_{sc} , N_T , and T are the same as those in [33], n is the electron concentration in cm^{-3} , and n_{scr} and ζ_{sc} are empirical parameters. The parallelism between the $\left(1 + \frac{n}{n_{scr}} \right)^{\zeta_{sc}}$ term of the above expression and the $\left(1 + \left(\frac{N_d^+ + N_a^-}{N_{ref}} \right)^{\gamma_b} \right)$ of the bulk mobility model should be apparent. However, unlike the bulk mobility equation, the Coulombic expression in Equation 2.48 improves mobility as the concentration value increases.

When solving the drift-diffusion equations for a two dimensional device model, I use a slightly modified version of the form found in [33], where I introduce an additional term to account for carrier screening effects. This additional term reduces electron scattering with surface interface charge in a manner similar to that provided by the Brooks-Herring model, which is obtained from perturbation theory[26]. The resulting model used in the simulator is given by the following:

$$\mu_{sc}(N_T, n) = \frac{\Gamma_{sc} T}{N_T} \left(1 + \frac{n}{n_{scr}} \right)^{\zeta_{sc}} \quad (2.49)$$

	6H-SiC	4H-SiC
m_c (m_o)	0.470	0.316
ϵ_{ins} (ϵ_0)	3.9	3.9
ϵ_{semi} (ϵ_0)	9.8	9.8
$\Gamma_{sctheory}$ ($V^{-1} sec^{-1} K^{-1}$)	1.016×10^{11}	1.510×10^{11}

Table 2.2: Interface Charge Density Mobility Parameters for 6H- and 4H-Silicon Carbide MOSFETs

where n is the electron concentration (cm^{-3}); n_{scr} (cm^{-3}) and ζ_{sc} are physical surface attributes.

Surface Phonons Using Fermi's golden rule, the scattering time for the surface acoustic phonon interaction is obtained and shown below[33].

$$\tau_{ac} = \left(\frac{8\pi^3 m^* Z_A^2 k_B T}{h^3 \rho_s u_l^2} \right)^{-1} \quad (2.50)$$

The resulting mobility due to acoustic phonon interaction is given by

$$\mu_{ac} = \frac{q\tau_{ac}}{m_c} = \frac{qh^3 \rho_s u_l^2}{8\pi^3 m^* m_c Z_A^2 k_B T} \quad (2.51)$$

where q is the charge of an electron, h is Planck's constant, ρ_s is the areal mass density of SiC, u_l is the velocity of sound in SiC, and m^* is the density of states effective mass. Z_A is the surface acoustic phonon deformation potential.

According to Schwartz and Russek [35], the areal mass density is approximately equal to the product of the bulk mass density and the channel thickness. Consequently, we obtain the following:

$$\rho_s \simeq \rho_{bulk} z = \rho_{bulk} (z_{CL} + z_{QM}) \quad (2.52)$$

where z_{CL} and z_{QM} are the classical and quantum components of the average channel thickness z given by

$$z_{CL} = \frac{3 k_B T}{2 q E_{\perp}} \quad (2.53)$$

and

$$z_{QM} = \left(\frac{9 h^2}{16 \pi^2 q m_{\perp} E_{\perp}} \right)^{1/3}. \quad (2.54)$$

E_{\perp} and m_{\perp} are the perpendicular average electric field and the effective mass in the crystallographic direction perpendicular to the surface, respectively. Now, rearranging the terms, the following vertical-field-dependent form for the mobility term due to surface phonons is obtained:

$$\mu_{ac}^{-1}(E_{\perp}) = \frac{\alpha_{ac} E_{\perp}}{1 + \frac{\beta_{ac}}{T} E_{\perp}^2}. \quad (2.55)$$

where

$$\alpha_{ac} = \left(\frac{3}{2} \rho_{bulk} \gamma_{ac} \right)^{-1} \quad (2.56)$$

$$\gamma_{ac} = \frac{h^3 u_l^2}{8 \pi^3 m^* m_{\mu} Z_A^2} \quad (2.57)$$

	6H-SiC	4H-SiC
$\alpha_{theory} \left(\frac{sec}{cm} \right)$	8.8×10^{-9}	2.3×10^{-9}
$\beta_{theory} \left(\left(\frac{V}{cm} \right)^{2/3} \right)$	62.7×10^{-4}	114×10^{-4}

Table 2.3: Theoretical Surface Phonon Parameters for 6H and 4H-Silicon Carbide MOSFETs

$$\beta_{ac} = \frac{2}{3} \frac{q}{k_B} \left(\frac{9h^2}{16\pi^2 q m_{\perp}} \right)^{1/3}. \quad (2.58)$$

Theoretically calculated values for α_{ac} and β_{ac} are given in Table 2.3. However, according to the reports in [25] and [34] for silicon MOSFETs, experimentally calculated values for α_{ac} in silicon tend to be 3 to 6 times larger than the theoretical value. This discrepancy is explained by results given in the work of Sah *et al*[33]. According to their work, for temperatures higher than 150 Kelvin, low field mobility reduction in silicon is not only due to surface acoustic phonon scattering but also surface optical phonon scattering and intravalley scattering. This phenomenon effectively raises the value of the physical parameter α . So, I have used an α value of $4 \times 10^{-8} \frac{sec}{cm}$ and $1.1 \times 10^{-8} \frac{sec}{cm}$ for the 6H- and 4H-silicon carbide, respectively, accounting for effects observed in Si devices. For β_{ac} the theoretical value is used since quantum effects represented by β_{ac} can be neglected given the large device geometry of specimens examined in this dissertation.

Surface Roughness Surface roughness scattering is a complicated phenomenon that is highly dependent on the quality of the interface, which may vary from process to process. Research has shown that surface roughness scattering is proportional to the square of the areal surface charge density[36], and this information has been

used along with Gauss' law to derive the following expression for surface roughness scattering[25, 37]:

$$\mu_{sr}(E_{\perp}) = \frac{\delta_{sr}}{E_{\perp}^2} \quad (2.59)$$

where E_{\perp} is the electric field perpendicular to the direction of surface transport, and δ_{sr} is a proportionality constant. The proportionality constant accounts for the combined effects of various parameters including the roughness correlation length, oxide permittivity, and the wave vector at the Fermi surface. The original form given in [36] is

$$\mu_{sr}^{-1} = \frac{m}{q\tau_{sr}} = \frac{m}{q} \frac{L^2 \Delta^2}{h^3} \left(\frac{q^2}{\epsilon_r \epsilon_0} \right)^2 (N_T + N_{depl}) f \quad (2.60)$$

where L is the correlation length, Δ is the root mean square deviation, N_{depl} is the areal surface charge density of depleted bulk region, and all other terms have been defined previously. f is given by

$$f = \int_0^{\pi} d\theta (1 - \cos \theta) \exp \left[-(1 - \cos \theta) k_F^2 L^2 / 2 \right] \quad (2.61)$$

where k_F is the Fermi wave vector.

Work by Joshi [38] suggest that surface roughness, not interface traps, is the dominant surface of surface scattering in silicon carbide MOSFETs. The results of this work use a value of $1 \times 10^{13} \frac{V}{sec}$ for δ_{sr} unless stated otherwise. This corresponds

to a correlation length of approximately 500 Angstrom and a root mean square deviation of 5.4 Angstrom. These quantities produce a δ_{sr} that is 60 times lower than that calculated for silicon MOSFETs by Lombardi *et al.* and corresponds to a surface approximately 50 times rougher.

High Field Interactions Monte Carlo simulation and other solutions to the Boltzmann transport equation have shown that a large parallel electric field imparts energy on electrons, which increases the rate of scattering due to optical phonons[26, 39]. This increased scattering rate reduces mobility and significantly contributes to velocity saturation. Thus, the velocity saturates in the direction parallel to the applied electric field, and its magnitude becomes nearly field independent. Consequently, the following empirical form is used for the high-field mobility component in SiC MOSFETs[27]:

$$\frac{1}{\mu_{hf}} = \frac{E_{\parallel}}{v_{sat}^{inv}} \quad (2.62)$$

where E_{\parallel} is the electric field component parallel to the surface transport, and v_{sat}^{inv} is the inversion layer saturation velocity.

Total MOSFET Mobility Beginning with Mathiessen's rule, the sum of the inverses of low and high-field mobility components is computed: $(\frac{1}{\mu_{lf}} + \frac{E_{\parallel}}{v_{sat}^{inv}})$. Rearranging the sum and inverting gives the following familiar preliminary expression for MOSFET mobility:

	6H-SiC	4H-SiC
γ	1.5	1.5
$v_{sat}^{inv} \left(\frac{cm}{sec} \right)$	2.0×10^7	2.0×10^7

Table 2.4: Theoretical Thornber High Field Parameters for 6H- and 4H-Silicon Carbide

$$\mu_{pre} = \frac{\mu_{lf}}{\left[1 + \left(\frac{\mu_{lf} E_{\parallel}}{v_{sat}^{inv}} \right) \right]} \quad (2.63)$$

The above expression assumes that low and high field scattering are mutually exclusive. However, solutions to the Boltzmann equation have shown that this is not strictly the case[37]. To account for the coupling between the high and low-field regimes, I follow the work of Thornber[28], and make a small correction to Equation (2.63). This leads to the final form for MOSFET mobility:

$$\mu_{MOS} = \frac{\mu_{lf}}{\left[1 + \left(\frac{\mu_{lf} E_{\parallel}}{v_{sat}^{inv}} \right) \right]^{\gamma^{1/\gamma}}} \quad (2.64)$$

where γ is an exponential correction factor that acts to couple the low and high-field regimes for mobility[28]. Values for the Thornber parameter of silicon carbide are given in Table 2.4. The explicit form for low field mobility μ_{lf} is given by

$$\mu_{lf} = \frac{\mu_b}{1 + \mu_b \left(\frac{\alpha_{ac} E_{\perp}}{1 + \frac{\beta_{ac,th}}{T} E_{\perp}^2/3} + \frac{N_T}{\Gamma_{sc}} \left(\frac{1}{T} \right) \left(1 + \frac{n}{n_{scr}} \right)^{-\zeta'_{sc}} + \frac{E_{\perp}^2}{\delta_{sr}} \right)}. \quad (2.65)$$

Anisotropy In addition to the aforementioned scattering mechanisms, crystal orientation can play a crucial role in electron transport characterization. Though

usually treated as a scalar, mobility is in fact a tensor quantity. For the two dimensional transport discussed in this work, the mobility tensor, $\bar{\mu}$ is represented by the following:

$$\bar{\mu} = \begin{bmatrix} \mu_x & 0 \\ 0 & \mu_y \end{bmatrix} \quad (2.66)$$

where μ_x is the mobility experienced by carriers travelling in the x direction, and μ_y is the mobility experienced by carriers travelling in the y direction. As a result, the average drift velocity of an electron or hole can be expressed as the product of the mobility tensor $\bar{\mu}$, and the electric field vector \vec{E} , where \vec{E} is given by

$$\vec{E} = \begin{bmatrix} E_x \\ E_y \end{bmatrix}. \quad (2.67)$$

E_x and E_y are the x and y components of the electric field, respectively. The resulting carrier velocity is shown below.

$$\vec{v} = \bar{\mu}\vec{E} = \begin{bmatrix} \mu_x & 0 \\ 0 & \mu_y \end{bmatrix} \begin{bmatrix} E_x \\ E_y \end{bmatrix} = \begin{bmatrix} \mu_x E_x \\ \mu_y E_y \end{bmatrix} = \begin{bmatrix} v_x \\ v_y \end{bmatrix}. \quad (2.68)$$

Practically speaking, only the low-field bulk and high-field mobility components are functions of crystal orientation since the others specifically require that transport is occurring parallel to the metal-oxide-semiconductor interface. As a result, the tensor expressions for surface charge, surface roughness, and surface phonon effects all have the following form

$$\bar{\bar{\mu}}_{sc,sp,sr} = \begin{bmatrix} \mu_{sc,sp,sr} & 0 \\ 0 & 0 \end{bmatrix}, \quad (2.69)$$

and the tensor expressions for bulk and high-field effects have the form given by Equation 2.66. The explicit forms of these tensor expressions are shown below.

$$\bar{\bar{\mu}}_b = \begin{bmatrix} \alpha_b \frac{\mu_{max}}{1 + \left(\frac{N_D^+ + N_A^-}{N_{ref}} \right)^{\gamma_b}} & 0 \\ 0 & \zeta_b \frac{\mu_{max}}{1 + \left(\frac{N_D^+ + N_A^-}{N_{ref}} \right)^{\gamma_b}} \end{bmatrix} \quad (2.70)$$

$$\bar{\bar{\mu}}_{MOS} = \begin{bmatrix} \frac{\mu_{lf}}{\left[1 + \left(\frac{\mu_{lf} E_{\parallel}}{\alpha_v v_{sat}^{inv}} \right)^{\gamma} \right]^{1/\gamma}} & 0 \\ 0 & \frac{\mu_{lf}}{\left[1 + \left(\frac{\mu_{lf} E_{\parallel}}{\zeta_v v_{sat}^{inv}} \right)^{\gamma} \right]^{1/\gamma}} \end{bmatrix} \quad (2.71)$$

Values for the 6H-SiC electron mobility α and ζ tensor terms are 1.0, 0.22, 1.0, and 0.85 for α_b , ζ_b , α_v , and ζ_v , respectively. For 4H-SiC the values are 0.8, 1.0, 0.85, and 1.0, respectively.

2.1.3 Boundary Conditions

In this section I discuss the boundary conditions associated with the drift-diffusion based transport model on silicon carbide metal-oxide-semiconductor field-effect-transistors. Constraints include conditions at both contact and artificial boundaries in addition to material boundaries - specifically the oxide-semiconductor interface. See Figure 2.1 for a diagram of the various MOSFET boundaries.

Ohmic Contacts

Of the four terminals associated with the MOSFET (gate, source, drain, and bulk), three of these are modelled as ideal Ohmic contacts. By Ohmic, I mean that the contact itself has a negligible current resistance when compared to that of the semiconductor on which it is mounted. Therefore, all of the voltage applied to the contact is transferred to the underlying semiconductor material. There is no power loss in an ideal Ohmic contact. An important consequence of these is that the free carrier concentrations at the Ohmic contact are unchanged during current flow and thus maintain their thermal equilibrium values.

It is well-known that the material potentials of a doped semiconductor in thermal equilibrium can be modelled by the following equations:

$$\phi_n = V_T \ln \frac{N_d^+}{n_i} \quad (2.72)$$

and

$$\phi_p = -V_T \ln \frac{N_a^-}{n_i} \quad (2.73)$$

where ϕ_n and ϕ_p are the electrostatic potential for n-type and p-type semiconductor materials, respectively, n_i is the intrinsic carrier concentration, V_T is the ambient thermal voltage, and N_d^+ and N_a^- are the ionized dopant concentrations of donor and acceptor ions, respectively. There is no voltage drop across the Ohmic contact, so the boundary condition for electrostatic potential at the contact-semiconductor

boundary is equal to

$$\phi_C = V_C + \phi_n \quad (2.74)$$

for Ohmic contacts residing on n-type material and

$$\phi_C = V_C + \phi_p \quad (2.75)$$

for Ohmic contacts residing on p-type material. V_C is the voltage applied to the terminal.

Because of the no-power-loss property of the ideal Ohmic contact, thermal equilibrium, and therefore charge neutrality, can be assumed at the contact-semiconductor boundary. The total charge density ρ is given by

$$\rho = q(p - n + D) = 0 \quad (2.76)$$

where $D = N_d^+ - N_a^-$. Since we are dealing with thermal equilibrium conditions, the mass action law ($np = n_i^2$) applies, and by using the appropriate substitutions for n- and p-type semiconductors, we end up with the following solutions:

$$n = \frac{D}{2} + \frac{\sqrt{D^2 + 4n_i^2}}{2}, \quad p = \frac{n_i^2}{n} \quad (2.77)$$

for n-type material and

$$p = \frac{-D}{2} + \frac{\sqrt{D^2 + 4n_i^2}}{2}, \quad n = \frac{n_i^2}{p} \quad (2.78)$$

for p-type material.

Gate Contact and Semiconductor-Oxide Interface

The boundary conditions for the gate contact are similar to those of the ideal Ohmic contact, but some modification is needed. Specifically, the oxide under the gate contact contains no holes or electrons, ideally. So, there is no material potential offset with regard to carriers and electrostatic potential. However, an analogous concept does exist – the intrinsic semiconductor band-bending. Therefore, the boundary condition for the electrostatic potential on the gate contact is defined by the following equation:

$$\phi_g = V_G + V_{offset} \quad (2.79)$$

where V_G is the applied gate voltage and V_{offset} is defined as the additional voltage required to create flat band conditions in the MOS structure when the theoretical flat band voltage is applied to the gate contact ($V_G = V_{FB}$). By defining V_{offset} this way, I am guaranteed to produce the proper values for intrinsic semiconductor band-bending. V_{offset} is a function of gate material, insulator material and thickness, and semiconductor material and doping.

The heart of the MOSFET device is the semiconductor-oxide interface. Though this interface is not one that terminates the device, material boundaries are

being crossed, and certain criteria must be satisfied when crossing this interface. Again, I assume that no current or free particle exchange between the oxide and semiconductor layers because of the oxide thickness. As a result the perpendicular components of the electron and hole current densities are both set to zero. However, boundary conditions do exist for the electrostatic potential at the interface. For electrostatic potential Gauss' law is implemented at the semiconductor/insulator interface. This relation is expressed by

$$\hat{a}_s \cdot (\vec{D}_i - \vec{D}_s) = Q_{surf} \quad (2.80)$$

where \vec{D} is the electric displacement vector and Q_{surf} is the effective surface charge density at the insulator/semiconductor interface, and \hat{a}_s is a unit vector in the direction of the semiconductor oxide interface.

Artificial Boundaries

All power received from or transferred to the device from outside of the MOSFET is done via the contact boundaries. However, artificial boundaries must also be considered. Artificial boundaries consist of all boundaries in which the device structure ceases to exist for simulation purposes but in reality this boundary may not exist on the device physically. For the purposes of this work, the artificial boundaries of the MOSFET are placed far enough away from the carrier transport activity so that the following boundary condition can be applied without any loss of simulation reliability:

$$\frac{\partial C}{\partial N_{art}} = 0 \quad (2.81)$$

where C is representative of potential, electron concentration, and hole concentration, and $\frac{\partial C}{\partial N_{art}}$ is the derivative of C in the direction normal to the artificial boundary.

2.2 Chapter Summary

I have reviewed the drift-diffusion equations and presented them within the context of transport modelling for silicon carbide metal-oxide-semiconductor field-effect-transistors. Also, special emphasis has been placed on mobility relations for SiC MOSFETs. I will use the next few chapters to describe how these relations enable the extraction of meaningful surface model parameters and explain what implications can be made regarding present and next generation silicon carbide MOSFETs.

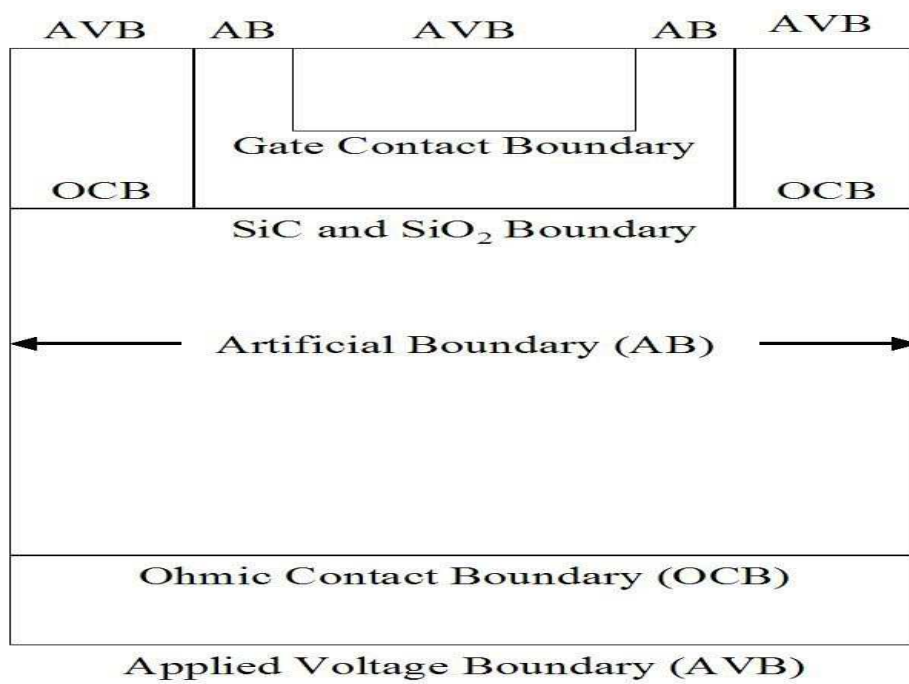


Figure 2.1: MOSFET boundaries showing all contact, interface, and artificial terminations.

Chapter 3

Experimentation and Simulation of 6H-SiC MOSFETs

In this chapter I present several 6H-SiC MOSFET devices, explain the process of experimentation and simulation performed on these devices, and report my findings from each of the processes. My major accomplishment in this chapter consists of using experimental data in conjunction with my simulation tool to accurately characterize the surface quality of the 6H-SiC MOSFETs studied in this work. Experimental techniques include direct measuring of device terminal characteristics that provide valuable information about the overall electrical behavior of the devices. Using the physics based simulation tool, I not only model the terminal characteristics of these devices but also examine the surface characteristics of the devices by investigating behavior not directly measurable by experimental techniques. Using the custom 6H silicon carbide device simulator, I am able to expose the shortcomings of surface characteristic extraction using terminal characteristics. All experimental work was conducted at the Army Research Laboratory in Adelphi, Maryland, and all simulation work was performed at the University of Maryland, College Park.

	device A1	device A2	device A3
W (μm)	200	100	100
L (μm)	4	4	8
	device B1	device B2	device B3
W (μm)	100	100	100
L (μm)	4	4	8

Table 3.1: Dimensions for Cree Research 6H-SiC MOSFETs studied in this work.

3.1 Device Design

In this work n-channel, enhancement-mode 6H-SiC MOSFETs fabricated by Cree Research, Incorporated in Durham, North Corollina were used. The gate oxide was (nominally 500Å thick) formed by wet thermal oxidation grown at 1025 degrees Celsius, followed by a wet 950 degrees Celsius re-oxidation anneal. MOSFETs were fabricated on the silicon face of a $3\mu m$ p-type 6H-silicon carbide epitaxial layer doped to approximately $5 \times 10^{15} \text{ cm}^{-3}$. Source and drain regions were implanted with nitrogen to $2 \times 10^{20} \text{ cm}^{-3}$ and activated with an anneal greater than 1600 degrees Celsius.

The Ohmic source and drain contacts are nickel (Ni) and the gate metal is sputtered molybdenum (Mo). The devices consists of the following width (W) to length (L) ratios: $200\mu m$ by $4\mu m$, $100\mu m$ by $4\mu m$, and $100\mu m$ by $8\mu m$, resulting in gate areas of 4×10^{-4} and $8 \times 10^{-4} \text{ cm}^2$. See Figure 3.1 for the device profile. Experimental and simulation results are based on the set of MOSFETs given in Table 3.1 [12].

3.2 Experimental Setup

Both drain-source current and charge pumping current were measured. Current-voltage (I-V) characteristics were measured from cut-off to saturation. The threshold voltage - V_{th} , drain conductance - G_d , and average electron channel mobility - $\bar{\mu}_n$, for each MOSFET were extracted using the I-V characteristic values. The voltage shift of the extracted V_{th} relative to the theoretical threshold voltage was used to indicate the net charge at the oxide/semiconductor interface, which includes both fixed oxide charge (Q_f) and average interface trap (\bar{Q}_{it}) charge.

Measuring the drain current versus gate-source voltage characteristics for a range of gate voltage values, I have used the ratio of the two components to compute the drain conduction G_d to calculate its value. (Equation 3.1.)

$$G_d = \frac{I_D}{V_{DS}} \quad (3.1)$$

To extract the effective electron surface mobility values for the linear operation region, the standard text book description of MOSFET terminal characteristics for the triode region has been used (the triode region being the condition in which the difference between the gate-source voltage V_{GS} and the threshold voltage V_{th} is greater than the drain-source current V_{DS})

$$I_D = \bar{\mu}_n \frac{W}{L} C_{ox} \left[(V_{GS} - V_{th}) V_{DS} - \frac{V_{DS}^2}{2} \right] \quad (3.2)$$

where $\bar{\mu}_n$ is the average electron channel mobility, W and L are the device width

and length, respectively, C_{ox} is the capacitance of the silicon dioxide insulator, and V_{GS} , V_{th} , and V_{DS} are the gate-source voltage, threshold voltage, and drain-source voltage, respectively. In the limit that V_{DS} is much less than 1 Volt, the squared term in Equation 3.2 can be neglected, and solving for the average mobility, the following is obtained:

$$\bar{\mu}_n = \frac{G_d}{\frac{W}{L} C_{ox} (V_{GS} - V_{th})} \quad (3.3)$$

where G_d is defined above in Equation 3.1.

In order to experimentally extract the total average interface state trap charge, \bar{Q}_{it} , the charge pumping (CP) technique[40, 41] has been used. The CP technique consists of applying a voltage pulse to the gate of the MOSFET while the source and drain are shorted together and held at a small reverse bias with respect to the bulk. The gate pulse voltage is adjusted to change the potential of the 6H-SiC MOSFET semiconductor surface so that the interface goes from accumulation to inversion then back to accumulation. During the rising edge of the pulse, the deeply depleted MOS surface begins to fill with electrons from the source and drain. These electrons are then captured or trapped first by positively charged interface traps in the lower half of the 6H-SiC bandgap then by neutral traps in the upper half of the bandgap. On the falling edge of the pulse, electrons that were captured by the interface traps are ejected from the traps and recombine with the majority carriers in the bulk. This process results in a net charge transfer, Q_{CP} , to the bulk which is assumed to be proportional to the interface trap density of states, $D_{it}(\varepsilon)$.

The relationship used for this proportionality is given by Equation 3.4:

$$Q_{CP} = qA_g \int D_{it}(\varepsilon) d\varepsilon \quad (3.4)$$

where q is the charge of an electron, A_g is the gate area and $D_{it}(\varepsilon)$ is the interface trap density of states. When the gate pulse is repeated at a particular frequency f , a substrate current I_{CP} , defined by Equation 3.5, is generated

$$I_{CP} = fQ_{CP} = q^2 f A_g \bar{D}_{it} \phi_s \quad (3.5)$$

where \bar{D}_{it} is then mean interface trap density of states averaged over the surface potential range $\Delta\phi_s$ swept during the gate voltage pulse. It has been assumed that the integral of $D_{it}(\varepsilon)$ with respect to energy ε can be replaced by the product of average interface trap density of states, \bar{D}_{it} , and the estimated change in surface energy, $q\Delta\phi_s$, where $\Delta\phi_s$ is the change in surface potential. Simplifying the expression, the energy dependence from the interface trap density of states has been removed. The ramifications of making this concession are discussed later.

\bar{D}_{it} has been extracted over an energy range of $2.2eV$ (the midgap $\pm 1.1eV$), and this value is used to estimate average charge holding interface trap density \bar{N}_{it} over $2\phi_B$, where ϕ_B is the electrostatic potential of the bulk. For this experiment, the gate voltage pulse had a maximum amplitude of $10V$, a frequency equal to 3.33 kHz, and a duty cycle of 0.25 . The number of fixed oxide charges per unit oxide area, Q_f , has been calculated by taking the difference between the effective charge

responsible for the net threshold voltage shift (Q_T) and the calculated average interface trap charge value, \bar{Q}_{it} . (Equation 3.6.)

$$Q_T = Q_f + \bar{Q}_{it} \quad (3.6)$$

3.3 Experimental Results

The theoretical MOSFET threshold voltage (V_{th}) value has been calculated by using the well known equation shown below

$$V_{th} = \phi_{MS} - \frac{Q_T}{C_{ox}} - 2\phi_B + \frac{(4q\epsilon_{SiC}N_A^-)^{1/2}}{C_{ox}} \quad (3.7)$$

where ϕ_{MS} is the work function difference between the gate metal (molybdenum) and the semiconductor (6H-SiC), C_{ox} is the oxide capacitance given by $\frac{\epsilon_{ox}}{t_{ox}}$ where t_{ox} is the oxide thickness, and ϕ_B is the bulk potential. The value for the work function of the gate material is obtained directly from literature [42]. To obtain the work function for SiC I used the following well-known expression for semiconductors[43]:

$$\phi_S = \left(\chi_s + \frac{\epsilon_c - \epsilon_i}{q} + V_T \ln \left(\frac{N_a^-}{n_i} \right) \right) \quad (3.8)$$

where χ_s is the semiconductor electron affinity (3.7-3.8V for 6H-SiC), ϵ_i is the semiconductor intrinsic Fermi level, V_T is the thermal voltage, n_i is the intrinsic carrier concentration, and N_{Af}^- is the ionized acceptor concentration at flatband. To determine N_{Af}^- I have performed simulations of incomplete ionization at the

	device A1 (cm^2/Vs)	device A2 (cm^2/Vs)	device A3 (cm^2/Vs)
$V_{GS} = 6V$	16.9	26.6	27.4
$V_{GS} = 7V$	15.7	24	26

Table 3.2: Effective electron channel mobilities for 6H-SiC MOSFETs of set A with $V_{DS} = 0.25V$. All values are less than 10% of the intrinsic bulk mobility value.

	device B1 (cm^2/Vs)	device B2 (cm^2/Vs)	device B3 (cm^2/Vs)
$V_{GS} = 6V$	21.1	29.8	28.5
$V_{GS} = 7V$	19.7	27.2	25.7

Table 3.3: Effective electron channel mobilities for 6H-SiC MOSFETs of set B with $V_{DS} = 0.25V$. All values are less than 10% of the intrinsic bulk mobility value.

equivalent flatband for Al doped SiC [44], and found a yield of 60% activation at room temperature. This gives rise to a value of $-1.92V$ for ϕ_{MS} . The calculated threshold theoretical voltage value for these devices is $1.33V$.

Examining the experimental data gathered from $I_D - V_{GS}$ measurements and using experimentation along with equations given above, I have found the following. For device A1 the measured threshold voltage ($3.9V$) is approximately 3 times higher than the calculated theoretical threshold voltage ($1.33V$). For devices A2 and A3 an even larger divergence from the expected theoretical value is discovered. Devices B1-B3 give similar results. The cause for such a drastic difference between theoretical and experimental values is assumed to be a byproduct of the high concentrations surface charge. I will revisit and justify this assumption in the next two sections.

Setting drain-source voltage, V_{DS} , equal to $0.25V$, I have extracted values for the effective electron channel mobility for V_{GS} equal to 6 and 7V at room temperature using Equation 3.3. The results are given in Tables 3.2 and 3.3. Experimental results indicate that the average linear region surface mobility for these devices

	device A1	device A2	device A3
$\bar{D}_{it} (cm^{-2}eV^{-1})$	1.30×10^{12}	1.05×10^{12}	7.13×10^{11}
$\bar{N}_{it} (cm^{-2})$	1.69×10^{12}	1.36×10^{12}	1.01×10^{12}
$\bar{N}_f (cm^{-2})$	(+) 5.31×10^{11}	(-) 1.05×10^{11}	(-) 4.78×10^{11}

Table 3.4: Experimentally extracted charge density of states and computed charge density values for the 6H-SiC MOSFETs of set A.

	device B1	device B2	device B3
$\bar{D}_{it} (cm^{-2}eV^{-1})$	1.58×10^{12}	8.66×10^{11}	7.11×10^{11}
$\bar{N}_{it} (cm^{-2})$	2.05×10^{12}	1.13×10^{12}	9.24×10^{11}
$\bar{N}_f (cm^{-2})$	(+) 7.39×10^{11}	(-) 2.56×10^{11}	(-) 5.03×10^{11}

Table 3.5: Experimentally extracted charge density of states and computed charge density values for the 6H-SiC MOSFETs of set B.

is approximately equal to $24 \text{ cm}^2 \text{ V}^{-1} \text{ sec}^{-1}$. This is only 6% of the bulk mobility value ($400 \text{ cm}^2 \text{ V}^{-1} \text{ sec}^{-1}$ for 6H-SiC MOSFETs with a substrate doping of approximately $5 \times 10^{15} \text{ (cm}^{-2}\text{)}$).

For device A1 the experimentally extracted average of the ionized interface trap density, \bar{N}_{it} , is approximately $1.7 \times 10^{12} \text{ cm}^{-2}$, and the computed fixed charge density, $\bar{N}_f = |Q_f/q|$, is approximately $(+)5.3 \times 10^{11} \text{ cm}^{-2}$. Both values were measured at room temperature. Tables 3.4 and 3.5 show the experimentally extracted values for \bar{D}_{it} , \bar{N}_{it} , and \bar{N}_f for all devices included in sets A and B[12]. The (\pm) symbol associated with the value of fixed oxide charge density is used to indicate a net positive or negative fixed oxide charge value, respectively. I have found the fixed oxide charge density values to be approximately 2.35 times smaller than their interface trap counterparts.

3.4 Simulation Process

At this time I will describe the setup for the simulation process. First, the interface trap model used for simulation is described in detail. Unlike the interface trap extraction technique performed during experiment, the simulation model retains energy dependence in the interface trap density of states model which will prove to be important in the text to follow. After detailing the interface trap model, I describe the methodology used to corroborate the experiment data with simulation. Using my simulation tool in conjunction with the measured terminal data, I have successfully extracted key figures of merit in regard to the surface quality.

3.4.1 Interface Charge Model

Mentioned previously, poor quality SiC/SiO₂ interfaces present a fundamental obstacle in the advancement of silicon carbide MOSFET technology[13]. Interface charge degrades the mobility and may increase the threshold voltage. As a result, it is not enough to incorporate the effects of interface charge in the mobility model; effects must also be included self-consistently within the Poisson equation by implementing Gauss' law at the semiconductor/insulator interface in the drift-diffusion model. By doing this, I am able to quantify the effects of interface charge on threshold voltage and electrostatic potential distribution within the device. At the interface Gauss' law requires that

$$\hat{a}_s \cdot (\vec{D}_i - \vec{D}_s) = Q_T \quad (3.9)$$

where \vec{D} is the electric displacement vector ($\vec{D} = -\epsilon_r \epsilon_o \nabla \phi$) and Q_T is the effective surface charge density at the insulator/semiconductor interface defined by Equation 3.6. The surface charge density includes fixed oxide charge Q_f and charge due to interface traps Q_{it} . The innovative physics included in this expression is found in the manner in which I model Q_{it} for the SiC MOSFETs. This expression is then calibrated by requiring the drift diffusion simulator to provide terminal characteristics that agree with experiment.

Though the average interface charge values extracted by experiment give insight into how much charge may be present at the semiconductor/insulator surface, the interface trap concentration and occupation are energy dependent; the energy dependence has been neglected by the experiment. Consequently, in order to simulate the interface charge dynamics of these devices, I have used the experimental data in conjunction with my simulator which has an energy dependent interface trap model. In order to more appropriately model the effects of interface trap states, I have introduced an expanded interface state model into the calculations. This model not only accounts for the spatial variation of occupied interface trap density but also includes the energy dependence of the trap density of states, which facilitates incorporation of gate bias into the analysis. The model for the interface charge occupation between the intrinsic level and the conduction band minimum is given in Equation 3.10 [13]

$$Q_{it}(x) = -qN_{it}(x) = -q \int_y \int_{\varepsilon_i}^{\varepsilon_c} D_{it}(\varepsilon) f_n(\varepsilon, x, y) \delta(y - y_{interface}) d\varepsilon dy \quad (3.10)$$

where $Q_{it}(x)$ is the charge density due to occupation of the upper-half interface states as a function of position along the semiconductor channel surface. $f_n(\varepsilon, x, y)$ is the probability function for finding an electron of energy ε . ε_c and ε_i are the conduction band minimum and intrinsic level, respectively. $D_{it}(\varepsilon)$ is the energy dependent trap density of states given by[13]

$$D_{it}(\varepsilon) = D_{ito} + D_c \exp \left[- \left(\frac{\varepsilon_c - \varepsilon}{\xi_c} \right) \right] \quad (\varepsilon_i < \varepsilon < \varepsilon_c) \quad (3.11)$$

where D_{ito} is the midband energy independent trap density, D_c is the conduction band edge trap density, ξ_c is the bandtail decay energy. Such a model has been validated experimentally for both 4H- and 6H-silicon carbide MOSFETs[7, 45]. I have assumed that all interface charge resides at the semiconductor/insulation junction, and as a result, include the delta function, $\delta(y - y_{interface})$, in the model for $Q_{it}(x)$.

Since the current flow perpendicular to the interface is negligible in MOSFETS with moderately thick oxides, it is reasonable to approximate $f_n(\varepsilon, x, y)$ using quasi-equilibrium statistics. Taking the energy space distribution of electrons and interface states occupation to be described by Fermi statistics, it is straightforward to show that $f_n(\varepsilon, x, y)$ takes on the following form[46]:

$$f_n(\varepsilon, x, y) = \frac{1}{1 + \frac{1}{2} \frac{N_c}{n(x,y)} \exp\left(\frac{\varepsilon - \varepsilon_c}{k_B T}\right)} \quad (3.12)$$

where ε_c is the conduction band minimum, N_c is the electron effective density of states, and $\frac{1}{2}$ is included to account for spin degeneracy. Equations (3.10) through (3.12) represent an interface state model in both energy space and real-space. Now that the model has been defined, values for the parameters D_{ito} , D_c and ξ_c need to be determined. An analogous set of expressions are used for the occupation of interface states for energies between the intrinsic level and the valence band maximum, with appropriate changes of sign. When the states below the intrinsic level are occupied by electrons they go from positively charged to neutral.

The question now arises as to how the experimental findings are incorporated into the simulator's interface trap model presented above. To answer this question, I refer back to the charge pumping (CP) technique describe previously. An analysis of electron occupation of interface traps under the conditions described in the CP experiment reveals that the extracted mean interface trap density of states \bar{D}_{it} is more representative of midband energy independent value D_{ito} than the full band average of the interface trap density of states. So, I have chosen \bar{D}_{it} as the value to use for D_{ito} . Justification for this decision follows.

The CP experiment was performed such that the bandgap was swept over a range of $\varepsilon_i \pm 1.1eV$ where ε_i is the midband value. For 6H-SiC this range is equivalent to approximately 73% of the bandgap. However, experimental finding by Saks *et al.* [7, 45] confirm that the 13 or so percent at each band edge significantly

contributes to the threshold voltage shift and mobility degradation observed in SiC MOSFETs. Shown in Figure 3.2 is an example of a possible interface trap density of states profile and electron Fermi distribution function versus bandgap energy. The interface trap density of states value peaks near the band edges. The Fermi distribution function is representative of a 6H-SiC MOSFET in the superthreshold region ($V_{GS} > V_{th}$). Notice that there is a non-zero probability that electrons occupy energy traps above the $2.6eV$ limit of the experiment. Consequently, the *CP* experiment described in this chapter is not sufficient enough to properly characterize \bar{D}_{it} over the entire range of the bandgap, and thus there is a need for accurate investigation. I have used the drift-diffusion simulation tool to perform a more accurate, rigorous analysis of the interface traps and their effect on 6H-SiC MOSFETs.

For the range swept by the *CP* experiment, the interface trap density of states value extracted using the *CP* experiment is approximately equal to the mid-band energy independent value. However, when the MOSFET surface is inverted (V_{GS} is greater than V_{th}), electrons occupy trap states that go beyond the range swept by *CP*. Figure 3.3 shows the product of the interface trap density of states and the electron Fermi distribution function versus bandgap energy. Equation 3.13 shows the relationship between interface trap density of states $D_{it}(\varepsilon)$, the electron Fermi distribution $f_n(\varepsilon, x, y)$, and their product, the occupied states $B_{it}(\varepsilon, x, y)$. Notice the non-zero value that extends beyond the $2.6eV$ band energy value. When the MOS surface is inverted, such as the case when experimentally extracting the

device threshold voltage, occupied traps that could not be accounted for when using *CP* technique are present. This happens because the energy dependence of the trap occupation has been removed. Furthermore, these unaccounted occupants contribute significantly to the total interface charge value. For the example shown in Figure 3.3, the amount of interface trap charge (measured from midband to conduction band edge for neutral interface trap states) not accounted for by experiment is about 50% of the extracted value. I conclude that the *CP* process conducted in the lab described above could yield values that under estimate the total interface trap charge by 30 percent - possibly more if the midband value is significantly lower than the band edge values. Given this information, it most likely that the extracted \bar{D}_{it} value is representative of only the midband interface trap density of states value.

$$B_{it}(\varepsilon, x, y) = D_{it}(\varepsilon)f_n(\varepsilon, x, y) \quad (3.13)$$

3.4.2 Methodology and Results

In order to verify the soundness of the two dimensional (2D) simulator, I have used the simulation tool to match experimental data of 6H-SiC MOSFETs. In the pages directly following, I present data modelling the electrical characteristics of 6H-SiC MOSFETs fabricated by Cree, Inc., and using experimentally extracted values for the midband interface trap density of states D_{ito} , I examine the behavior of these devices at room elevated temperature. Experimental data for I_D versus V_{GS} and I_D versus V_{DS} at room temperature exist for all device in sets A and B. All

experimental I-V characteristics and their simulated counterparts are presented. High temperature data exist for device A3 only and will be discussed in the next chapter.

Starting with set A, simulations of the terminal characteristics of each device were performed. Specifically, drain current versus gate-source voltage and drain-source voltage simulation were conducted. The mean interface trap density of states value \bar{D}_{it} was used as the midband density of states value D_{ito} . Modelling parameters for each device were then optimized to best fit their respective I-V curves. This process was done iteratively until agreement between simulation and experiment was achieved. After matching was achieved for each device in set A, I calculated the average of the modelling values discovered for this set and used my findings as the empirical parameter set (with exception of N_f) for simulation of the devices in B.

I begin with examining the simulated data for the devices of set A. Remember, for this set the modelling parameters were optimized for each device separately. The first parameter fitted is the fixed oxide density N_f . This is accomplished using the $I_D - V_{GS}$ data. When the MOSFET is in the subthreshold ($V_{GS} \ll V_{th}$), electrons are not plentiful at the surface, so few traps near the conduction band edge are occupied. As a result, the interface trap charge is dominated by the presence of electrons in the midband region. In addition, screening is not a factor because of the low volume of electrons at the surface. Given the above conditions, the only empirical parameter affecting the terminal characteristics is the fixed oxide density.

The value for N_f has been iteratively adjusted until agreement is achieved between simulation and experiment in the subthreshold region.

Moving up the $I_D - V_{GS}$ curve, electrons begin to populate the interface trap states near the conduction band edge as the gate-source voltage is increased, and the modelling terms D_c and ξ_c begin to play a role. In order to get an initial guess for the bandtail decay value, ξ_c , I rely on the experimental findings in [7] and [45]. Based on their work I have determined that a reasonable value for ξ_c lies between 0.1 and 0.2eV. The value for the band edge interface trap density of states peak, D_c , is obtained by requiring that the transition region from subthreshold to threshold agrees with experimental observation.

Once the $I_D - V_{GS}$ curve moves from subthreshold to super-threshold, the difference in I_D for various values V_{DS} becomes apparent. This is due to the fact that the increased population of electrons at the semiconductor surface begin to screen the negative charge effects of the occupied interface traps causing an increase in mobility and consequently the drain current. My model accounts for this phenomenon with the electron screening parameters, n_{Cit} and ζ_{Cit} . These two values are obtained by requiring agreement between experiment and simulation for super-threshold values of I_D at V_{DS} equal to 0.25 and 0.5V. Table 3.6 contains the values for n_{Cit} and ζ_{Cit} obtained for all devices in set A. Notice that the n_{Cit} value is on the same order of magnitude as the expected electron concentration at the surface, demonstrating the feasibility of my inclusion of the $\left(1 + \frac{n}{n_{Cit}}\right)^{\zeta_{Cit}}$ term in the interface charge portion of the low field mobility.

	device A1	device A2	device A3	average
D_c ($cm^{-2} eV^{-1}$)	9.1×10^{12}	1×10^{13}	1.52×10^{13}	1.143×10^{13}
ξ_c (eV)	0.106	0.1162	0.11	0.1107
N_f (cm^{-2})	(+) 1.18×10^{12}	(+) 7.12×10^{11}	(+) 3.80×10^{11}	-
n_{Cit} (cm^{-3})	2.6×10^{17}	2.5×10^{17}	3.65×10^{17}	2.97×10^{17}
ζ_{Cit}	1	1	1	1
v_{sat} (cm/sec)	4.7×10^5	2.3×10^5	1.42×10^5	2.8×10^5

Table 3.6: Modelling parameters for set A 6H-SiC MOSFETs. Value were extracted using experimental data and are used to describe that surface interface trap conditions.

The modelling parameter v_{sat} is extracted from the $I_D - V_{DS}$ data. If the $I_D - V_{GS}$ is in agreement, the linear regions of the $I_D - V_{DS}$ curve are matched automatically. So, the only thing left to do is obtain the v_{sat} parameter that produces agreement between experimental and simulated data. Notice that the obtained v_{sat} values are approximately 30 times smaller than the theoretically expected bulk value of 2×10^7 cm/sec . These results are in agreement with the low field mobility results that are approximately 20 times less than the theoretically expected bulk value of 400 $cm^2/V sec$. See Table 3.6 for optimized modelling values obtained for set A and their average. A comparison of experimental and simulated $I_D - V_{GS}$ and $I_D - V_{DS}$ data for set A devices at room temperature is shown in Figures 3.4 through 3.12.

Simulations for set B have also been performed. Experimentally extracted \bar{D}_{it} values are used as the the midband density of states for this set also, so the only empirical parameter fitted in is N_f . N_f was adjusted until best agreement between simulation and experiment was achieved. For set B devices, the N_f value was fitted in the same manner as that of set A, but no other empirical parameters

	device B1	device B2	device B3
D_c ($cm^{-2} eV^{-1}$)	1.143×10^{13}	1.143×10^{13}	1.143×10^{13}
ξ_c (eV)	0.1107	0.1107	0.1107
N_f (cm^{-2})	(+) 1.51×10^{12}	(+) 6.16×10^{11}	(+) 3.55×10^{11}
n_{Cit} (cm^{-3})	2.97×10^{17}	2.97×10^{17}	2.97×10^{17}
ζ_{Cit}	1	1	1
v_{sat} (cm/sec)	2.8×10^5	2.8×10^5	2.8×10^5

Table 3.7: Modelling parameters for set B 6H-SiC MOSFETs. With the exception of the fixed oxide charge density, values are equal to the averages computed from set A findings.

were optimized. Average empirical parameters were calculated using the value obtained from the simulation of the set A devices. These averages were then used as the empirical value set for simulations of set B devices. A comparison between experimental and simulated data shows that one of the three device simulation produces $I - V$ curves that overestimated the current. Another one underestimated it, and the third fits reasonably well. These results are astonishing given the known process variation among the devices and fact that only the fixed oxide density was optimized. Plots of the set B simulation results are shown in Figures 3.13 through 3.21. See Table 3.7 for empirical parameter values used in set B.

3.5 The Fixed Oxide Charge Discrepancy

It is apparent that the fixed oxide charge values, Q_f , extracted from experiment are not in agreement with those resulting from simulation, so justification of this discrepancy is required. Recalling the earlier discovery of possible underestimation of interface trap causing charge by the CP experiment, this *missing* negative charge must be accounted for if the observed shift in threshold voltage is

	device A1	device A2	device A3
experimental (cm^{-2})	(+)5.31×10 ¹¹	(-)1.05×10 ¹¹	(-)4.78×10 ¹¹
simulated (cm^{-2})	(+)1.18×10 ¹²	(+)7.12×10 ¹¹	(+)3.80×10 ¹¹

Table 3.8: Experimental and simulated values of N_f for set A. A discrepancy exists between the experimentally extracted fixed oxide charge density and the value extracted by simulation due to oversimplification assumed by the charge pumping technique.

	device B1	device B2	device B3
experimental (cm^{-2})	(+)7.39×10 ¹¹	(-)2.56×10 ¹¹	(-)5.03×10 ¹¹
simulated (cm^{-2})	(+)1.51×10 ¹²	(+)6.16×10 ¹¹	(+)3.55×10 ¹¹

Table 3.9: Experimental and simulated values of N_f for set B. A discrepancy exists between the experimentally extracted fixed oxide charge density and the value extracted by simulation due to oversimplification assumed by the charge pumping technique.

to be accurately quantified. The only way to achieve this and maintain the consistency of the system is to include the missing charge as part of the fixed oxide charge value. As a result, when underestimating the negative contribution of interface trap charge to the total surface charge value, the negative contribution of the fixed oxide charge is inherently overestimated.

See Tables 3.8 and 3.9 for simulated and experimentally extracted values of the fixed oxide charge density for set A and B, respectively.

For experimentally extracted values of N_f , 4 of the 6 devices were found to have a negative fixed oxide charge value. The two devices (A1 and B1) having positively calculated Q_f values also have the largest average interface trap density values, meaning that most of the negative charge was accounted for before calculating Q_f . On the other hand, the energy dependent simulation model accounts for the negative charge contribution near the band edges, so Q_f does not have to over compensate for negative charge not previously taken into account. For the

devices studied, I have obtained, through simulation, modelling values for Q_f/q (N_f) which are comparable to other experimental works[47, 14].

3.6 Chapter Summary

In this chapter several 6H-SiC MOSFET devices were presented along with their respective experimental data. Experimentally extracted data was used as a calibration tool for the physics based 6H-SiC MOSFET simulator. Using the simulator I was able to not only reproduce $I-V$ data in agreement with experiment and produce, for the first time, accurate interface trap figures of merit but also identify a potential error produced when performing the charge pumping technique. The noted error causes an overestimation of the fixed oxide charge density when dealing with samples that contain large interface trap density of state values. Using my simulator I was able to identify the error and more accurately quantify the condition of the semiconductor/oxide interface. Because of the results produced in this chapter, I am lead to believe that the mobility degradation due to net interface charge density is considerably higher than any possible degradation due to surface roughness which is in contrast to conclusions reached by Joshi[38]. This assumption will be revisited and justified later in the work.

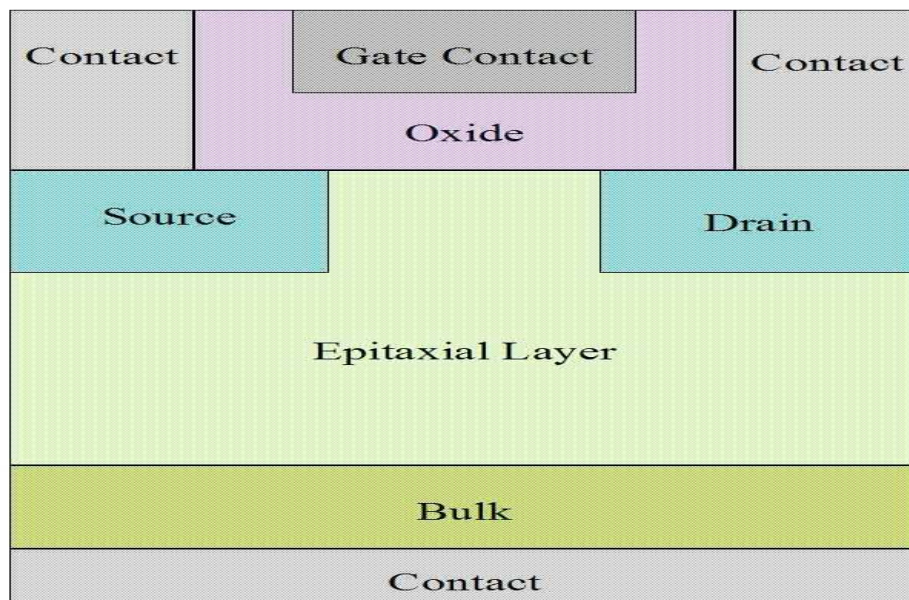


Figure 3.1: Device profile for 6H-SiC MOSFETs studied in this work.

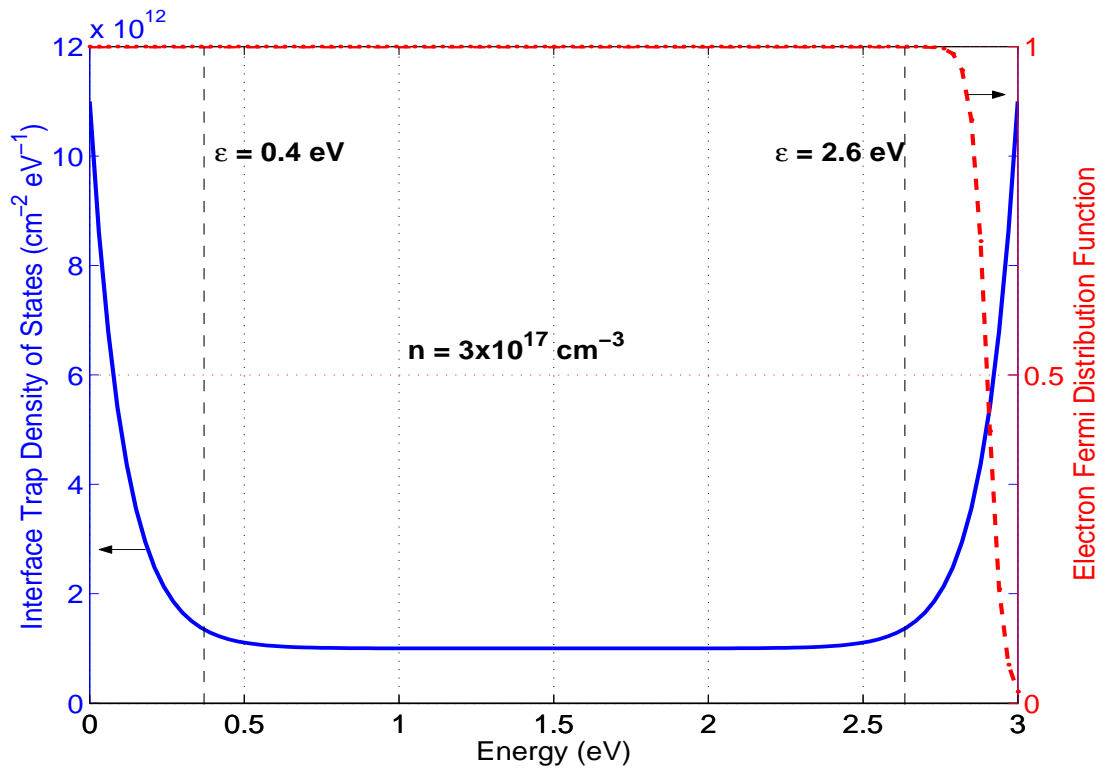


Figure 3.2: Interface trap density of states and electron Fermi distribution with $D_c = D_v = 1 \times 10^{13} \text{ cm}^{-2} \text{ eV}^{-1}$, $\xi_c = \xi_v = 0.11 \text{ eV}$, $D_{it0} = 1 \times 10^{12} \text{ cm}^{-2} \text{ eV}^{-1}$, and $n = 3 \times 10^{17} \text{ cm}^{-3}$. The Fermi distribution is representation of an inverted 6H-SiC MOSFET.

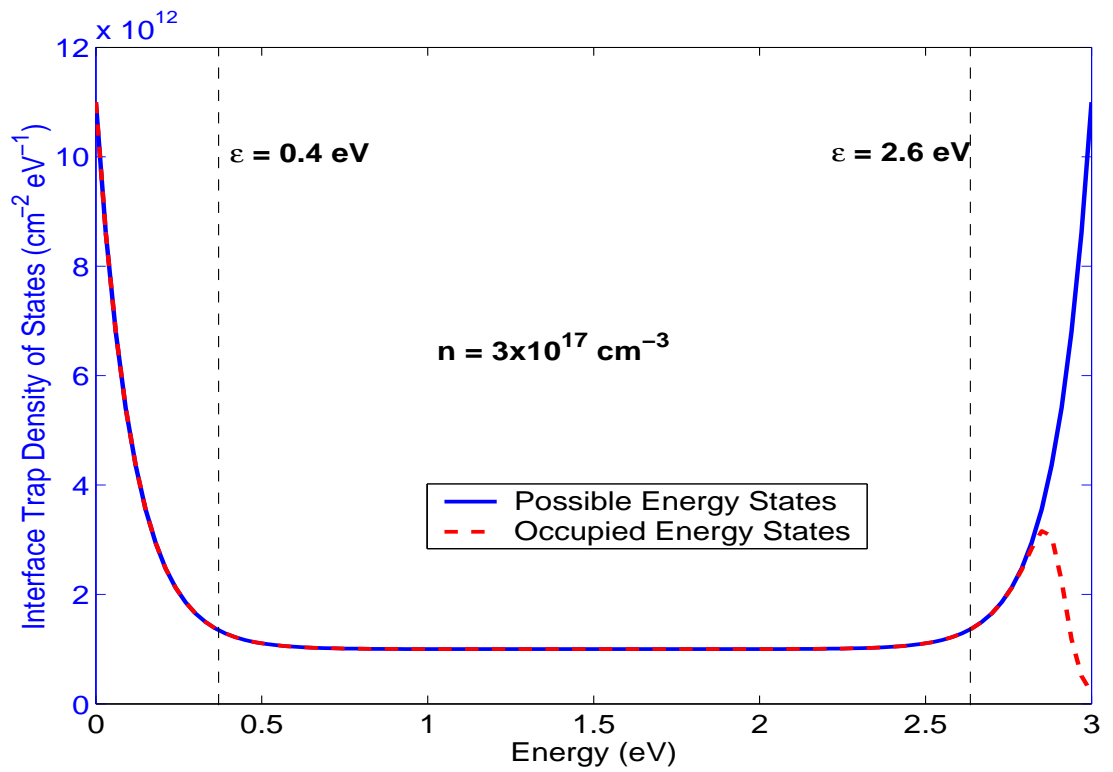


Figure 3.3: Product of interface trap density of states profile with and electron Fermi distribution with $D_c = D_v = 1 \times 10^{13} \text{ cm}^{-2} \text{ eV}^{-1}$, $\xi_c = \xi_v = 0.11 \text{ eV}$, $D_{ito} = 1 \times 10^{12} \text{ cm}^{-2} \text{ eV}^{-1}$, and $n = 3 \times 10^{17} \text{ cm}^{-3}$. The Fermi distribution is representation of an inverted 6H-SiC MOSFET. Results show that there are electrons present past 2.6 eV .

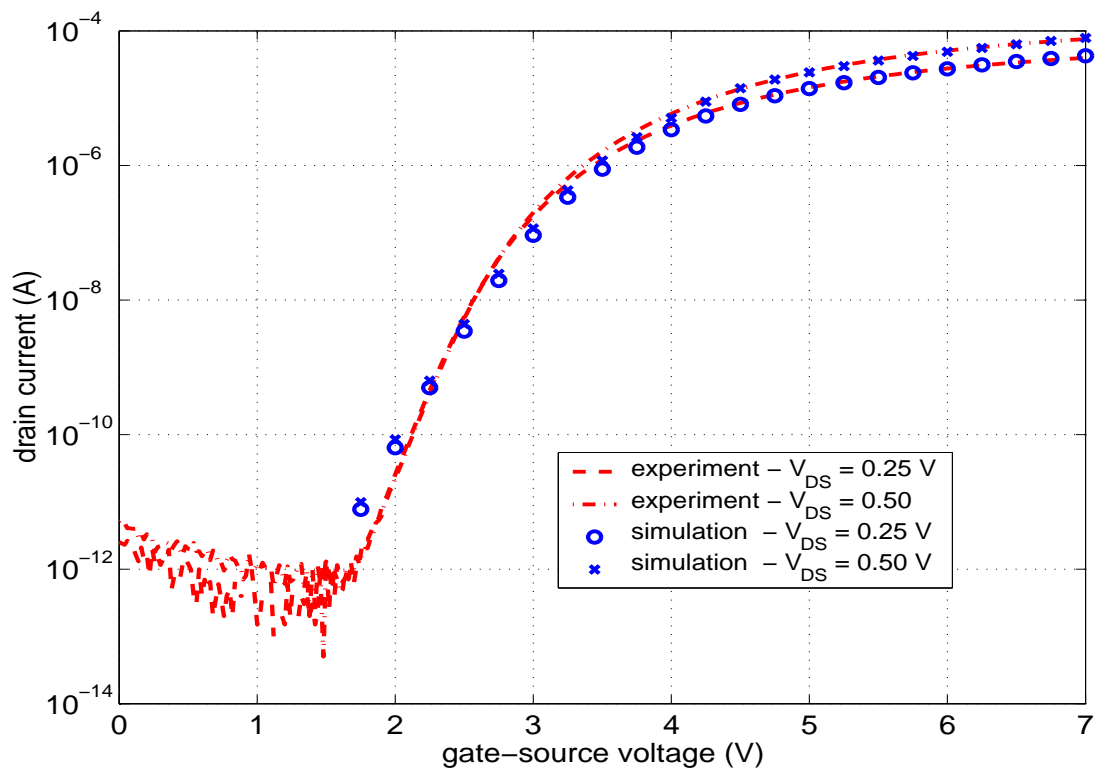


Figure 3.4: Log plot of I_D vs. V_{GS} for device A1 at room temperature. Simulation data is in agreement with experiment throughout the entire range of gate-source voltages simulated.

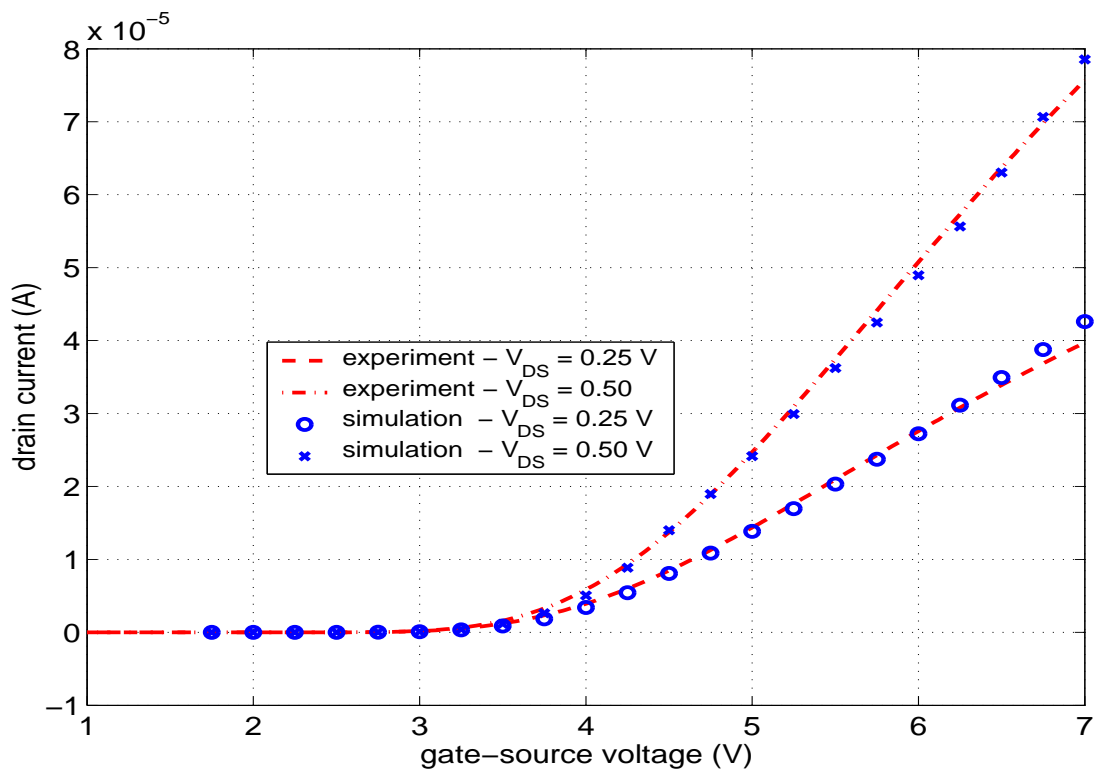


Figure 3.5: Linear plot of I_D vs. V_{GS} for device A1 at room temperature. Simulated and experimental results are in agreement. Simulation was conducted using optimized modelling values.

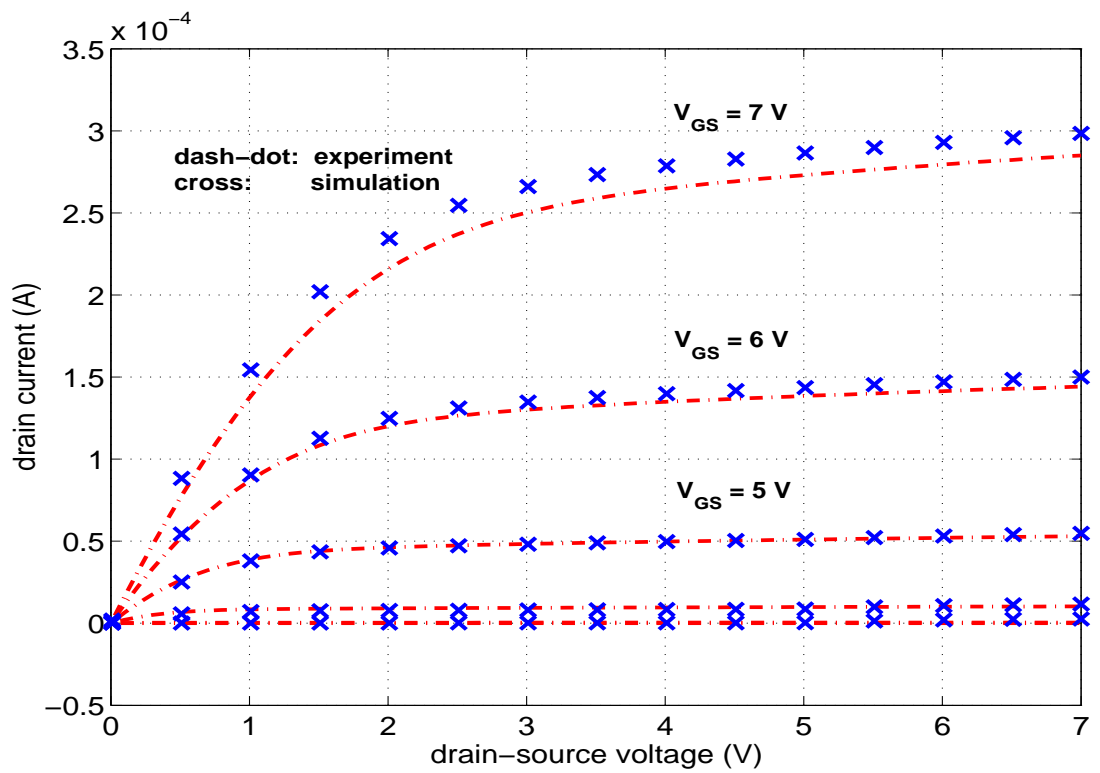


Figure 3.6: I_D vs. V_{DS} for device A1 at room temperature. Simulated and experimental results are in agreement. Simulation was conducted using optimized modelling values.

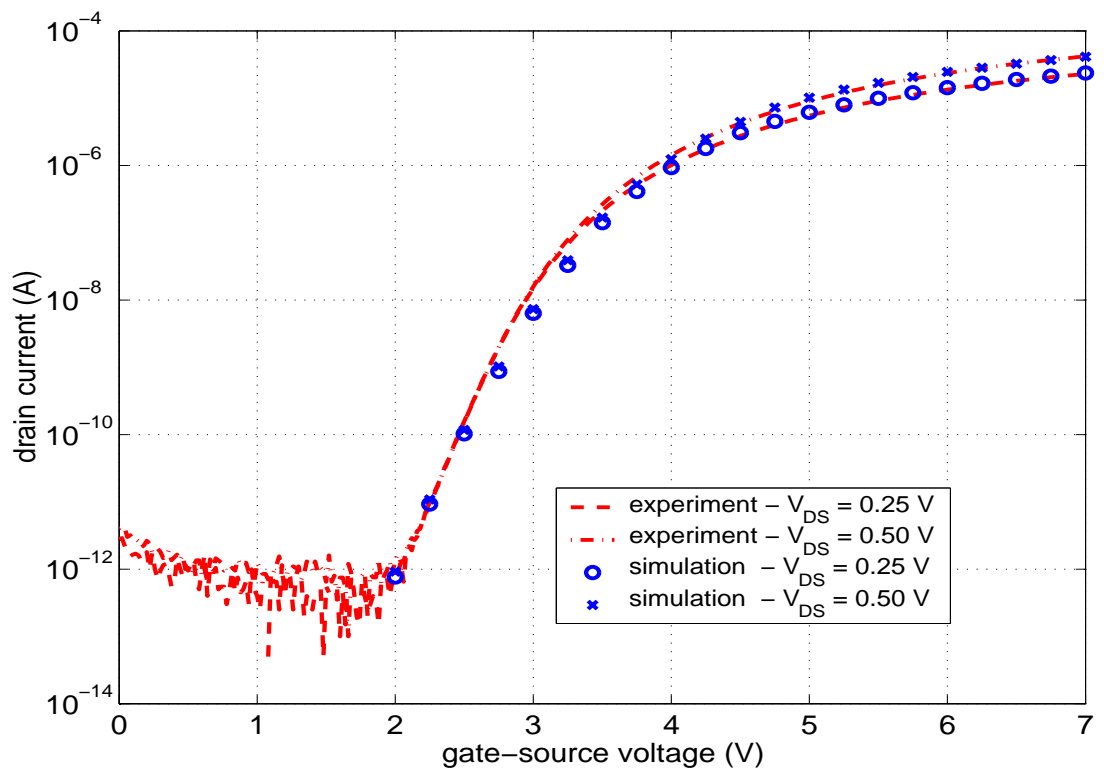


Figure 3.7: Log plot of I_D vs. V_{GS} for device A2 at room temperature. Simulation data is in agreement with experiment throughout the entire range of gate-source voltages simulated.

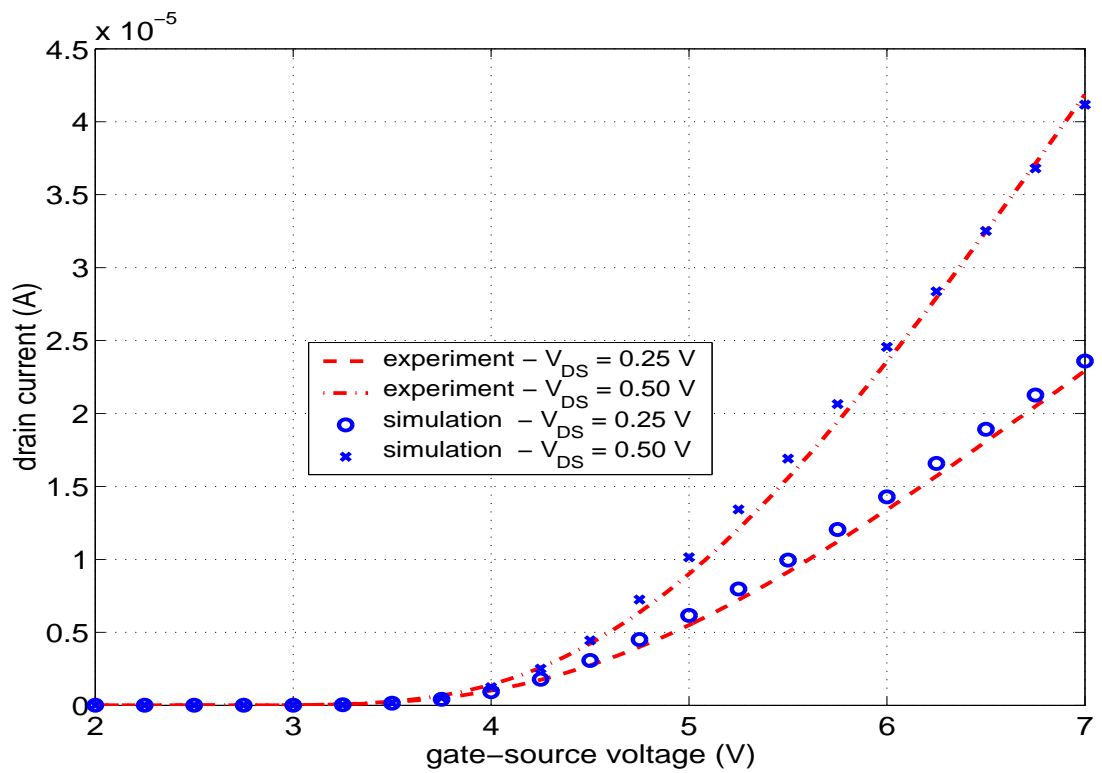


Figure 3.8: Linear plot of I_D vs. V_{GS} for device A2 at room temperature. Simulated and experimental results are in agreement. Simulation was conducted using optimized modelling values.

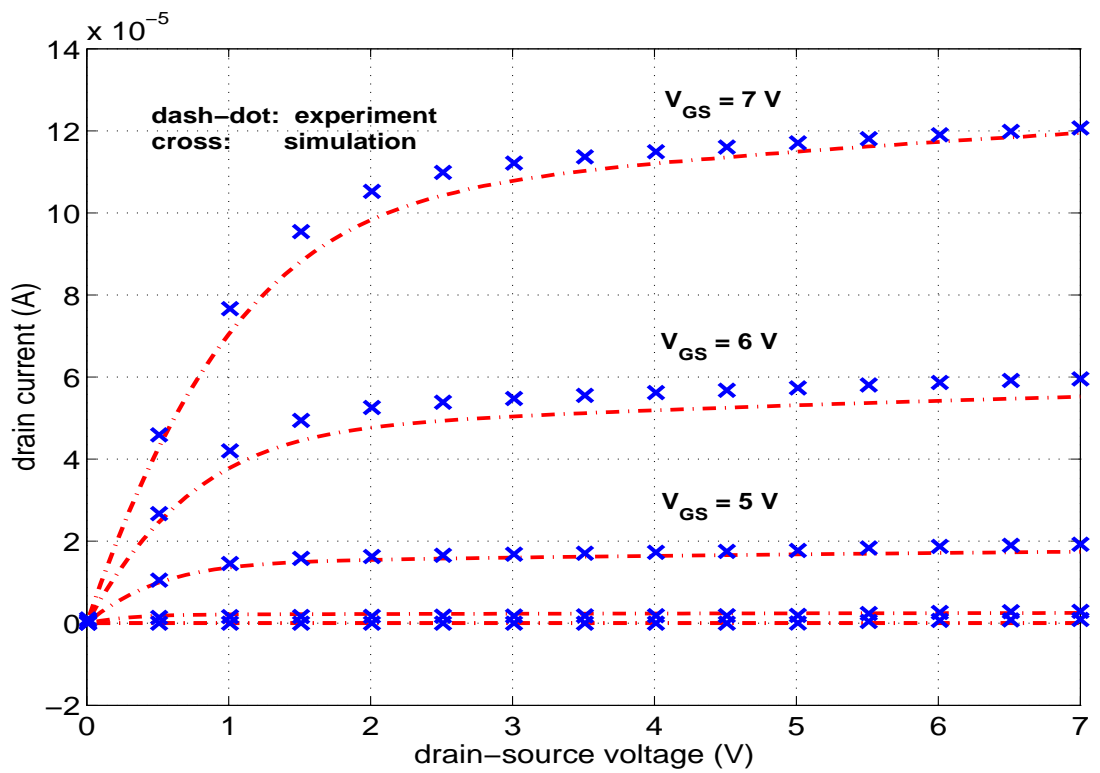


Figure 3.9: Linear plot of I_D vs. V_{DS} for device A2 at room temperature. Simulated and experimental results are in agreement. Simulation was conducted using optimized modelling values.

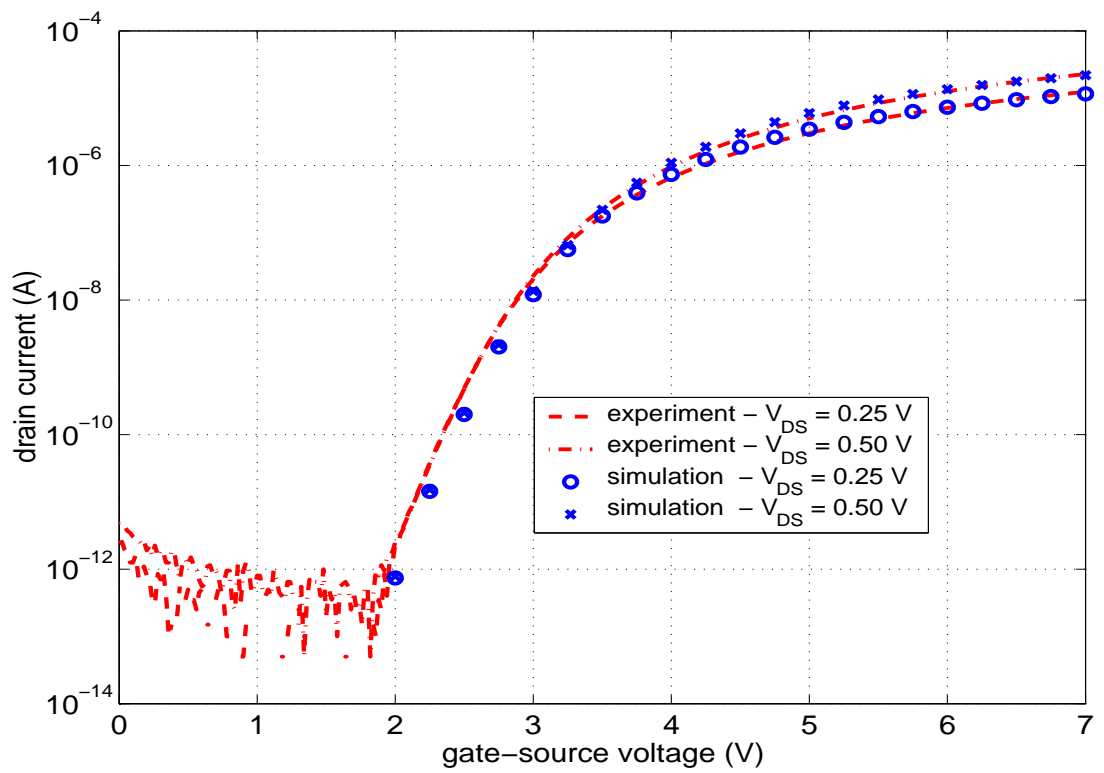


Figure 3.10: Log plot of I_D vs. V_{GS} for device A3 at room temperature. Simulation data is in agreement with experiment throughout the entire range of gate-source voltages simulated.

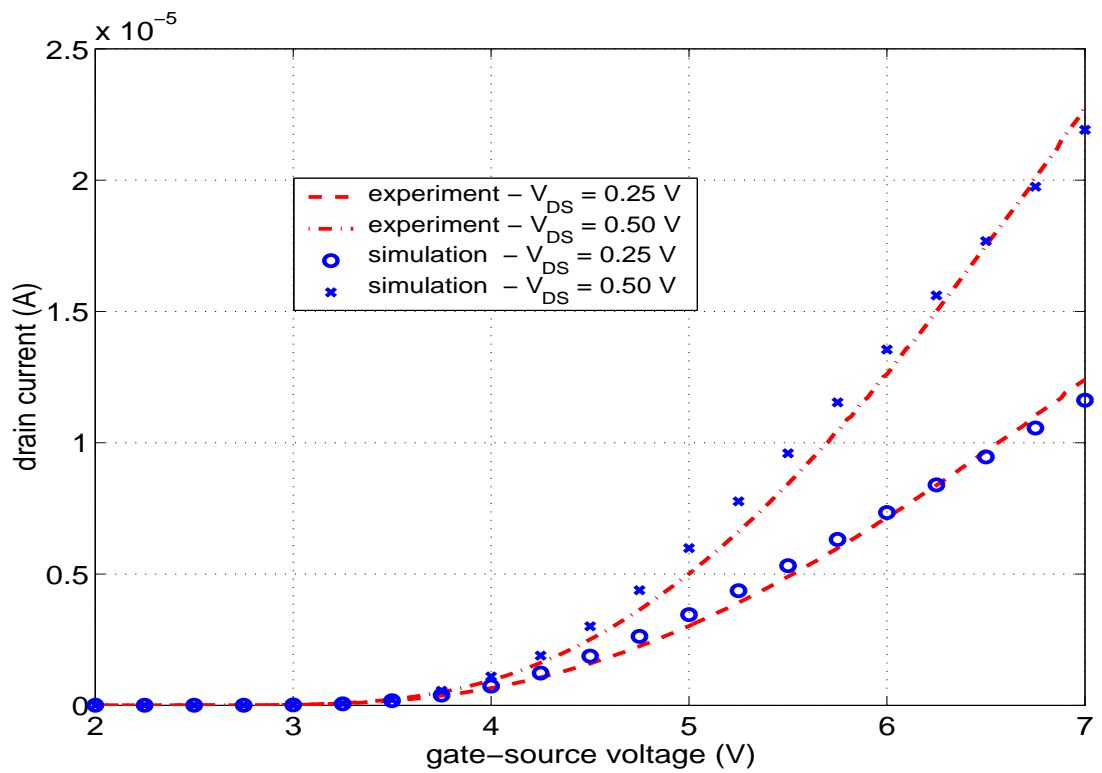


Figure 3.11: Linear plot of I_D vs. V_{GS} for device A3 at room temperature. Simulated and experimental results are in agreement. Simulation was conducted using optimized modelling values.

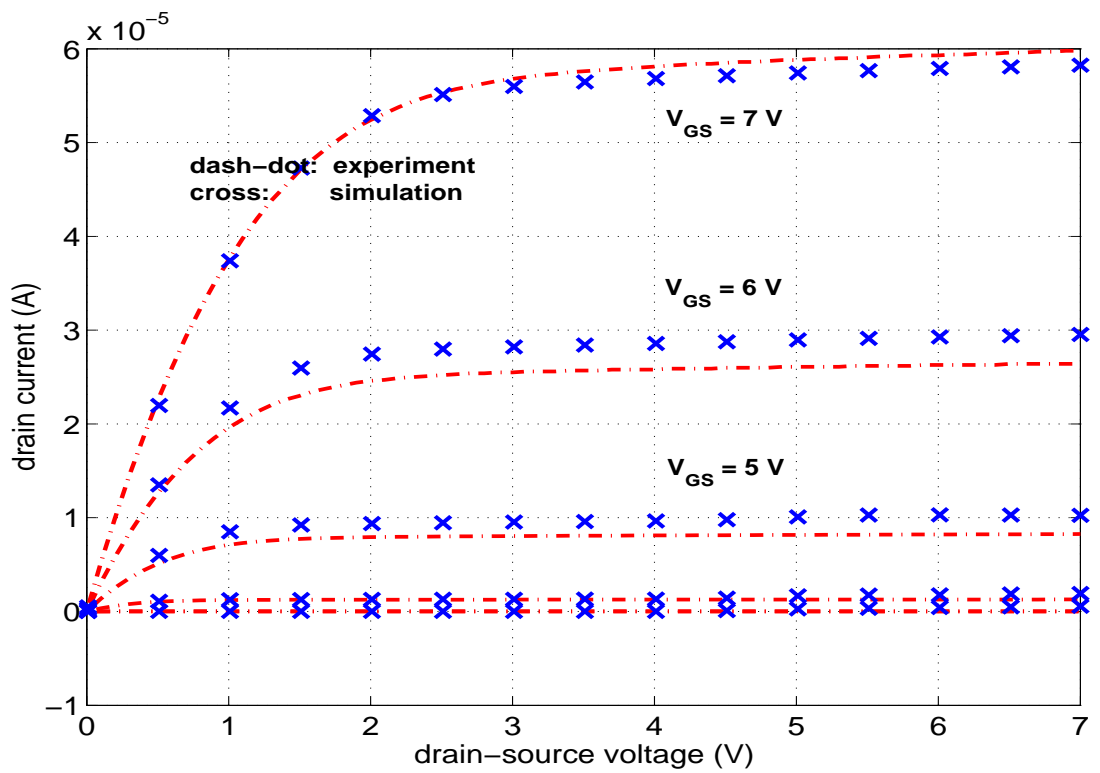


Figure 3.12: I_D vs. V_{DS} for device A3 at room temperature. Simulated and experimental results are in good agreement. Simulation was conducted using optimized modelling values.

This page intentionally left blank.

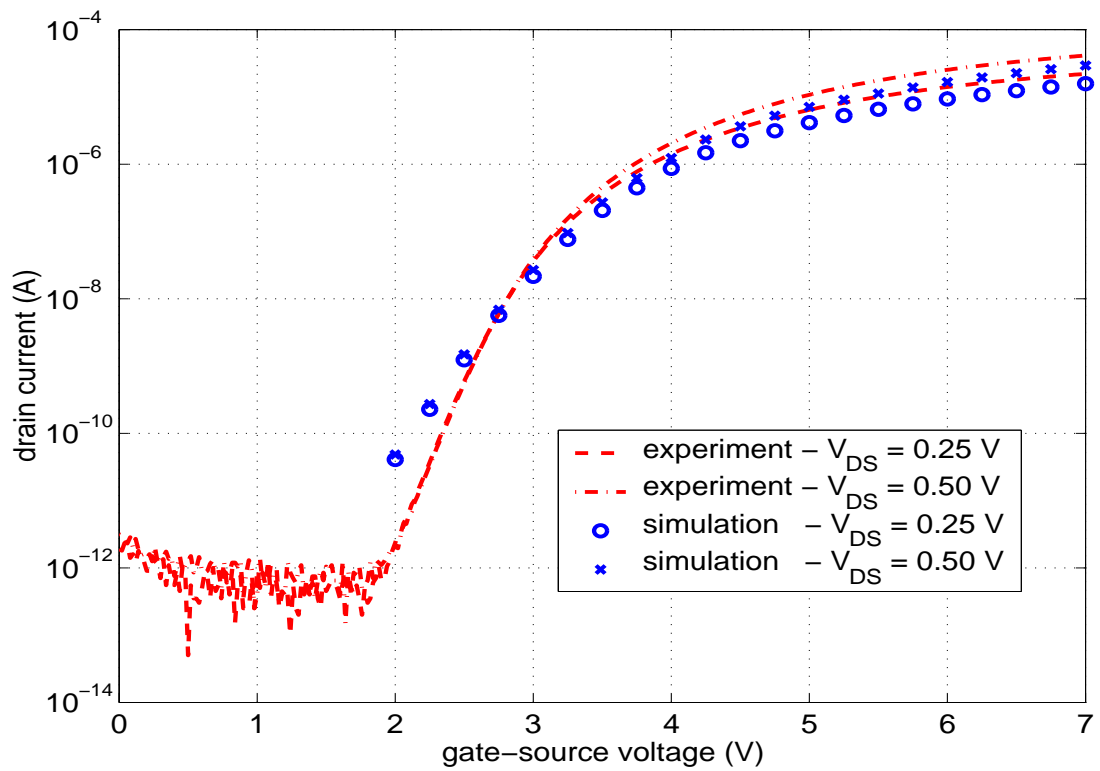


Figure 3.13: Log plot of I_D vs. V_{GS} for device B1 at room temperature. Simulation was conducted using non-optimized modelling values and underestimates the experimental results. Despite the mismatch, the results are favorable considering the surface quality variation among the devices.

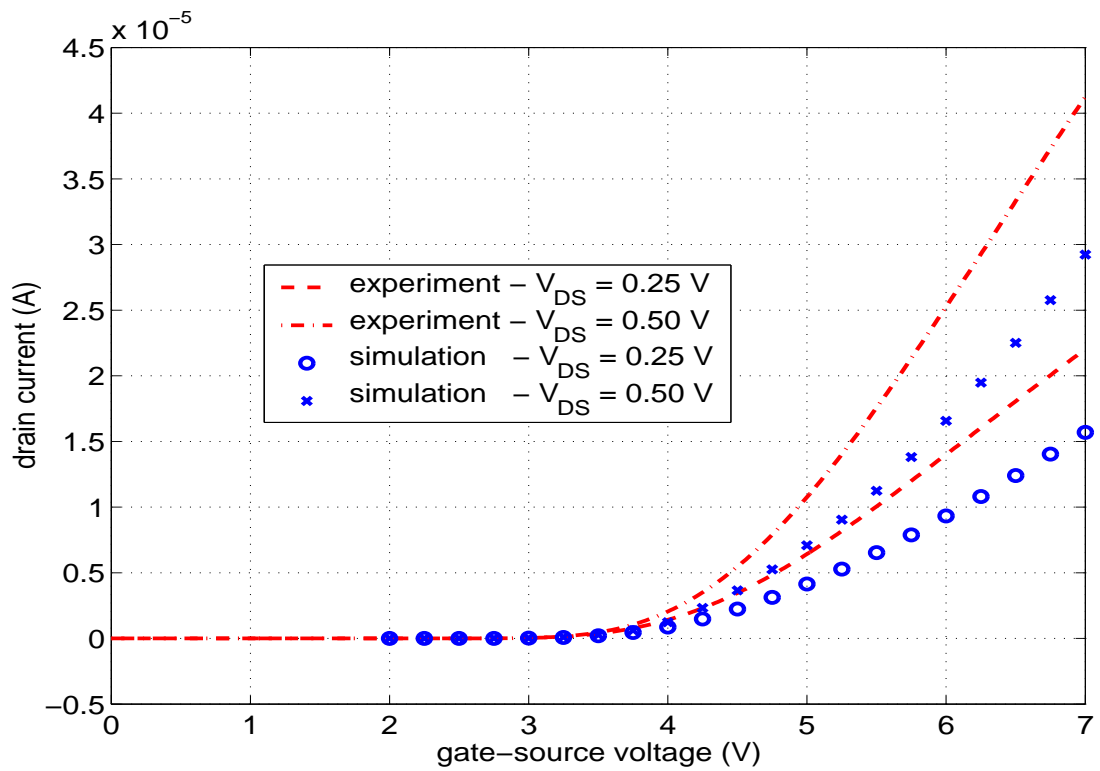


Figure 3.14: Linear plot of I_D vs. V_{GS} for device B1 at room temperature. Simulation was conducted using non-optimized modelling values and underestimates the experimental results. Despite the mismatch, the results are favorable considering the surface quality variation among the devices.

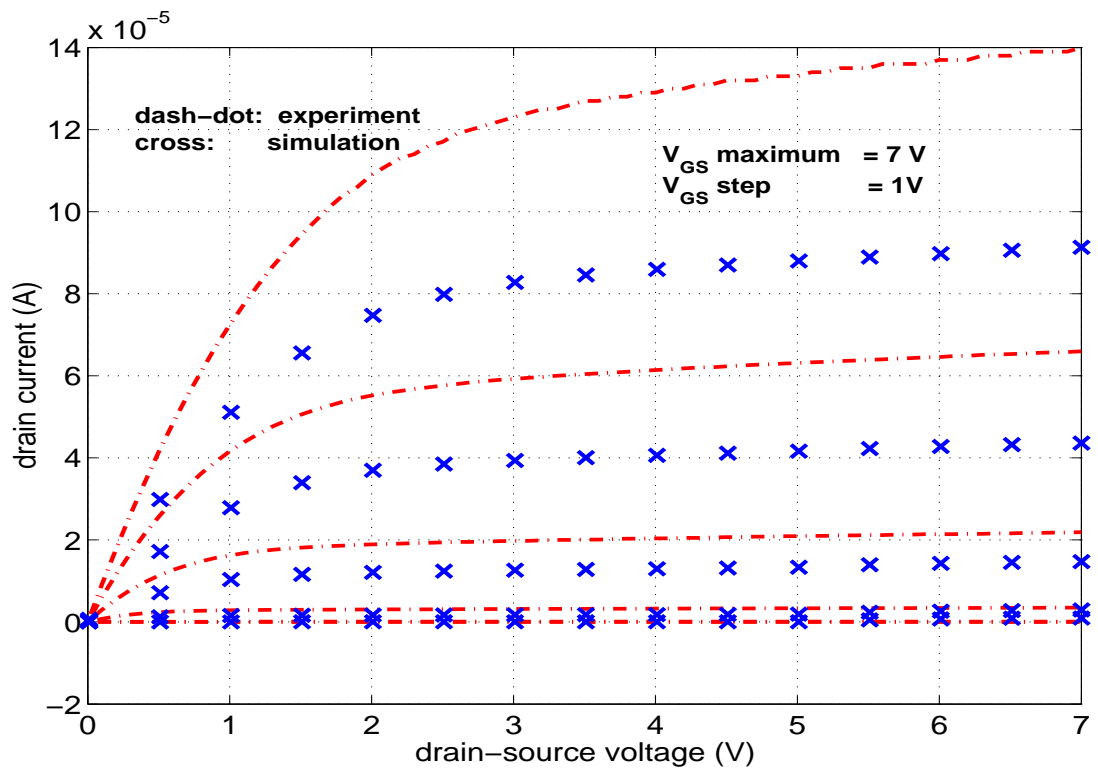


Figure 3.15: I_D vs. V_{DS} for device B1 - room temperature. Simulation was conducted using non-optimized modelling values and underestimates the experimental results. Despite the mismatch, the results are favorable considering the surface quality variation among the devices.

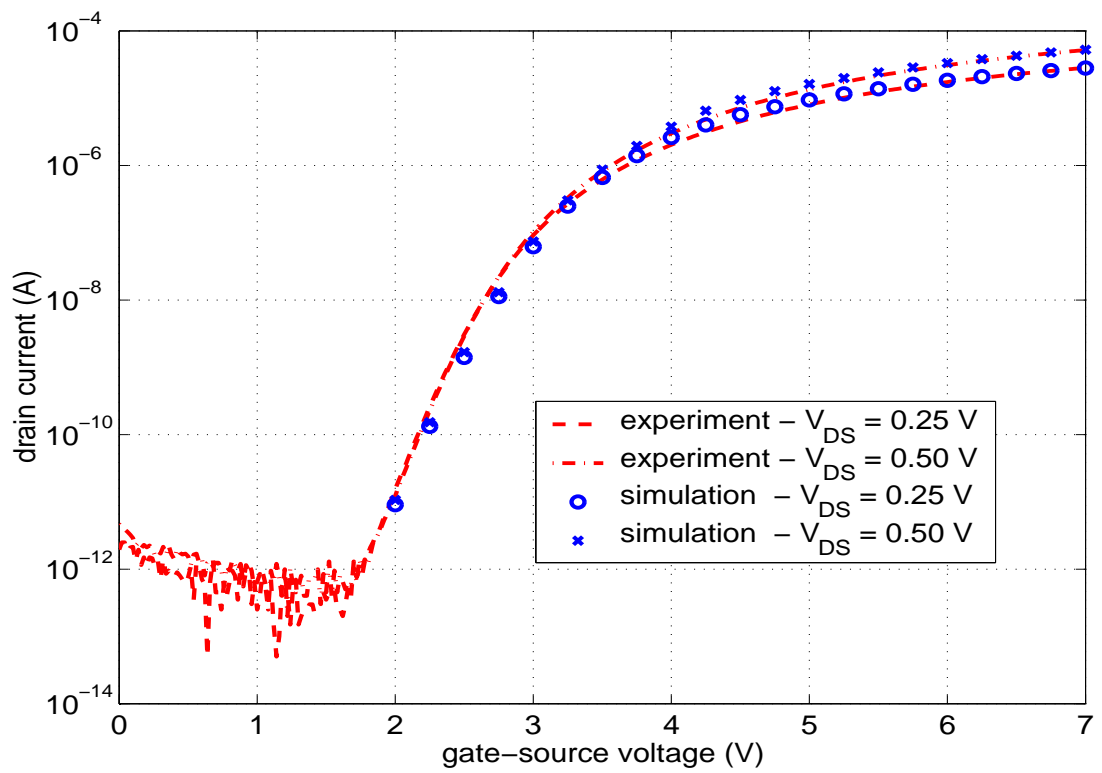


Figure 3.16: Log plot of I_D vs. V_{GS} for device B2 at room temperature. Simulated and experimental results are in good agreement. Simulation was conducted using non-optimized modelling values.

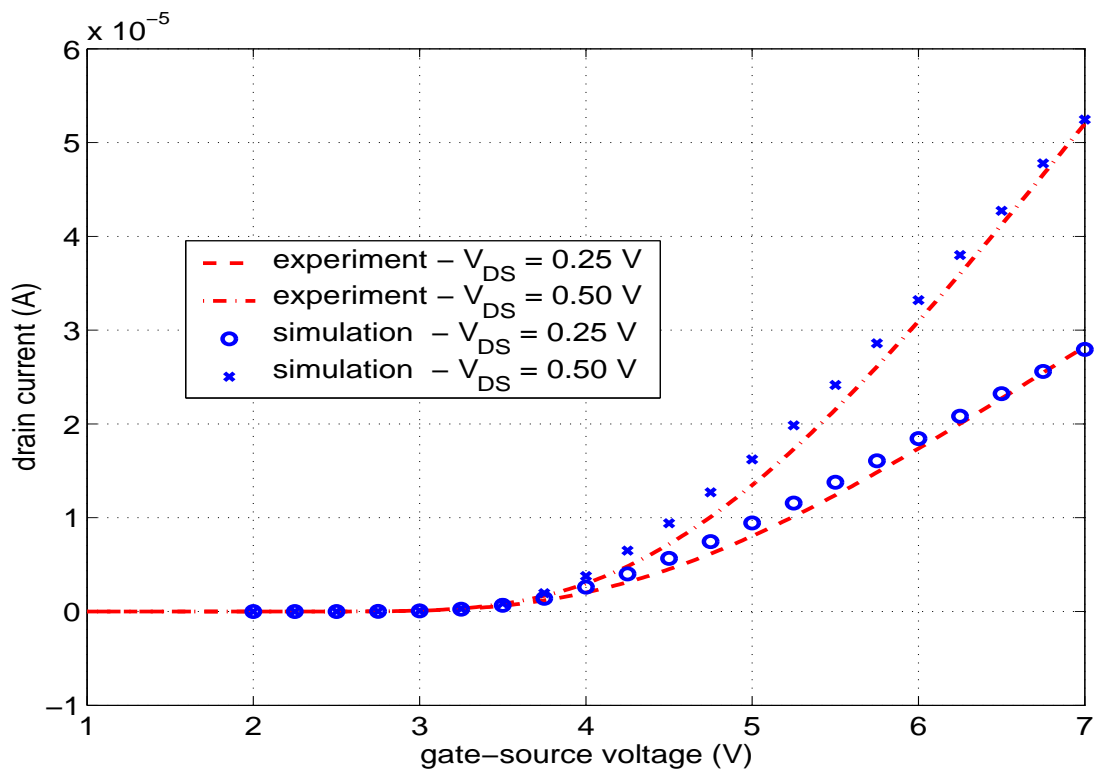


Figure 3.17: Linear plot of I_D vs. V_{GS} for device B2 at room temperature. Simulated and experimental results are in good agreement. Simulation was conducted using non-optimized modelling values.

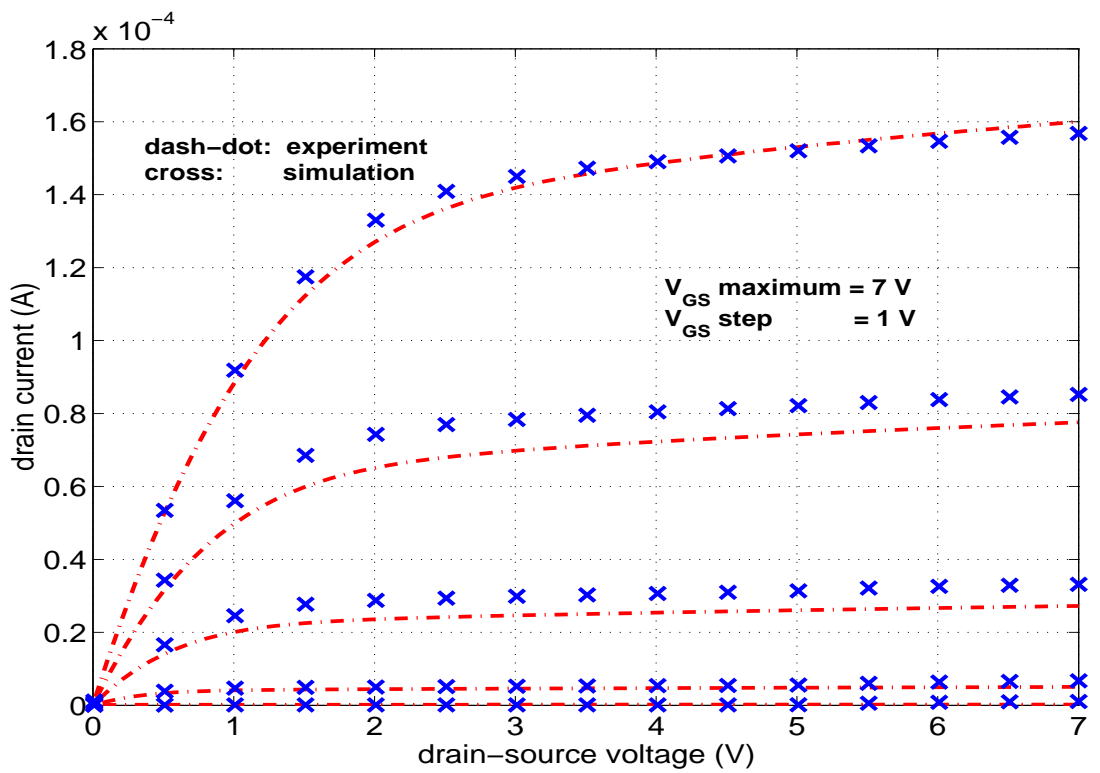


Figure 3.18: I_D vs. V_{DS} for device B2 at room temperature. Simulated and experimental results are in good agreement. Simulation was conducted using non-optimized modelling values.

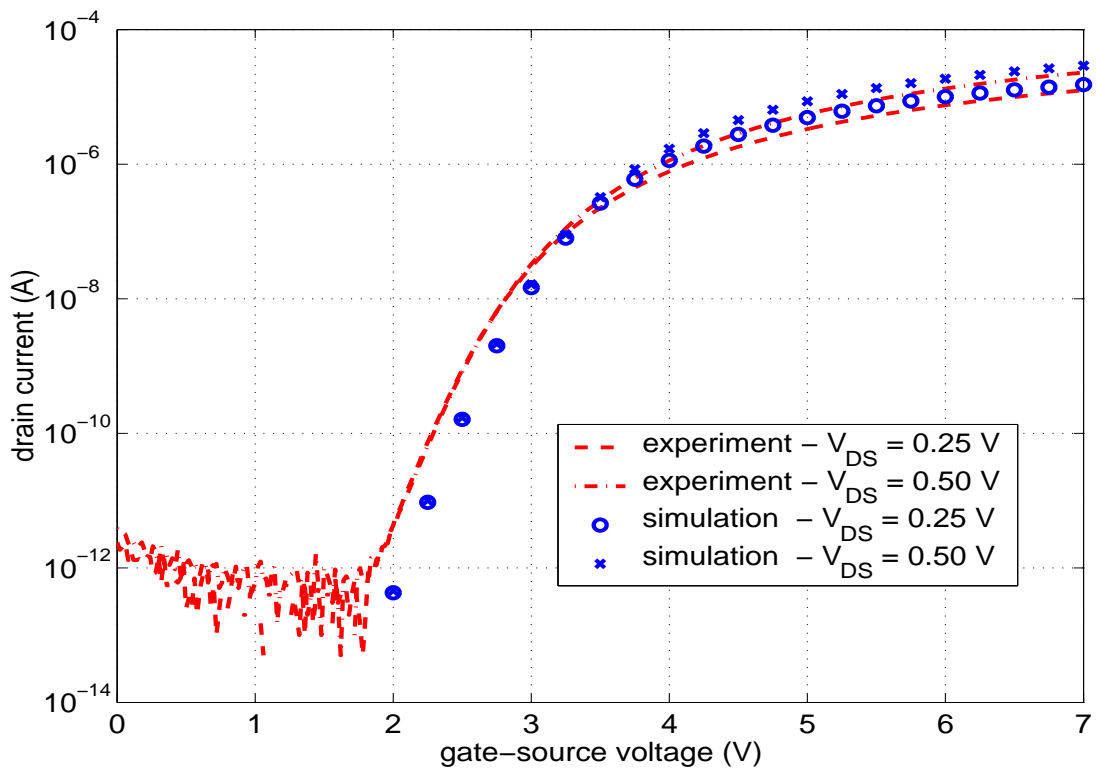


Figure 3.19: Log plot of I_D vs. V_{GS} for device B3 at room temperature. Simulation was conducted using non-optimized modelling values and overestimates the experimental results. Despite the mismatch, the results are favorable considering the surface quality variation among the devices.

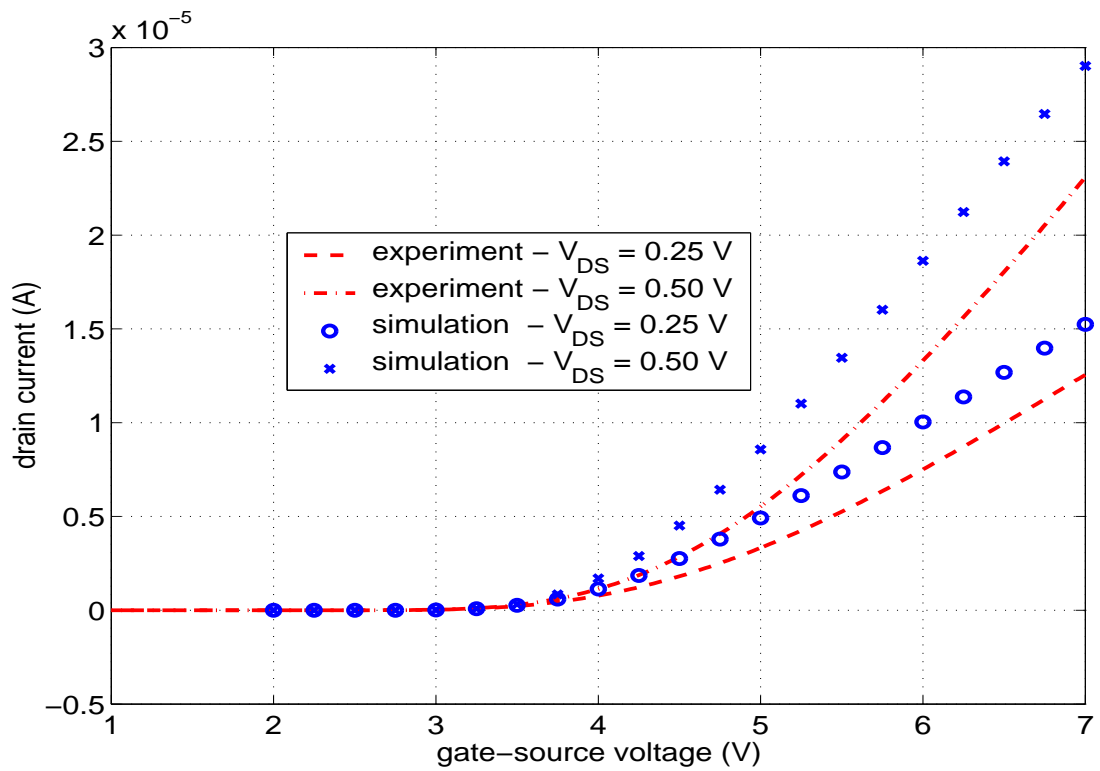


Figure 3.20: Linear plot of I_D vs. V_{GS} for device B3 at room temperature. Simulation was conducted using non-optimized modelling values and overestimates the experimental results. Despite the mismatch, the results are favorable considering the surface quality variation among the devices.

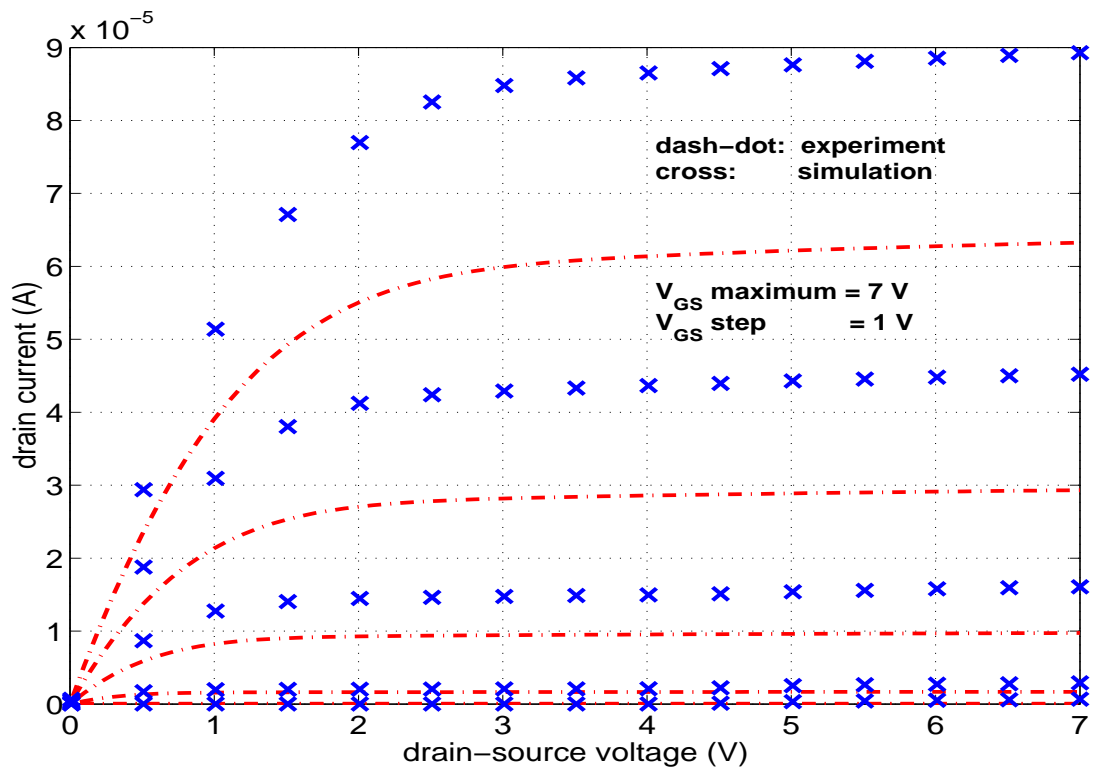


Figure 3.21: I_D vs. V_{DS} for device B3 at room temperature. Simulation was conducted using non-optimized modelling values and overestimates the experimental results. Despite the mismatch, the results are favorable considering the surface quality variation among the devices.

High Temperature Modelling and Beyond

In the previous chapter, I used the drift-diffusion-based simulator to investigate and further characterize the performance of real world 6H-SiC MOSFETs. By matching experimentally observed electrical characteristics of the MOSFETs, I have shown that the simulator can be used to provide insight to current state-of-the-art silicon carbide devices. Demonstrating the validity of the simulator at room temperature, I have taken on the tasks of extending the realm of the simulator into high temperature modelling and characterizing of next generation 6H-silicon carbide MOSFETs. In order to achieve this, lattice self-heating must be added to the simulation model, and calibration must be done for high temperature environments. I accomplish this by examining and simulating the performance of the 6H-SiC MOSFETs at elevated temperatures, simulating the effects of improved surface quality, and examining the possible scalability of 6H-SiC MOSFETs.

4.1 Heat Conduction

When modelling devices at high temperatures, it is crucial that effects due to ambient temperature and lattice self-heating are considered. The isothermal drift-diffusion model presented thus far can account for changes in device performance due to ambient temperature variation provided that temperature dependent model parameters are available. However, it does not explicitly consider device performance degradation due to lattice self-heating. For this reason the isothermal drift-diffusion equations must be amended, and the heat conduction equation must be included to the semiconductor device model. The equation used to model semiconductor heat conduction is given by

$$c_v \frac{\partial T}{\partial t} = \vec{\nabla}_r \cdot \{\kappa(T) \vec{\nabla}_r T\} + H \quad (4.1)$$

where T is the semiconductor lattice temperature, c_v is heat capacity, κ is thermal conductivity, and H is the heat generation rate.

According to Wachutka [48], the semiconductor heat generation rate for steady-state operation can be expressed by the following:

$$H = \frac{|\vec{J}_n|^2}{\mu_n(T)n(T)} + \frac{|\vec{J}_p|^2}{\mu_p(T)p(T)} + q(R(T) - G(T))[\psi_p - \psi_n + T(P_n + P_p)] - T(\vec{J}_n \cdot \vec{\nabla} P_n - \vec{J}_p \cdot \vec{\nabla} P_p), \quad (4.2)$$

where \vec{J}_n and \vec{J}_p are the current densities for electron and holes respectively, μ_n and μ_p are the electron and hole mobilities, respectively, R is the net recombination rate

of carrier pairs, G is the net generation rate of carrier pairs; and $\psi_{n,p}$ and $P_{n,p}$ are the quasi-Fermi potential and thermoelectric power of electrons and holes, respectively.

Conventional and silicon-on-insulator (SOI) MOSFET simulation results by Dallmann [49] indicate that nearly all of the heat is generated by means of lattice self-heating. As a result, the heat generation rate can be simplified to the expression

$$H = H_{Joule} = (\vec{J}_n + \vec{J}_p) \cdot \vec{E} \quad (4.3)$$

where \vec{E} is the electric field. In order to account for the release of heat due to electron-hole recombination, an additional term is added to the heat generation rate. With the new term, this expression is given as

$$H = H_{Joule} = (\vec{J}_n + \vec{J}_p) \cdot \vec{E} + E_g(T)(R(T) - G(T)) \quad (4.4)$$

where $E_g(T)$ is the temperature dependent energy bandgap and $R - G$ is the net electron-hole recombination rate.

4.1.1 Thermal Conductivity

Experimental data examined by [50] reveals that the thermal conductivity of a pure single crystal semiconductor is zero near 0 Kelvin and rises approximately exponentially to a maximum near 20 K, falls slightly faster than $1/T$ to about 500 K, and then varies as $1/T$ to the melting point[50]. Experimental results also disclose that the thermal conductivity of highly doped semiconductor material is less than that of the intrinsic material. This is most likely due the increased probability of

phonon-electron scattering. According to Maycock, a good rule of thumb for highly doped samples is to decrease the thermal conductivity value by 20 percent [50]. For simulation results presented in this work, the following thermal conductivity model is used [19]

$$\kappa(T) = \alpha_T \kappa_o \left(\frac{T}{300} \right)^{-\gamma_T}$$

where α_T is defined by

$$\alpha_T = \frac{1}{1 + \left(\frac{|C|}{2.8 \times 10^{19}} \right)}$$

and has been added to the model in [19] in order to account for thermal conductivity degradation due to heavy doping. κ_o ($4.9 \frac{W}{cm K}$ for $6H$ and $3.7 \frac{W}{cm K}$ for $4H$) is the thermal conductivity at 300 K; γ_T is the power law degradation coefficient of $\kappa(T)$, and C is the net ionized doping concentration. The model is valid in a range of 300 to 600 Kelvin.

Most of the internal energy in the semiconductor is stored via lattice vibrations (phonons). How much internal energy can be stored by the phonons per unit temperature is defined as the heat capacity, c_v , given by

$$c_v = \frac{\partial U}{\partial T}$$

where U is the net internal energy, and T is the lattice temperature. For silicon carbide the heat capacity is approximately $2.25 \frac{J}{cm^{-3} K}$ at 300 Kelvin.

4.1.2 Self-Consistency of Drift-Diffusion and Heat Flow

In order to fuse drift-diffusion and heat conduction into a working model capable of simulating temperature dependent semiconductor device phenomena, an additional constraint must be added – *localized temperature equilibrium*. Localized temperature equilibrium states that, though the temperature within the device or material may stray from the ambient temperature drastically, the temperature of electrons, holes, and lattice at any particular point in space, *e. g.* \vec{r}_0 , is the same. In other words,

$$T_n(\vec{r}_0) = T_p(\vec{r}_0) = T_L(\vec{r}_0) = T(\vec{r}_0) \quad (4.5)$$

where T_n is the electron temperature, T_p is the hole temperature, and T_L is the semiconductor lattice temperature. Imposing the localized temperature constraint, the following model is obtained,

$$\begin{aligned} \vec{\nabla}_r \cdot \{\epsilon \vec{\nabla}_r \phi\} &= -q\{n - p - C(T)\} \\ q \frac{\partial n}{\partial t} &= \vec{\nabla}_r \cdot \vec{J}_n(T) - q(R(T) - G(T)) \\ -q \frac{\partial p}{\partial t} &= \vec{\nabla}_r \cdot \vec{J}_p(T) + q(R(T) - G(T)) \\ c_v \frac{\partial T}{\partial t} &= \vec{\nabla}_r \cdot \{\kappa(T) \vec{\nabla}_r T\} + H(T) \end{aligned} \quad (4.6)$$

where

$$\vec{J}_n(T) = -q\{n\mu_n(T)\vec{\nabla}_r\phi - q\vec{\nabla}_r[nD_n(T)]\} \quad (4.7)$$

$$\vec{J}_p(T) = -q\{p\mu_p(T)\vec{\nabla}_r\phi + q\vec{\nabla}_r[pD_p(T)]\}$$

$$H(T) = \{\vec{J}_n(T) + \vec{J}_p(T)\} \cdot \{-\vec{\nabla}_r\phi\} + E_g(T)\{R(T) - G(T)\}.$$

4.1.3 High Temperature Modelling

For the sake of clarity, the temperature dependence of several previously mentioned parameter models was omitted. At this time, the temperature dependency is given for the following: bandgap, intrinsic carrier concentration, minority carrier lifetime, impact ionization generation, bulk mobility, saturation velocity, and boundary conditions.

Bandgap and Intrinsic Carrier Concentration Modelling

The bandgap is by far the most well known material characteristic of any semiconductor material. This is because the band structure - from which the bandgap is extracted - determines all of the material properties mentioned up to this point. The bandgap represents the distance from the valence band energy maximum to the conduction band energy minimum, and this energy distance has a direct effect on the number of electron and hole pairs that are available to roam the conduction and valence bands, respectively. In this work temperature dependence of the bandgap energy is modelled only to the first order and given by the following:

$$E_g(T) = E_{g0} + \alpha_g(T - 300).$$

	6H-SiC	4H-SiC
E_{g0} (eV)	3.0	3.23
α_g ($\frac{eV}{K}$)	-3.3×10^{-4} [21]	same as 6H

Table 4.1: Bandgap model values for 6H- and 4H-silicon carbide.

See Table 4.1 for bandgap values.

The intrinsic carrier concentration of a semiconductor material is approximately equal to

$$n_i(T) = \sqrt{np} = \sqrt{N_c(T)N_v(T)} \exp\left(\frac{-E_g(T)}{2k_B T}\right).$$

where $N_c(T)$ and $N_v(T)$ are the effective density of states in the conduction band and valence band, respectively, and $E_g(T)$ is the temperature dependent the bandgap energy discussed above. Effective density of states values are obtained using the following well known equations

$$N_c(T) = 2 \left(\frac{2\pi m_{de}^* k_B T}{h^2} \right) M_c$$

and

$$N_v(T) = 2 \left(\frac{2\pi m_{dh}^* k_B T}{h^2} \right).$$

m_{de}^* is the density of states effective mass for electrons (holes) in the conduction (valence) band, M_c (3 for SiC) is the number of equivalent conduction band valleys in the Brillouin zone, and m_0 is the rest mass of an electron.

Minority Carrier Lifetime and Impact Ionization Generation

Mentioned in the previous chapter, the minority carrier lifetimes play a critical role in computing the recombination rate due to traps in the center of the bandgap. Shown below is the enhanced, temperature dependent version of the minority carrier lifetime model.

$$\tau_{n,p}(T) = \frac{\tau_{no,po} \left(\frac{T}{300}\right)^{\gamma_{n,p}}}{1 + \left(\frac{N_d^+(T) + N_a^-(T)}{N_{n,p}^{ref}}\right)^{\alpha_{n,p}}}, \quad (4.8)$$

As with recombination, impact ionization generation is also affected by temperature. Its dependence is shown below.

$$G^{II}(T) = \frac{1}{q} \left(\alpha_n(T) |\vec{J}_n| + \alpha_p(T) |\vec{J}_p| \right) \quad (4.9)$$

$$(4.10)$$

where

$$\alpha_{n,p}(T) = \alpha_{n,p}^{\infty}(T) \exp\left(\frac{-b_{n,p}(T)}{|\vec{E}|}\right). \quad (4.11)$$

$G^{II}(T)$ is the net impact ionization generation rate, $\alpha_{n(p)}(T)$ is the per unit length generation coefficient for electrons (holes), and $b_{n(p)}(T)$ is the electric field at which impact ionization generation becomes significant. This particular model is presented in [24].

Bulk Mobility and Saturation Velocity

Both acoustic and optical phonon scattering increase with temperature. Consequently, both bulk mobility and saturation velocity decrease with temperature. The simulator discussed in this work use a power law dependency in order to model the degrading temperature effects on bulk mobility and saturation velocity. These new forms as shown below.

$$\mu_b = \frac{\mu_{max} \left(\frac{300}{T}\right)^{\eta_b}}{1 + \left(\frac{N_d^+(T) + N_a^-(T)}{N_{ref}}\right)^{\gamma_b}} \quad (4.12)$$

$$v_{sat} = v_{sat} \left(\frac{300}{T}\right)^{\eta_s} \quad (4.13)$$

η_b equals 2.4 [6], and η_s equals 2.0.

Boundary Conditions

According to Wachutka[48], when dealing with ideal Ohmic contacts, the semiconductor thermal conductivity κ_{semi} and internal temperature T of the semiconductor device is related to the ambient temperature T_o by the following:

$$\kappa(T) \frac{\partial T}{\partial N_{semi}} = h_{semi} (T_o - T) \quad (4.14)$$

where $\frac{\partial T}{\partial N_{semi}}$ is the derivative of the temperature T in the direction normal to the semiconductor-contact junction. h_{semi} is the heat transfer coefficient between the semiconductor and the ambient medium.

Another boundary condition is imposed on heat that transfers from the semiconductor or oxide of the device to the ambient medium. The condition is expressed by

$$\kappa_{mat} \frac{\partial T}{\partial N_{mat}} = h_{mat} (T_o - T) \quad (4.15)$$

where $\frac{\partial T}{\partial N_{mat}}$ is the derivative of the temperature T in the direction normal to the material-ambient junction, and h_{mat} is the heat transfer coefficient between the *material* (semiconductor or oxide) and the ambient medium.

Gauss' law is used to define the boundary condition for electric field as it transfers from the semiconductor to the insulator. A similar condition applies to the temperature as it transfers from one material to another and is expressed by the following:

$$\kappa_{semi}(T) \frac{\partial T}{\partial N_{semi}} - \kappa_{ox}(T) \frac{\partial T}{\partial N_{ox}} = H_{surf} \quad (4.16)$$

where H_{surf} is the effective surface heating at the insulator/semiconductor interface. For the simulation work presented in the dissertation, $H_{surf} = 0$.

Because the temperature at the device boundary may change while solving for the solution to the drift-diffusion heat flow equations, it is important that the quasi-neutral condition of the electrons and holes at the Ohmic contacts remain consistent with the possible change in temperature. As a result, the carrier boundaries at the contacts must be temperature dependent. They are defined as follows:

$$n(T) = \frac{D}{2} + \frac{\sqrt{D^2 + 4n_i^2(T)}}{2}, \quad p(T) = \frac{n_i^2(T)}{n(T)} \quad (4.17)$$

for n-type material and

$$p(T) = \frac{-D}{2} + \frac{\sqrt{D^2 + 4n_i^2(T)}}{2}, \quad n(T) = \frac{n_i^2(T)}{p(T)} \quad (4.18)$$

for p-type material.

4.2 High Temperature Results

In addition to testing the room temperature modelling ability of the simulation, I also desire to know the functionality of its high temperature modelling capabilities. At the time of this writing, high temperature data was only available for device A3. Consequently, the comparison of simulation and experimental results is limited to discussion of MOSFET A3.

For the high temperature simulations, all modelling parameters were initially kept at their room temperature values. The resulting $I - V$ curves for device A3 are given in Figures 4.1 through 4.4. The I_D versus V_{GS} data (Figures 4.1 and 4.2) are in good agreement for almost the entire range of V_{GS} value despite the fact that no high temperature optimization was done. This accomplishment validates the robustness and completeness of the models used to characterize the transport physics of the SiC MOSFETs. Specifically, the midband density of states and fixed oxide charge must be correct in order to match the $I - V$ curves in subthreshold. Additionally, the band edge interface trap values and mobility models must be

correct in order to match the knee and superthreshold portions of the $I_D - V_{GS}$ data. Most importantly, the agreement shows that the temperature dependence of the model is correct. Minor divergence from the experimental data at high V_{GS} values suggest that either the effective screening may be too low.

The increasingly worse agreement between the simulated and experimental drain current at higher temperatures (Figures 4.3 and 4.4) suggest that the empirical parameter v_{sat} may be a function of interface charge density much like the low field mobility term, μ_{Cit} . Usually, as the temperature increases, v_{sat} decreases due to the increased rate of optical phonon scattering. However, experimental data for these 6H-SiC MOSFETs shows an increase in current with temperature for both I_D versus V_{GS} and I_D versus V_{DS} . Examining the mobility models presented, all mobility components, with the exception of μ_{Cit} , decrease with increasing temperature, yet experimental data shows an increase in mobility as temperature increases. The only reasonable justification of this is that the reduction of interface trap occupation due to temperature increase has not only increased the net low field mobility component but also the high field. Increases in the low field mobility with temperature support my earlier claim that the interface charge scattering - and not the surface roughness - dominates the low field mobility of the MOSFETs used in this study.

Using the equations presented in chapter 2, the relationship between interface charge and low field mobility is apparent. However, the same can not be said about the relationship between interface charge and high field mobility. It an ef-

fort to achieve reasonable agreement between simulated and experimental results at high temperatures, I have chosen to increase the v_{sat} value. Simulation results with the new saturation velocity value are shown in Figures 4.5 through 4.7. The v_{sat} value has been raised to 2.1×10^5 cm/sec for 100 Celsius and 5.0×10^5 cm/sec for 200 Celsius. For I_D - V_{GS} data the change in v_{sat} causes no effect. However, the simulated I_D - V_{DS} data is in much better agreement with experiment. Expressing the effect on saturation velocity quantitatively is discussed in the Improving Surface Quality section of this chapter.

4.3 Improving Surface Quality

In this section I quantify potential device performance of 6H-SiC MOSFETs due to improved surface quality. These improvements include lowering the net surface charge density, $N_T = N_{it} + N_f$, via reduction in fixed oxide and trapped interface charge and smoothing the surface roughness of the MOSFET. I will present the results for both room and elevated temperatures.

Using the data gathered from the previous chapter, I have constructed a device that is representative of the other devices already tested. This new device is made from the same materials and has the same doping profile as devices mentioned in chapter 3. Also, like most of the devices previously studied, this device has a gate length of $4\mu m$ and an oxide thickness of 500\AA . However, I have chosen a gate width of $50\mu m$ for this device. Since the simulation model is based on a two dimensional system, the gate width value has no effect on the physics of the system and only

	device C1	device C1s	device C2
$D_{ito} (cm^{-2} eV^{-1})$	1.03×10^{12}	1.03×10^{12}	1.03×10^{11}
$D_c (cm^{-2} eV^{-1})$	1.143×10^{13}	1.143×10^{13}	1.143×10^{12}
$\xi_c (eV)$	0.1107	0.1107	0.1107
$N_f (cm^{-2})$	(+) 7.927×10^{11}	(+) 7.927×10^{11}	(+) 7.927×10^{10}
$n_{Cit} (cm^{-3})$	2.97×10^{17}	2.97×10^{17}	2.97×10^{17}
ζ_{Cit}	1	1	1
$v_{sat} (cm/sec)$	2.8×10^5	2.8×10^5	2.45×10^6
$\delta_{sr} (V/sec)$	1×10^{13}	1×10^{14}	1×10^{13}

Table 4.2: Model values for MOSFETs of set C. C1 is representative of devices previously studied in this work. C1s is identical to C1 with the exception that C1s has an improved surface roughness. C2 has a factor of 10 reduction in interface charge density and improved saturation velocity when compared to device C1.

	device C3	device C4	device C4s
$D_{ito} (cm^{-2} eV^{-1})$	1.03×10^{10}	1.03×10^9	1.03×10^9
$D_c (cm^{-2} eV^{-1})$	1.143×10^{11}	1.143×10^{10}	1.143×10^{10}
$\xi_c (eV)$	0.1107	0.1107	0.1107
$N_f (cm^{-2})$	(+) 7.927×10^9	(+) 7.927×10^8	(+) 7.927×10^8
$n_{Cit} (cm^{-3})$	2.97×10^{17}	2.97×10^{17}	2.97×10^{17}
ζ_{Cit}	1	1	1
$v_{sat} (cm/sec)$	1.166×10^7	1.867×10^7	1.867×10^7
$\delta_{sr} (V/sec)$	1×10^{13}	1×10^{13}	1×10^{14}

Table 4.3: Model values for MOSFETs of set C. C3 has a factor of 100 reduction in interface charge density and improved saturation velocity when compared to device C1. C4 has a factor of 1000 reduction in interface charge density and improved saturation velocity when compared to device C1. C4s is identical to C4 with the exception that C4s has an improved surface roughness.

scales the resulting drain-source current value. The model values for this device are equal to the average of the values from set A of the previous chapter, with the exception of the fixed oxide charge density. The fixed oxide charge density is computed by taking the average value of both sets A and B. This MOSFET is referred to as device C1, and its values are given in Table 4.2. In Tables 4.2 and 4.3 are the model values for other devices with improved surface quality. All of these devices will be discussed, and I shall begin with device C1.

Simulation results for drain current versus gate-source voltage and drain current versus drain-source voltage curves for MOSFET C1 at room temperature are shown in Figures 4.8 and 4.9. When multiplying the drain current values of C1 by the appropriate scaling factor (in this case 4), the performance of this device is comparable to devices from sets A and B of the previous chapter. High temperature simulations performed at 100 (see Figures 4.10 and 4.11) and 200 Celsius (Figures 4.12 and 4.13) also mimic the high temperature behavior of device A3. That is, as temperature increases, the current value for a specific voltage bias also increases. Described earlier, as the temperature elevates, the number of occupied interface trap states decreases. Therefore, if in fact interface charge scattering is the dominant scattering mechanism as I have already stated, I expect the effective mobility (and likewise the current) to also increase with temperature. Current versus voltage for temperatures are given in Figures 4.14 and 4.15. On both plots the drain current is higher at 100 and 200 Celsius than at room temperature for any given gate-source voltage. This behavior is consistent with the behavior of device A3. Figure 4.16 shows the charge carrying interface trap density, N_{it} , as a function of channel position for $V_{GS} = 6V$, $V_{DS} = 0.5V$. As the temperature increases, the occupied interface trap density decreases by 10 percent per 100 degrees Celsius. At this bias, the average electron channel mobilities are 18.8, 25.2, and 31.5 ($cm^2/V \text{ sec}$) for room temperature, 100, and 200 degrees Celsius, respectively. Such results support the assumption that interface charge scattering dominate surface mobility degradation.

The first step to an improved surface quality is lowering both fixed oxide and interface trap densities by a factor of 10 (device C2). I have performed I_D versus V_{GS} and I_D versus V_{DS} simulations. Results are given in Figures 4.17 and 4.18. I have also changed the value of the parameter v_{sat} . From high temperature experiment data of device A3, I deduced that the interface charge density not only affects the low field mobility but also the high field mobility. This was seen in the fact that there was an increase in saturation current as the temperature increased. In order to model this dependency of v_{sat} on the total interface charge density, N_T , I have included a term similar to that found in the interface charge component of the low field mobility model. This compensation term is given in Equation 4.19

$$v_{sat} = \frac{v_{max}}{1 + \alpha_v (N_{it} + N_f)} \quad (4.19)$$

where v_{max} is the maximum possible saturation velocity which I have assumed to be equal to the bulk saturation velocity of $2 \times 10^7 \text{ cm}^2/\text{V sec}$, N_{it} and N_f are the interface trap charge density and fixed oxide charge density, respectively, and α_v is a fitting parameter. Based on the high temperature data of device A3, α_v has an extracted value of $2.5 \times 10^{-11} \text{ cm}^2$ and results in a v_{sat} value of 2.45×10^6 for MOSFET C2. Equation 4.19 is used to calculate the theoretical saturation velocity limit of all devices in set C.

Simulated $I - V$ data for device C2 show impressive increases in current over its C1 companion. An astonishing 3 to 80 times improvement in certain parts of the $I_D - V_{DS}$ curve is achieved. However, there exist some undesirable behavior in the

$I_D - V_{GS}$ data. For gate-source voltages greater than $5V$, the channel mobility, and consequently the device current, begins to decrease. This behavior is also reflected in the $I_D - V_{DS}$ curve for low values of V_{DS} . A review of the low field mobility model of chapter 2 shows that all of the low field components are weak functions of the perpendicular electric field, with the exception of the surface roughness term, $\mu_{sr} = \frac{\delta_{sr}}{E_{\perp}^2}$. I will examine more closely the effects of surface roughness shortly using devices C1s and C4s.

For further improvements in device surface quality, consider MOSFETs C3 and C4. These FETs have a total interface charge density reduction factor of 100 and 1000, respectively. As with $I_D - V_{GS}$ curves of device C2, the drain current begins to decrease at the higher gate-source voltage values. (Figure 4.19.) Both C3 and C4 show a reduction of 20% from the peak drain current value to the value at V_{GS} equals $5V$. Shown in Figures 4.20 and 4.22, the impact of this current reduction can be seen in the $I_D - V_{DS}$ data where the current value for V_{GS} equals $5V$ is greater than the value for V_{GS} equals $7V$ for low V_{DS} . Similar results were presented by Momosa *et al.* using silicon, n-channel MOSFETs with 1.5 nanometer thick oxides and $0.09 \mu m$ gate lengths[51]. A comparison of the C3 and C4 $I - V$ curves show to that there is little improvement in the current yield between interface charge density reduction factors of 100 and 1000, so some other scattering mechanisms must be responsible for the lowering of current a high V_{GS} values. I propose that the other mechanism is service roughness.

Given the evidence presented thus far, one may wonder what the contri-

bution of the surface roughness is on the $I - V$ characterization of device C1. A comparison of simulation results for devices C1 and C1s (C1s is identical to device C1 with the exception of improved surface roughness) is given in Figures 4.23 and 4.24. Data from these $I - V$ plots show that surface roughness *could* have a noticeable but minimal effect on the characteristics of devices with interface trap densities similar to C1. On the other hand, if I improve the surface roughness of C4 by a factor of 10 (see device C4s in Table 4.3), room and elevated temperature simulations show that the current yield of the device improves drastically. (Figures 4.21 through 4.29). These figures reveal that, by first reducing the surface interface charge density then the surface roughness, 6H-SiC MOSFET performance can be improved and its behavior made to resemble that of high quality silicon MOSFETs. These improvements produce an increase of drain current, a reduction of surface roughness induced drain current lowering, the observance of high temperature performance degradation. Such results firmly establish the argument that, for the 6H-SiC MOSFETs studied, surface roughness degrade performance only after significant reduction in the surface interface charge density has been achieved. Consequently, I have deduced that the surface charge due to interface trap is largely responsible for the performance degradation observed in state-of-the-art 6H-SiC MOSFETs. So, as the interface charge density reduces, surface quality due to roughness becomes increasingly important. A comparison of the various surface qualities and its effect on drain current can be seen in Figure 4.30.

4.4 Scalability of SiC MOSFETs

Having shown potential device performance due to improvements in surface quality, it is time to investigate the scalability of the SiC MOSFETs. This inquiry is motivated by the fact that large scale integration (LSI) of silicon carbide MOSFETs could result in the achievement of integrated power and high temperature circuitry not possible with silicon. Experimental investigations of the scalability of n-channel enhancement mode 6H-SiC MOSFETs conducted by Lam and Kornegay [52] reveal that a segment of lightly-doped drain (LDD) region is necessary to reduce punchthrough effects for channel lengths less than $0.3\mu m$; however, the devices in [52] have a reported interface state density (\bar{D}_{it}) value of $1.1 \times 10^{11} \text{ cm}^{-2}$ and a fixed oxide charge density (N_f) of $(+)3.0 \times 10^{12} \text{ cm}^{-2}$. Such high interface concentrations may have an effect on the punchthrough behavior of MOSFETs. For the 1, 0.5, and 0.25 micron devices presented in this section, the interface charge density and surface roughness parameters are equal to those of device C4s (see Table 4.3). The oxide thickness of each MOSFET is 125, 63, and 32 Angstrom, respectively; the width of each device is $50\mu m$. Each of these devices uses a simple box geometry for the source and drain region - no LDD region is present. The initial doping profile for the $1\mu m$ 6H-SiC MOSFET is shown in Figure 4.31.

Let us examine the $I - V$ characteristics of each device in order to determine whether the limiting scalability factor is a function of device geometry or surface quality. $I - V$ curves for the $1\mu m$ are presented in Figures ?? and 4.33. Similar to the results of devices C2-C4, surface roughness dominates at high gate-source

voltages, even with the improved surface roughness parameter value of device C4s. The surface roughness dominant behavior continues and is magnified in the $I_D - V_{GS}$ characteristics of both the 0.5 (Figure 4.34) and 0.25 (Figure 4.35) micron devices.

The preceding results reveal that reduction of interface charge only is not enough to produce high quality, submicron 6H-SiC MOSFETs thus forcing further improvements to the surface roughness in order to observe the full current yielding potential of the scaled devices. As a result, I have improved the surface roughness of both the $0.5\mu m$ and $0.25\mu m$ devices by a factor of 5. Simulation results of the newly improved $0.5\mu m$ and $0.25\mu m$ FETs are given in Figures 4.36 and 4.37 and Figures 4.38 and 4.39, respectively. A comparison among the room temperature performance of the 1, 0.5, and $0.25\mu m$ devices is presented in Figures 4.40 and 4.41. Simulation data has shown that, by improving the surface quality of SiC MOSFETs, submicron technology without the use of complex doping profiles is achievable.

4.5 Chapter Summary

I have presented both room and high temperature data for 6H-SiC MOSFETs and have achieved agreement between experimental and simulated data at high temperatures. Succeeding in this task is a noteworthy accomplishment given numerical complexities associated with numerically solving the drift-diffusion heat flow equation set for wide bandgap materials such as silicon carbide. Using experimentally calibrated model values, I have shown that a factor of 100 improvement

in the reduction of net interface charge will greatly enhance performance of 6H-SiC MOSFETs; however, in order to produce the next generation of submicron SiC MOSFETs, improvements must also be achieved in the area of surface roughness smoothing.

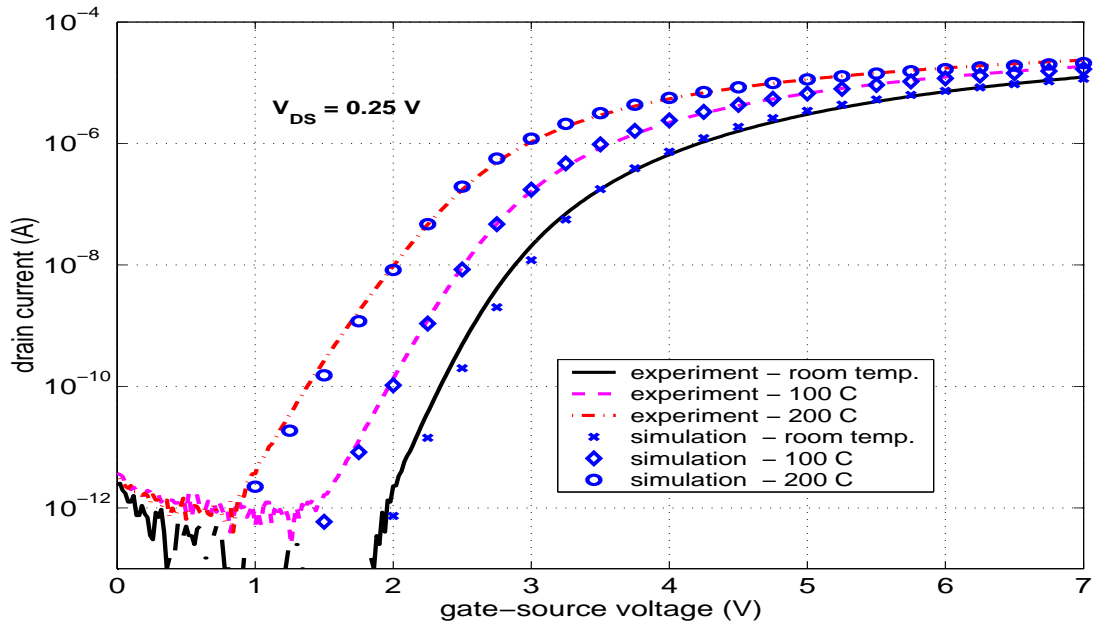


Figure 4.1: Drain current versus gate-source voltage the device A3 at room temperature, 100 Celsius, and 200 Celsius for a drain-source voltage equal to 0.25 Volts. Agreement between simulation and experiment is achieved without changing any of the room temperature model values.

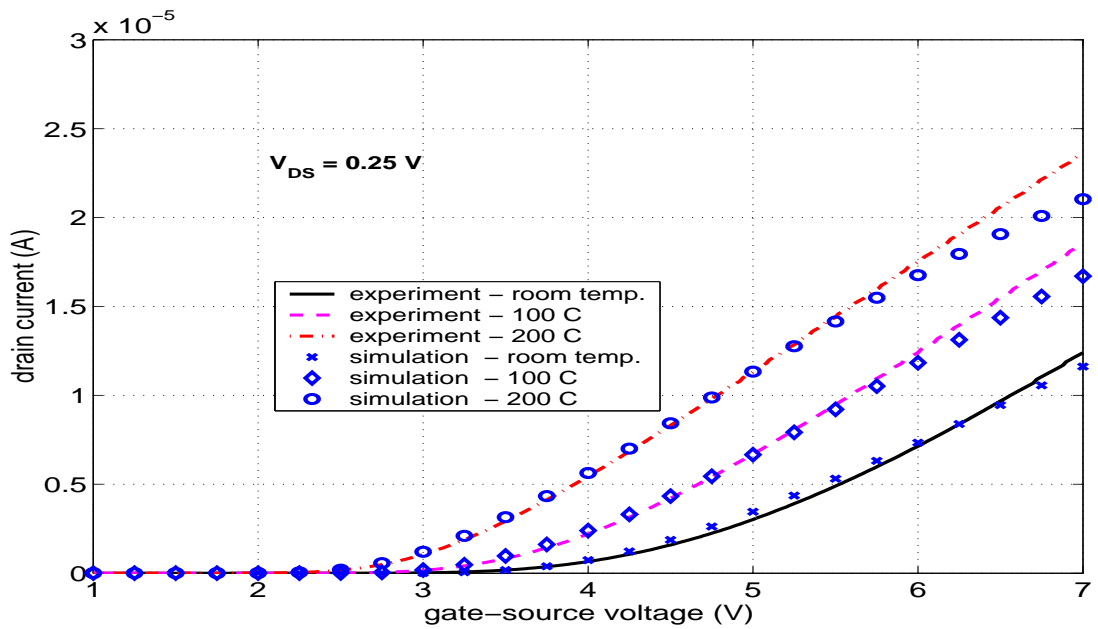


Figure 4.2: Linear scale of drain current versus gate-source voltage the device A3 at room temperature, 100 Celsius, and 200 Celsius for a drain-source voltage equal to 0.25 Volts. Agreement between simulation and experiment is achieved without changing any of the room temperature model values.

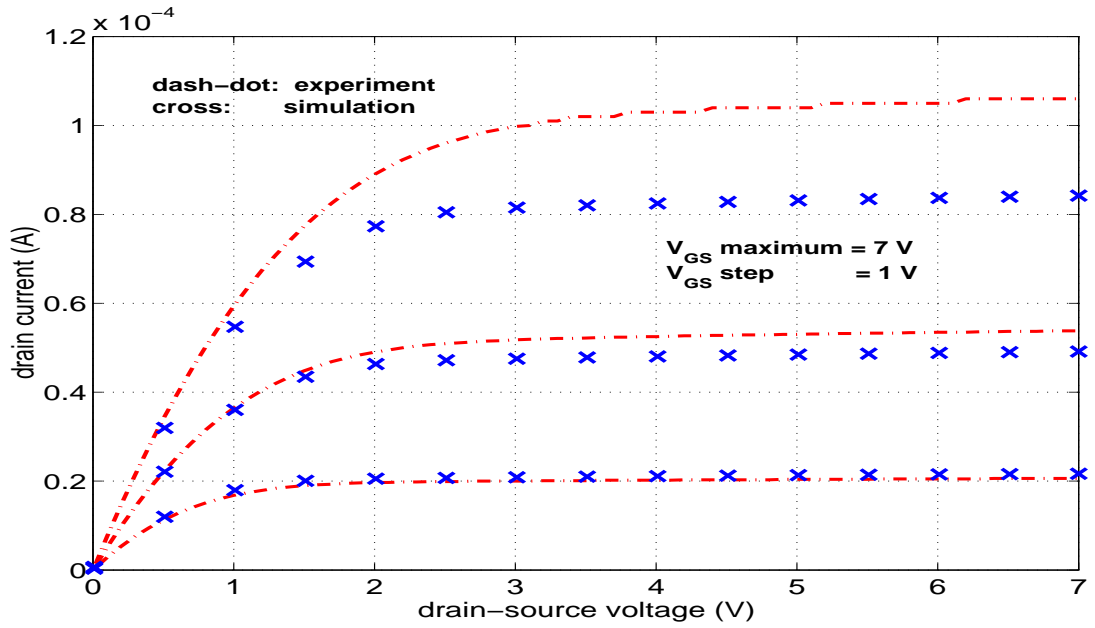


Figure 4.3: Drain current versus drain-source voltage for device A3 at 100 Celsius. Simulation results are in good agreement with experiment for gate-source voltages of 5 and 6 Volts. When the gate-source voltage is equal to 7 Volts, the simulation underestimates the drain current by 20 percent.

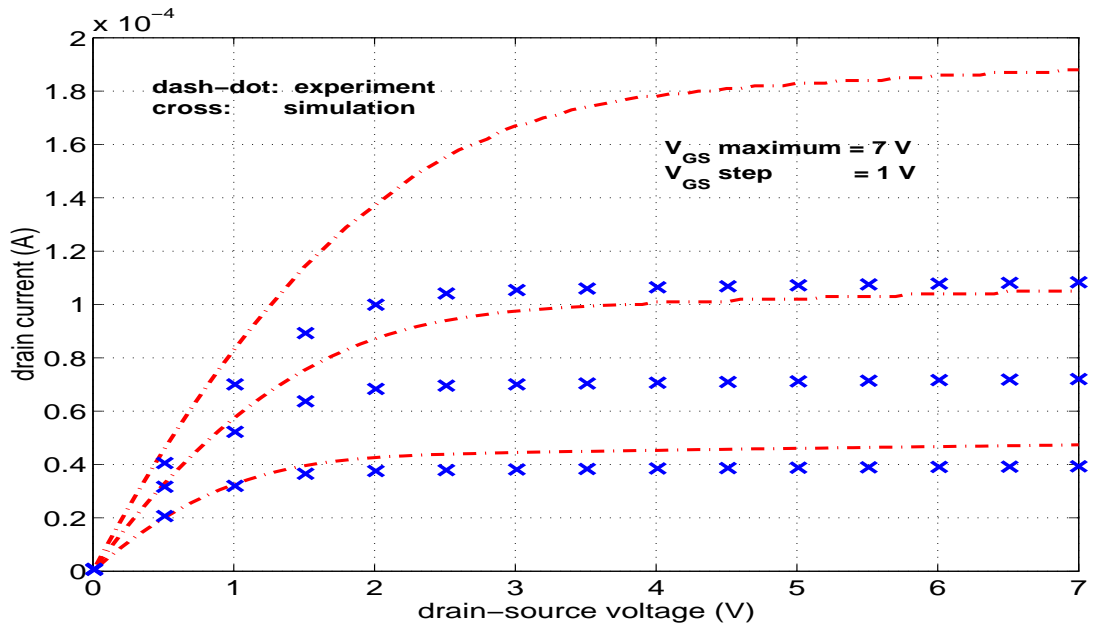


Figure 4.4: Drain current versus drain-source voltage for device A3 at 200 Celsius. Simulation results are in reasonable agreement with experiment for gate-source voltage of 5 Volts. When the gate-source voltage is equal to 6 and 7 Volts, the simulation underestimates the drain current by 25 and 45 percent, respectively.

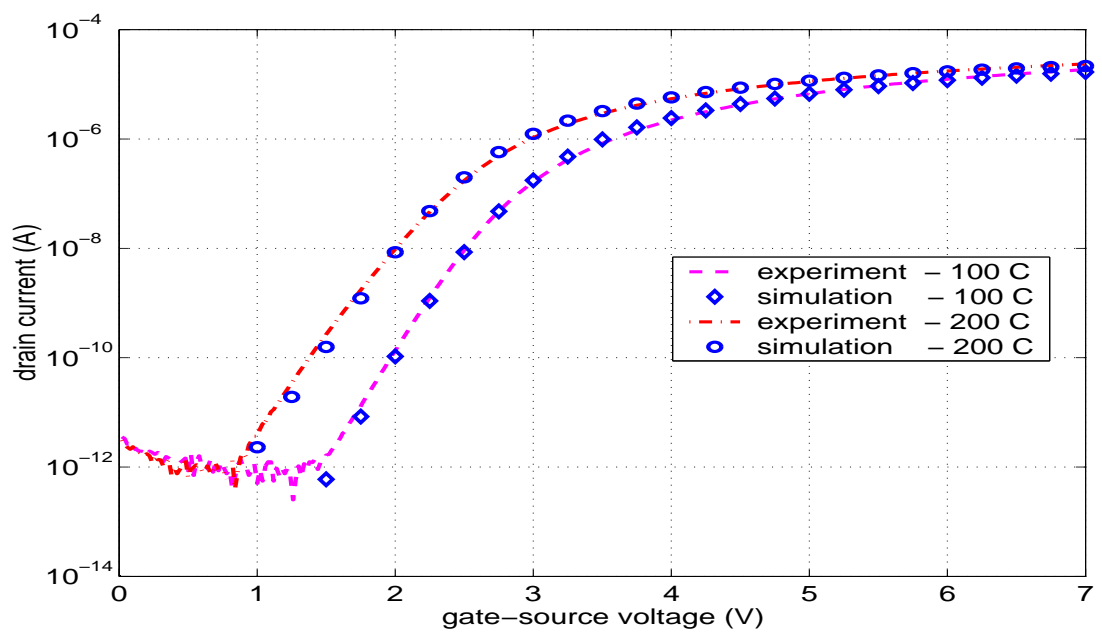


Figure 4.5: Drain current versus gate-source voltage for device A3 at 100 and 200 Celsius with improved saturation velocity value.

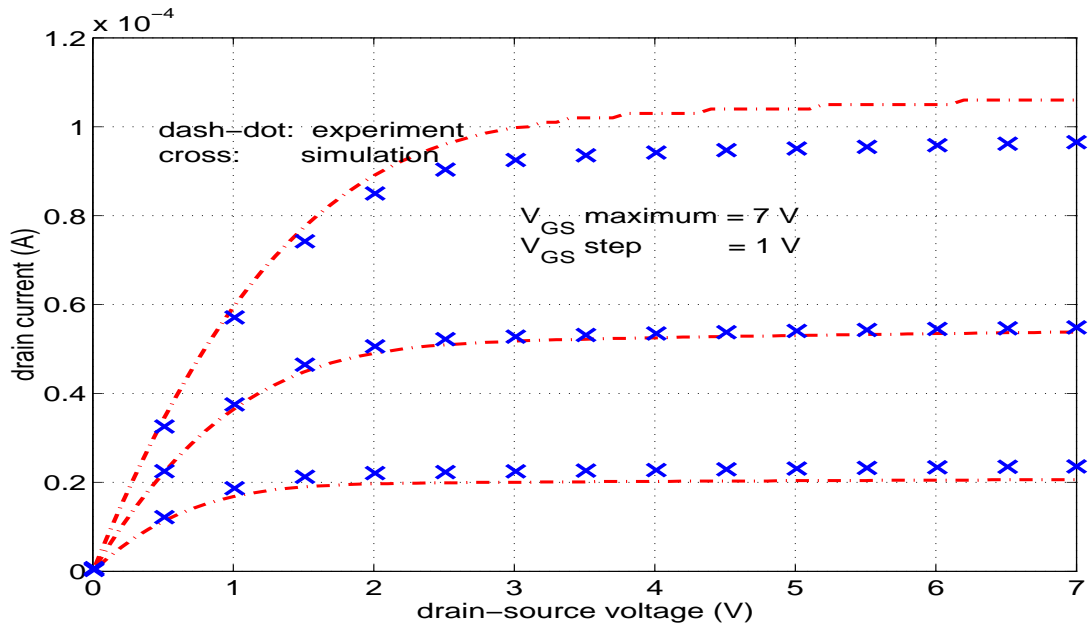


Figure 4.6: Drain current versus drain-source voltage for device A3 at 100 Celsius with a corrected saturation velocity value of 2.1×10^5 cm/sec. Simulation and experiment are in reasonable agreement for all gate-source voltages shown.

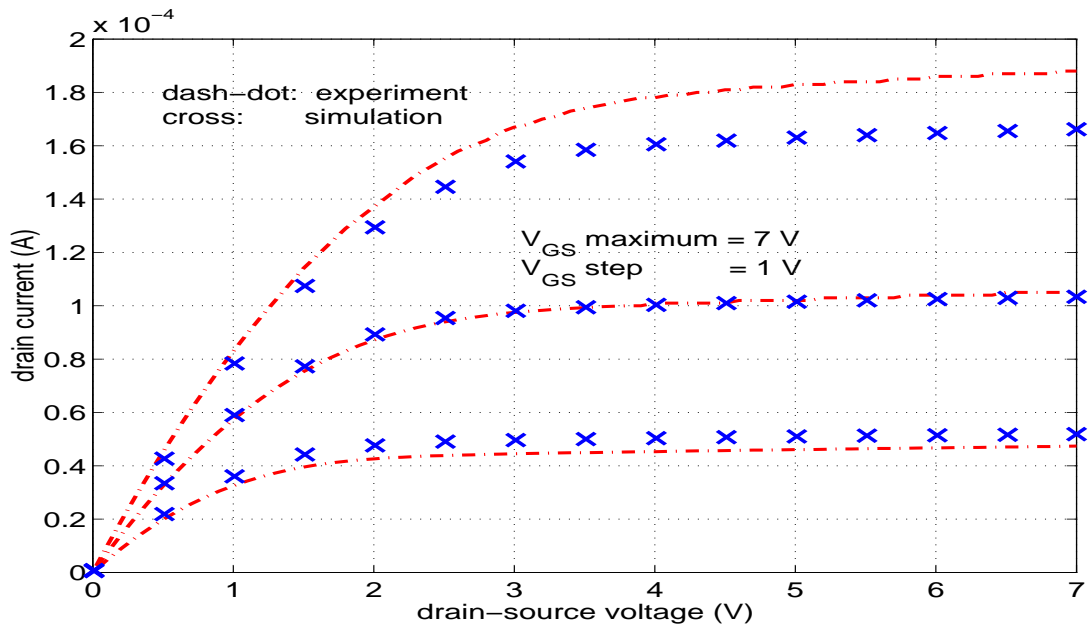


Figure 4.7: Drain current versus drain-source voltage for device A3 at 200 Celsius with a corrected saturation velocity value of 5.0×10^5 cm/sec. Simulation and experiment are in reasonable agreement for all gate-source voltages shown.

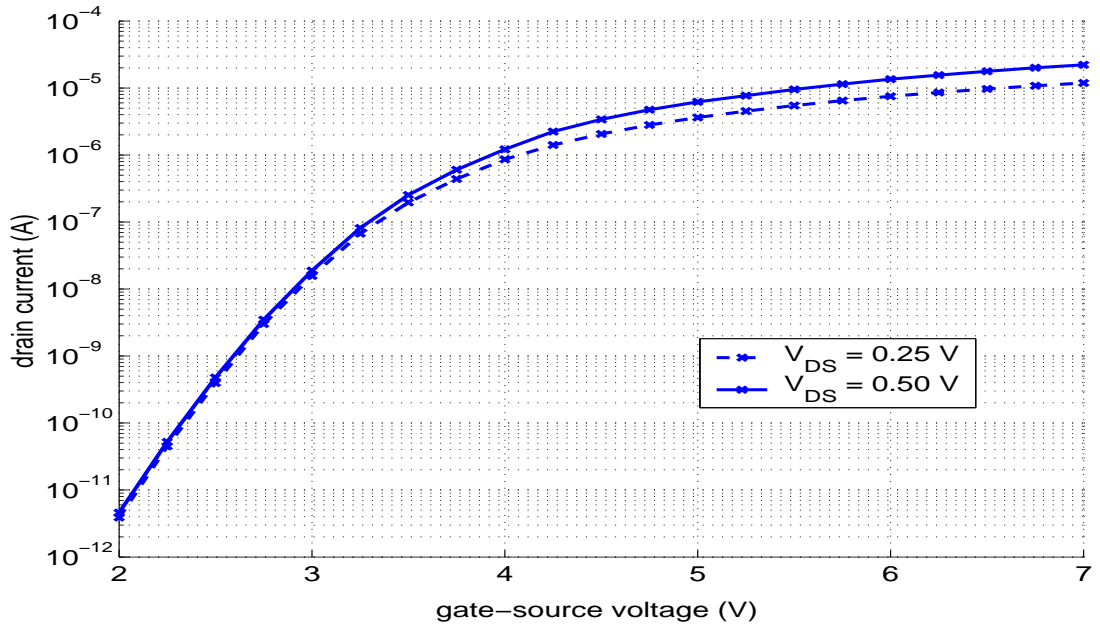


Figure 4.8: Drain current versus gate-source voltage of device C1 at room temperature for a drain-source voltage of 0.25 and 0.5 Volts. C1 is representative of the sets A and B 6H-SiC MOSFETs.

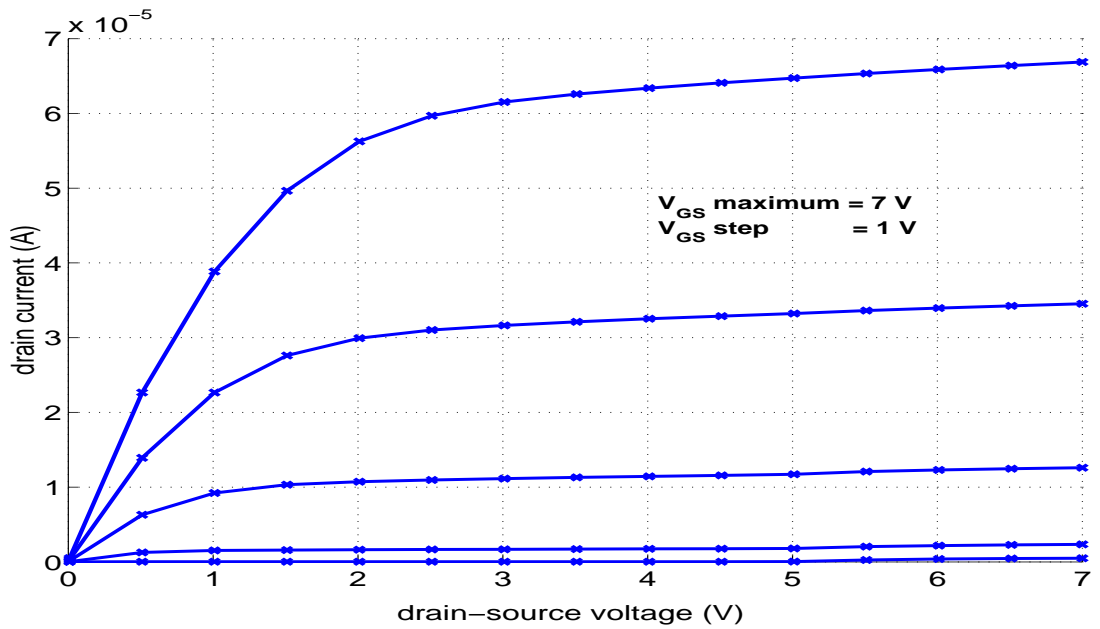


Figure 4.9: Drain current versus drain-source voltage of device C1 at room temperature. C1 is representative of the sets A and B 6H-SiC MOSFETs.

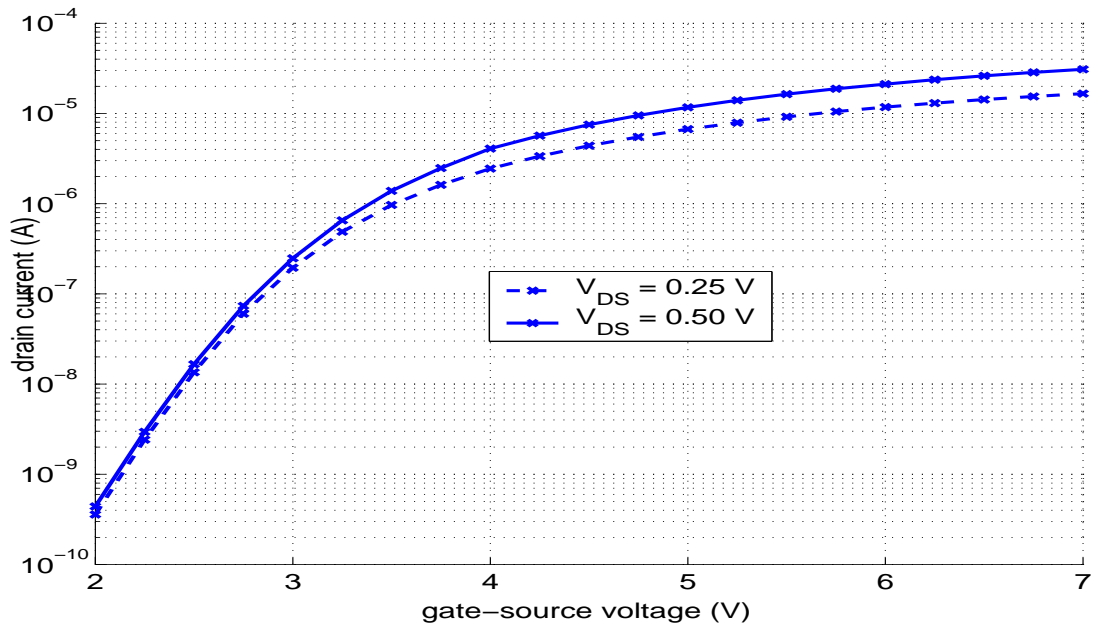


Figure 4.10: Drain current versus gate-source voltage of device C1 at 100 Celsius for a drain-source voltage of 0.25 and 0.5 Volts. C1 is representative of the sets A and B 6H-SiC MOSFETs.

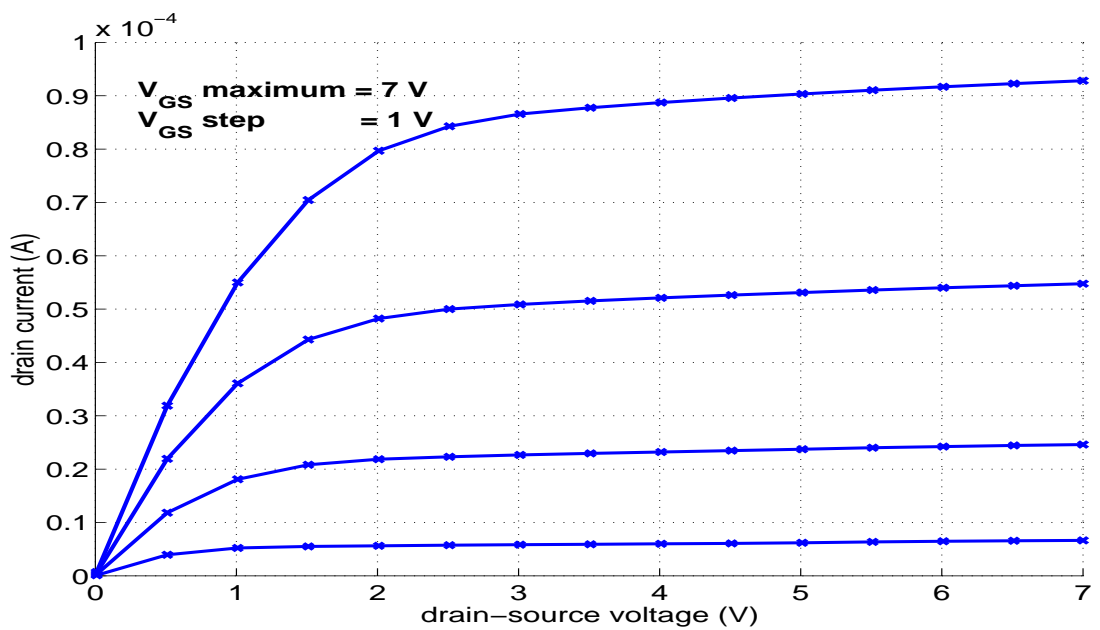


Figure 4.11: Drain current versus drain-source voltage of device C1 at 100 Celsius. C1 is representative of the sets A and B 6H-SiC MOSFETs.

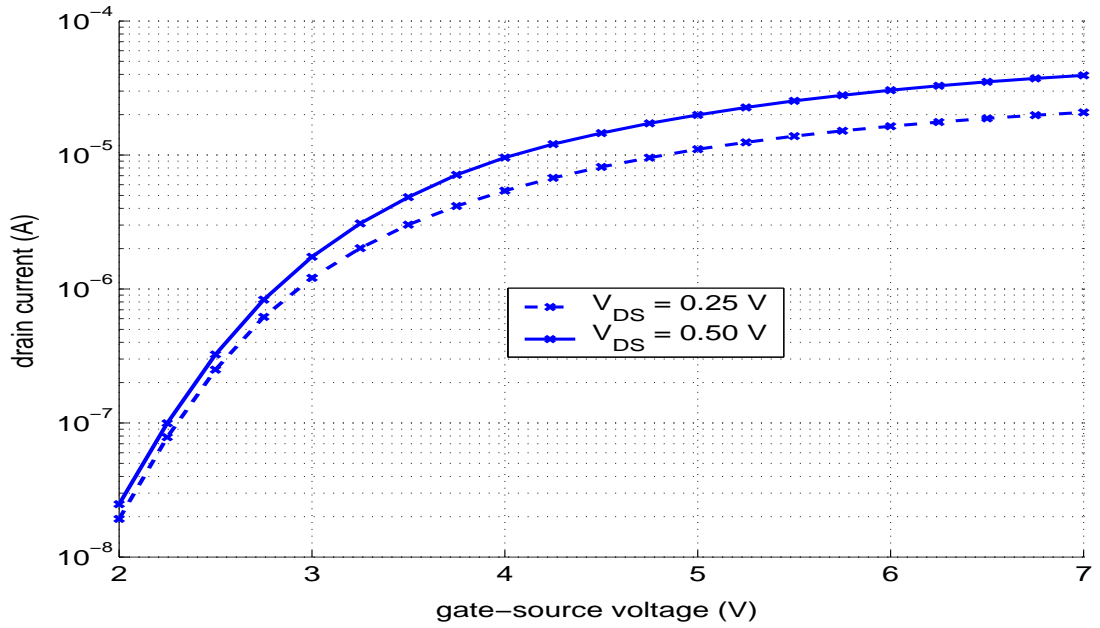


Figure 4.12: Drain current versus gate-source voltage of device C1 at 200 Celsius for a drain-source voltage of 0.25 and 0.5 Volts. C1 is representative of the sets A and B 6H-SiC MOSFETs.

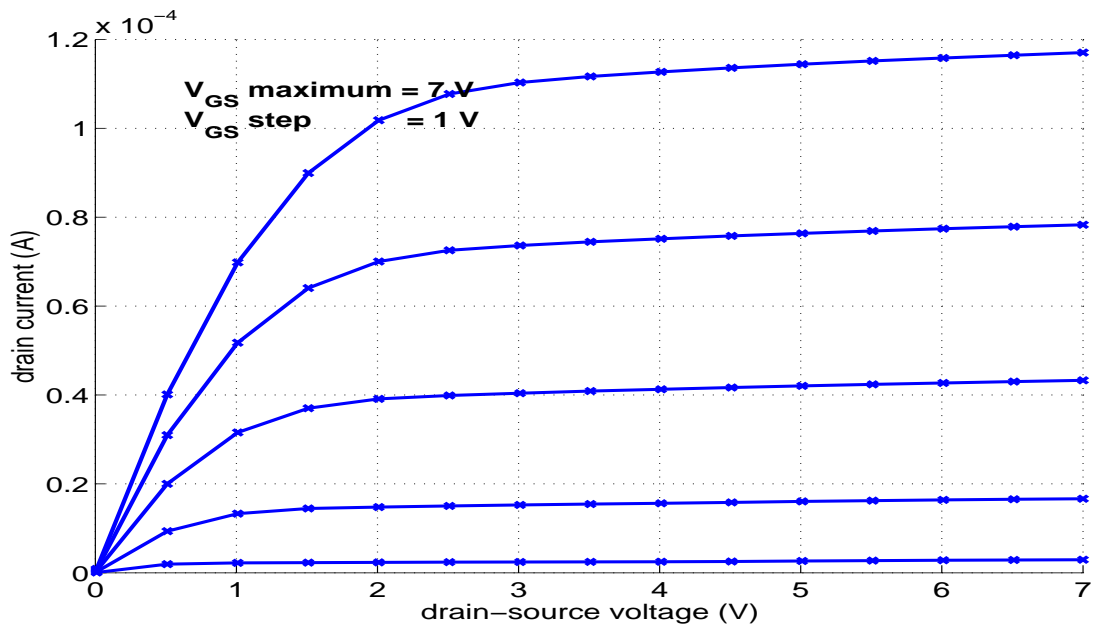


Figure 4.13: Drain current versus drain-source voltage of device C1 at 200 Celsius. C1 is representative of the sets A and B 6H-SiC MOSFETs.

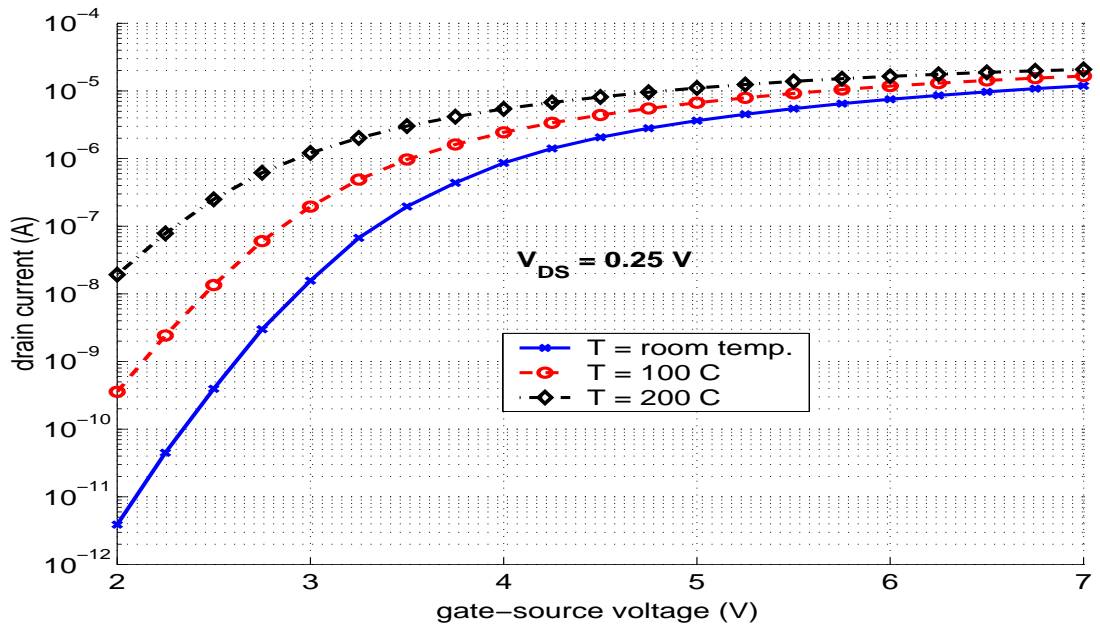


Figure 4.14: Drain current versus gate-source voltage of device C1 at various temperatures for a drain-source voltage of 0.25 and 0.5 Volts. C1 is representative of the sets A and B 6H-SiC MOSFETs.

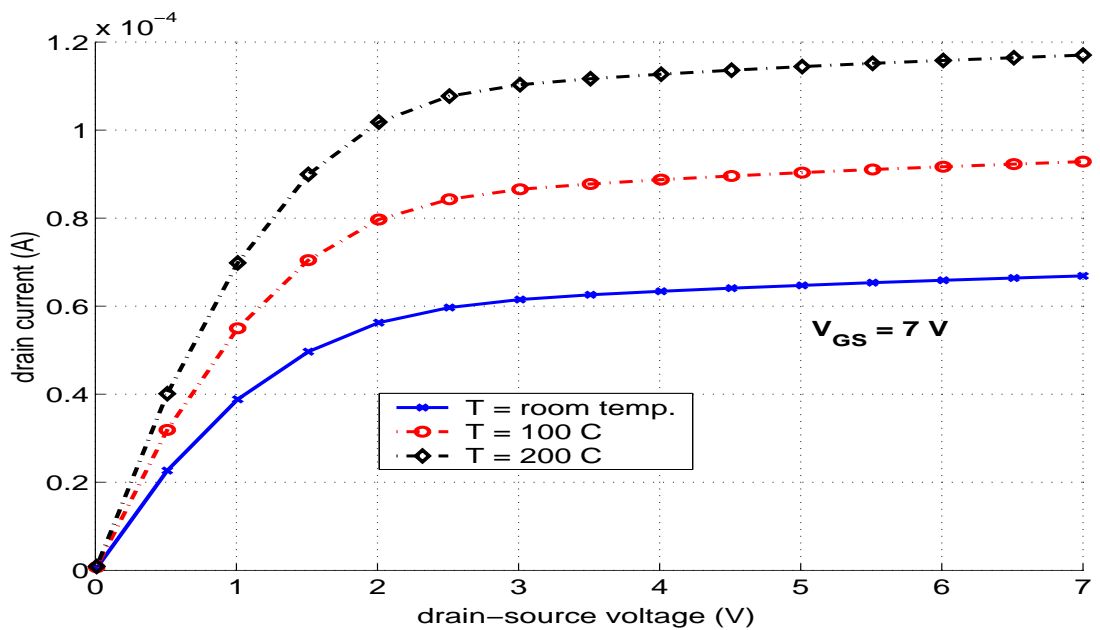


Figure 4.15: Drain current versus drain-source voltage of device C1 at various temperatures. C1 is representative of the sets A and B 6H-SiC MOSFETs.

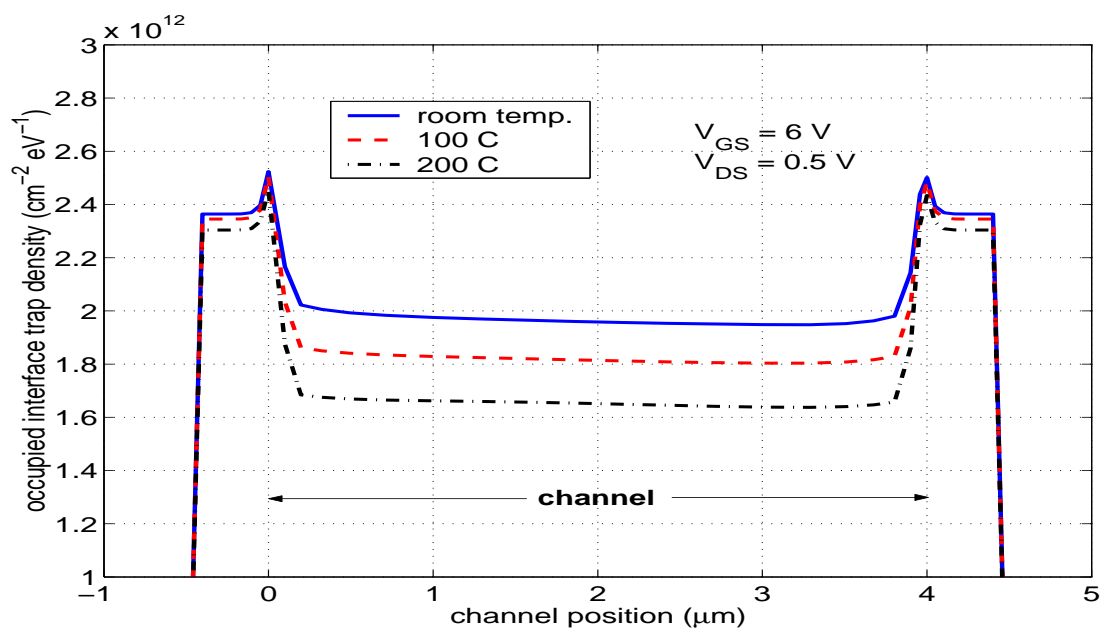


Figure 4.16: Occupied interface trap density of device C1 at $V_{GS} = 6V$, $V_{DS} = 0.5V$ for various temperatures. The trap density is decreasing at a rate of 10 percent per 100 degrees.

This page intentionally left blank.

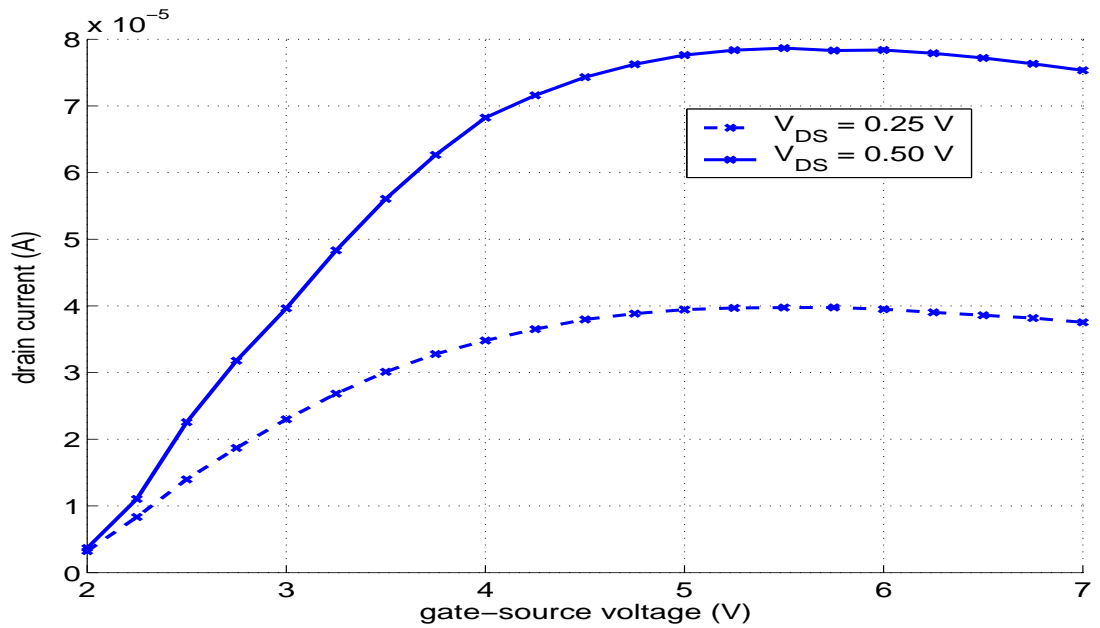


Figure 4.17: Drain current versus gate-source voltage of device C2 at room temperature. The interface charge density of device C2 is reduced by a factor of 10 when compared to C1. Though the drain current is considerably higher when compared to C1, notice the decrease in drain current after the gate-source value of 5 Volts.

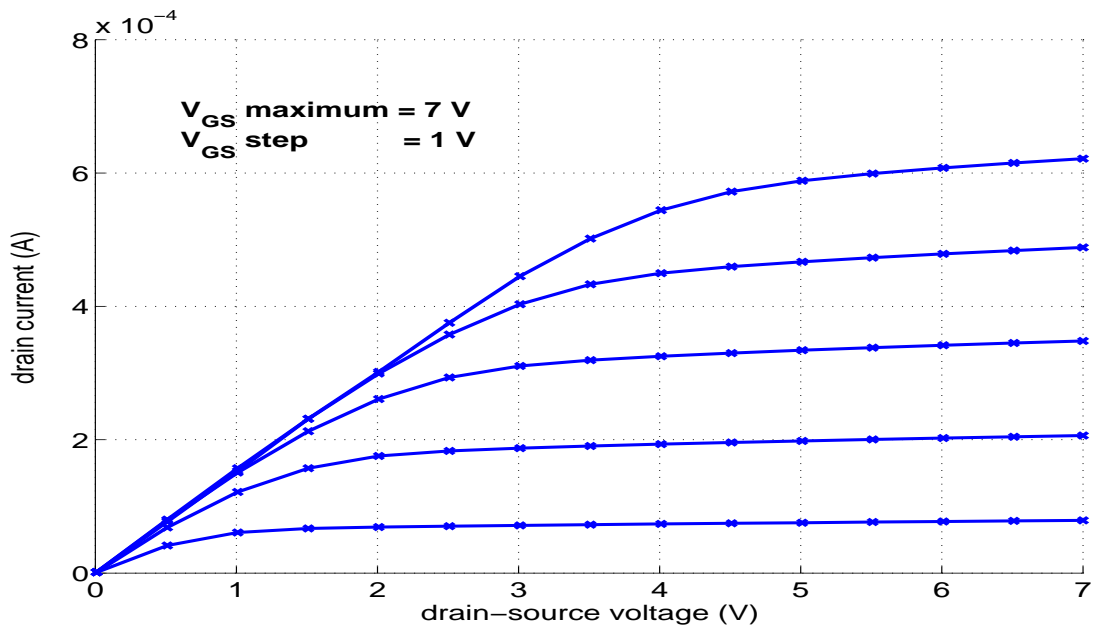


Figure 4.18: Drain current versus drain-source voltage of device C2 at room temperature. The interface charge density of device C2 is reduced by a factor of 10 when compared to C1. Drain current is considerably higher when compared to C1.

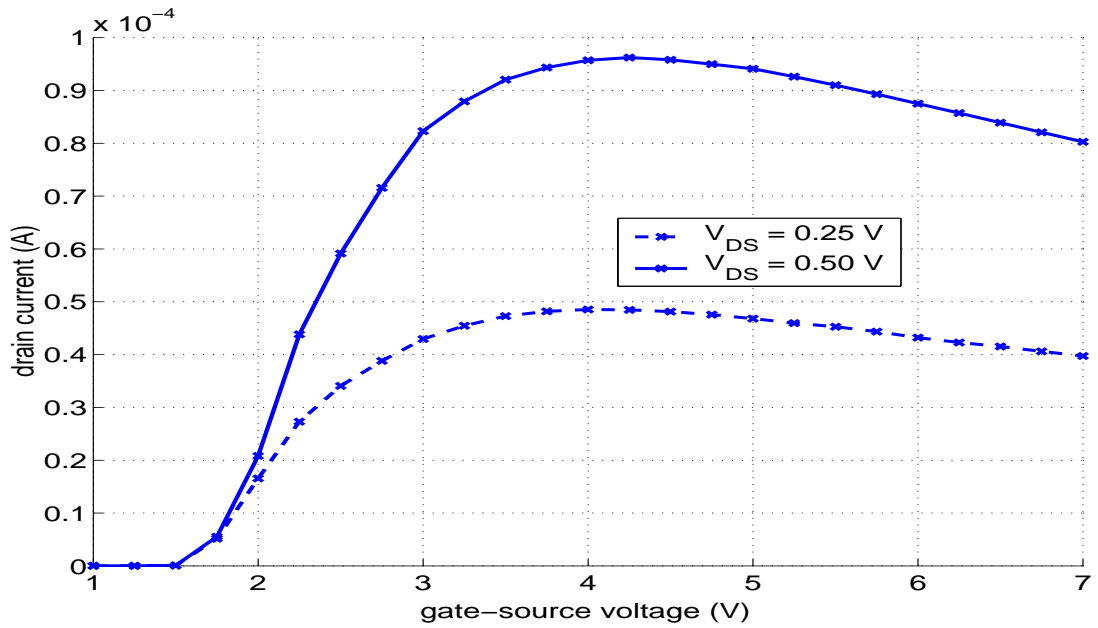


Figure 4.19: Drain current versus gate-source voltage of device C3 at room temperature. The interface charge density of device C3 is reduced by a factor of 100 when compared to C1. Though the drain current is considerably higher when compared to C1, notice the decrease in drain current after the gate-source value of 4 Volts.

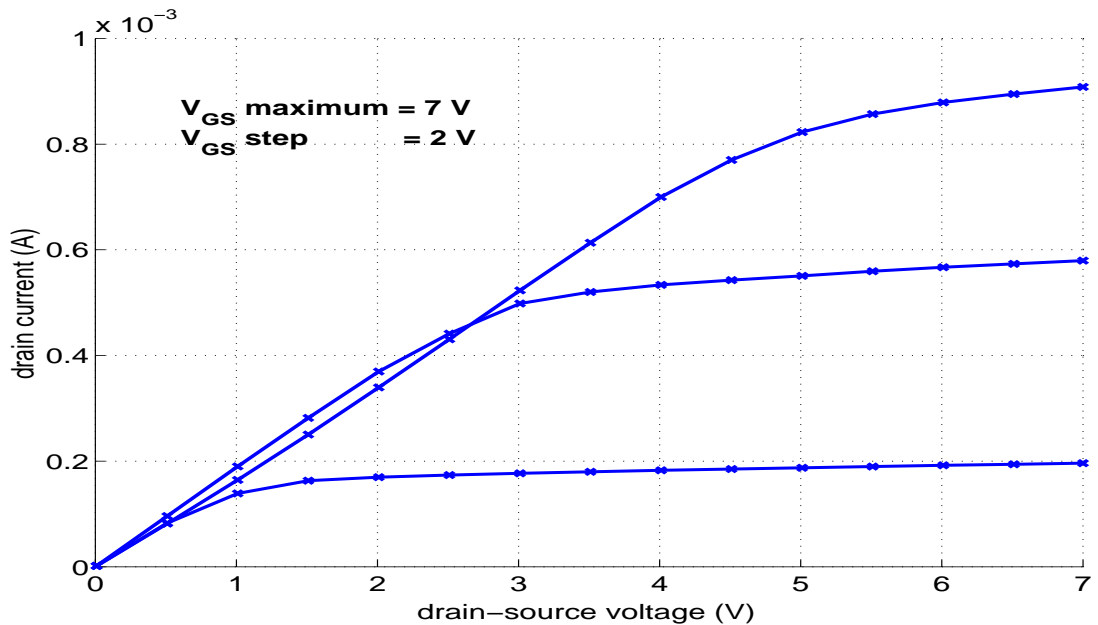


Figure 4.20: Drain current versus drain-source voltage of device C3 at room temperature. The interface charge density of device C3 is reduced by a factor of 100 when compared to C1. Drain current is considerably higher when compared to C1. Notice the overlap of drain current values at V_{GS} equal to 5 Volts and V_{GS} equal to 7 Volts for low drain-source voltage values.

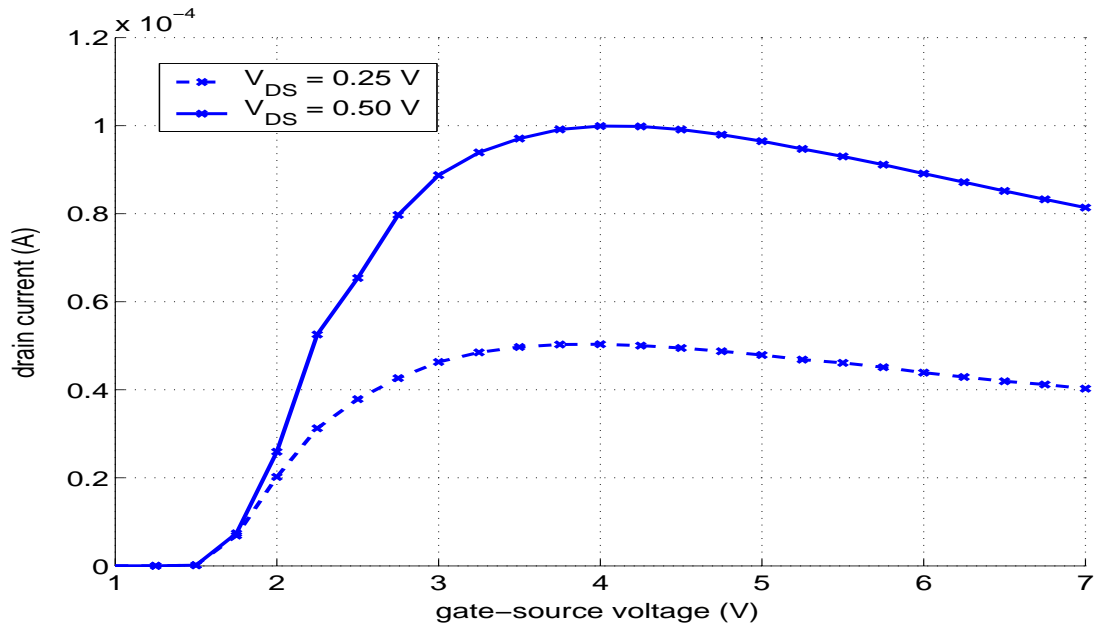


Figure 4.21: Drain current versus gate-source voltage of device C4 at room temperature. The interface charge density of device C4 is reduced by a factor of 1000 when compared to C1. Though the drain current is considerably higher when compared to C1, notice the decrease in drain current after the gate-source value of 4 Volts.

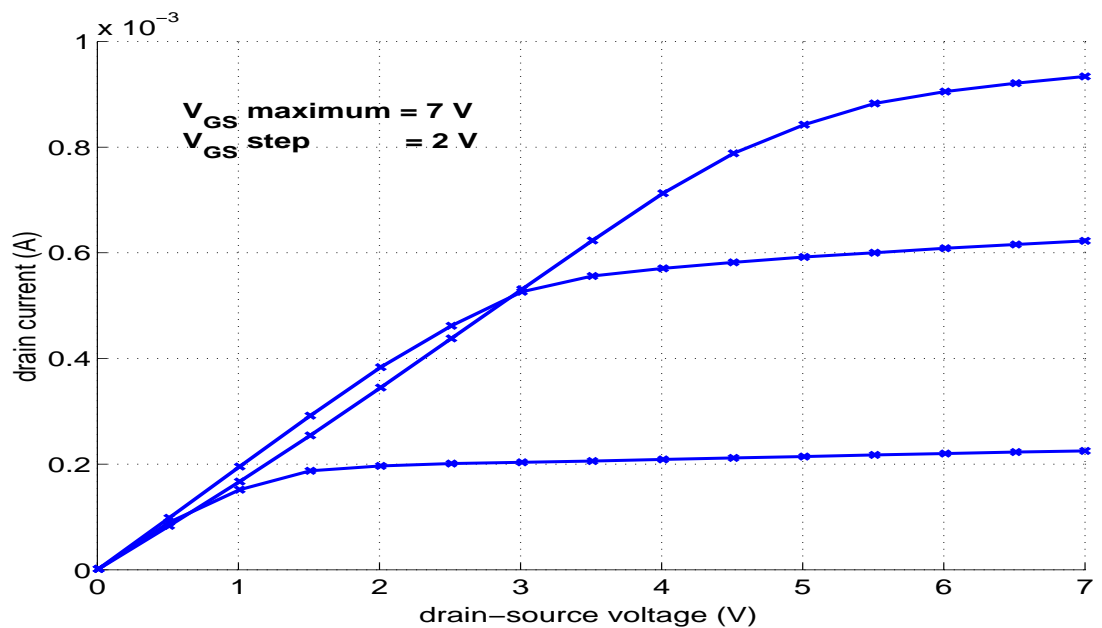


Figure 4.22: Drain current versus drain-source voltage of device C4 at room temperature. The interface charge density of device C4 is reduced by a factor of 1000 when compared to C1. Drain current is considerably higher when compared to C1. Notice the overlap of drain current values at V_{GS} equal to 5 Volts and V_{GS} equal to 7 Volts for low drain-source voltage values.

This page intentionally left blank.

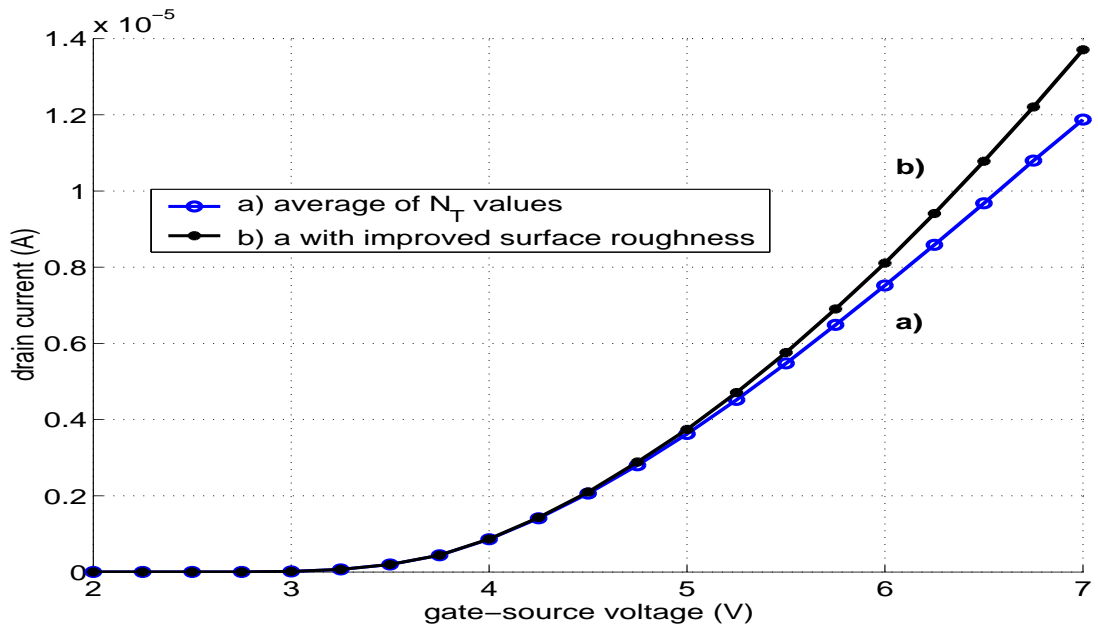


Figure 4.23: Drain current versus gate-source voltage of device C1s at room temperature. The surface roughness of device C1s is reduced by a factor of 10 when compared to C1. Notice that a tenfold improvement in surface roughness makes only a small improvement to the drain current.

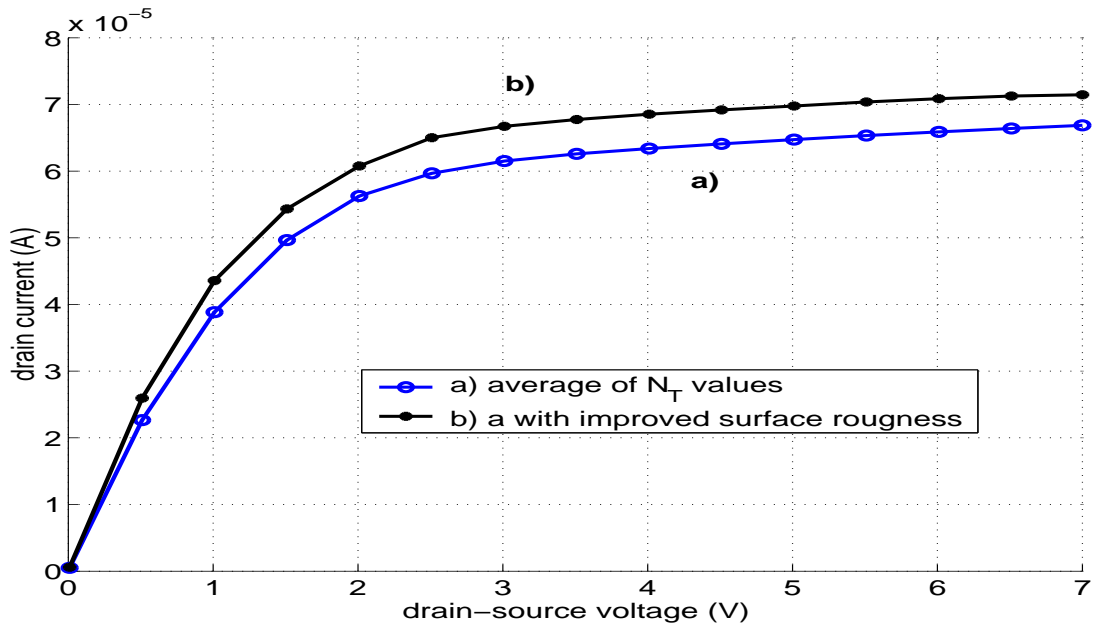


Figure 4.24: Drain current versus drain-source voltage of device C1s at room temperature for V_{GS} equal to 6 Volts. The surface roughness of device C1s is reduced by a factor of 10 when compared to C1. Notice that a tenfold improvement in surface roughness makes only a small improvement to the drain current.

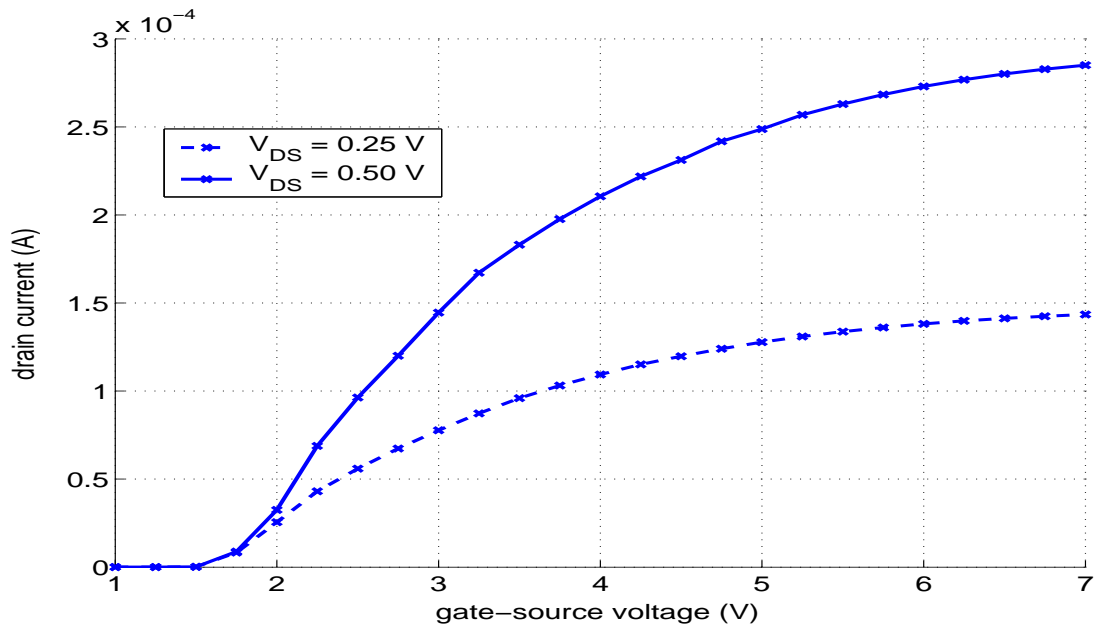


Figure 4.25: Drain current versus gate-source voltage of device C4s at room temperature. The surface roughness of device C4s is reduced by a factor of 10 when compared to C4. Notice that the drain current continues to increase as a gate-source voltage increase when the surface roughness is improved.

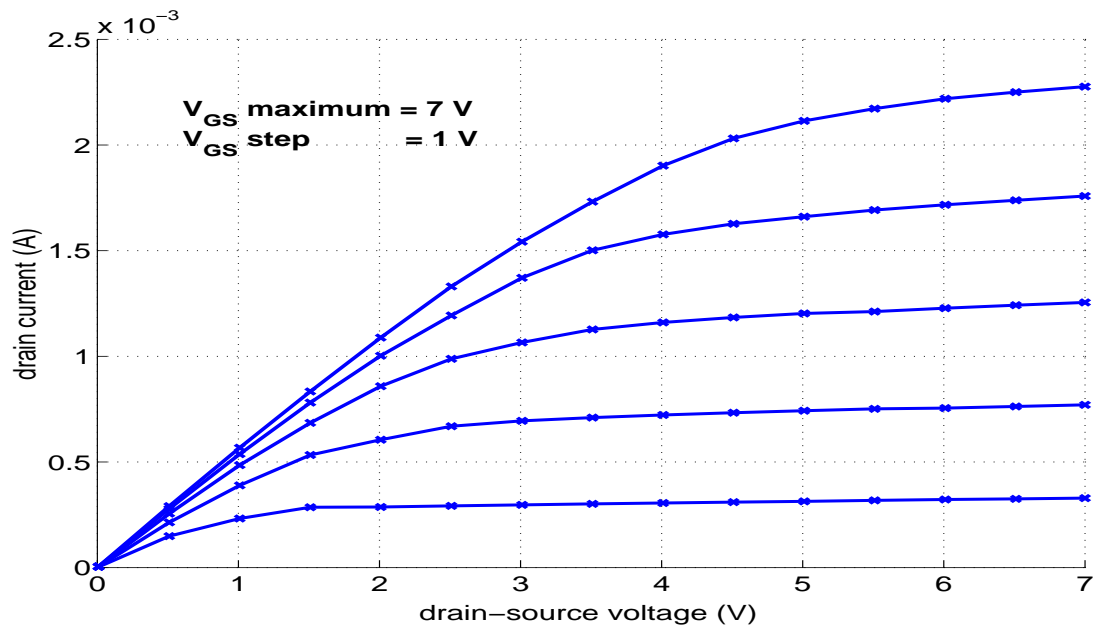


Figure 4.26: Drain current versus drain-source voltage of device C4s at room temperature. The surface roughness of device C4s is reduced by a factor of 10 when compared to C4. Notice that there is not overlap of drain current values.

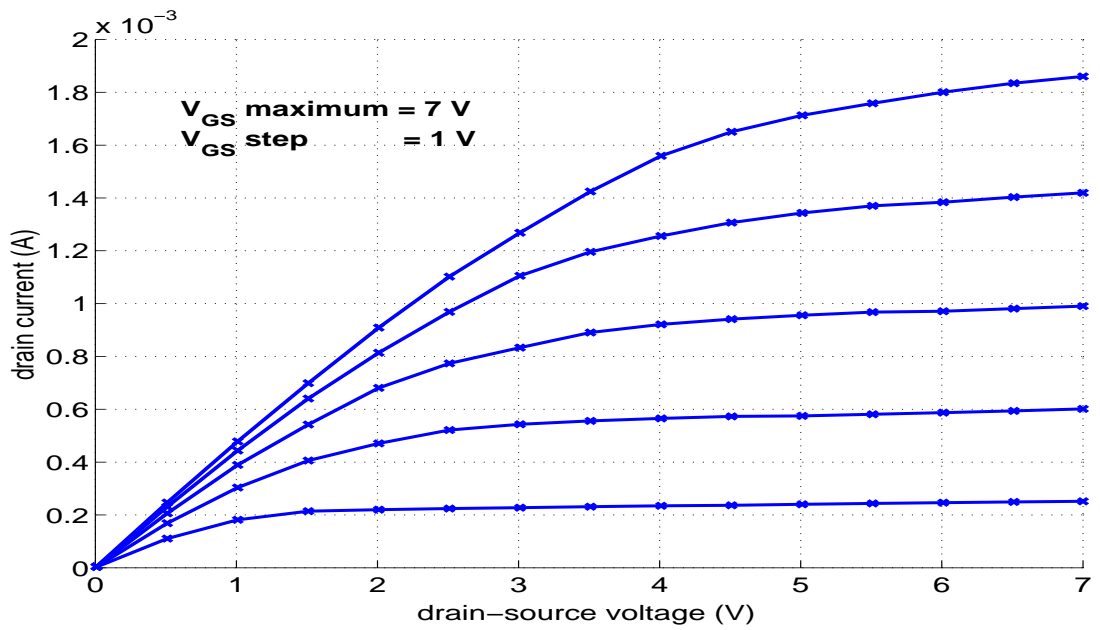


Figure 4.27: Drain current versus drain-source voltage of device C4s at 100 Celsius. The surface roughness of device C4s is reduced by a factor of 10 when compared to C4. Notice that the drain current decreases as a function of temperature.

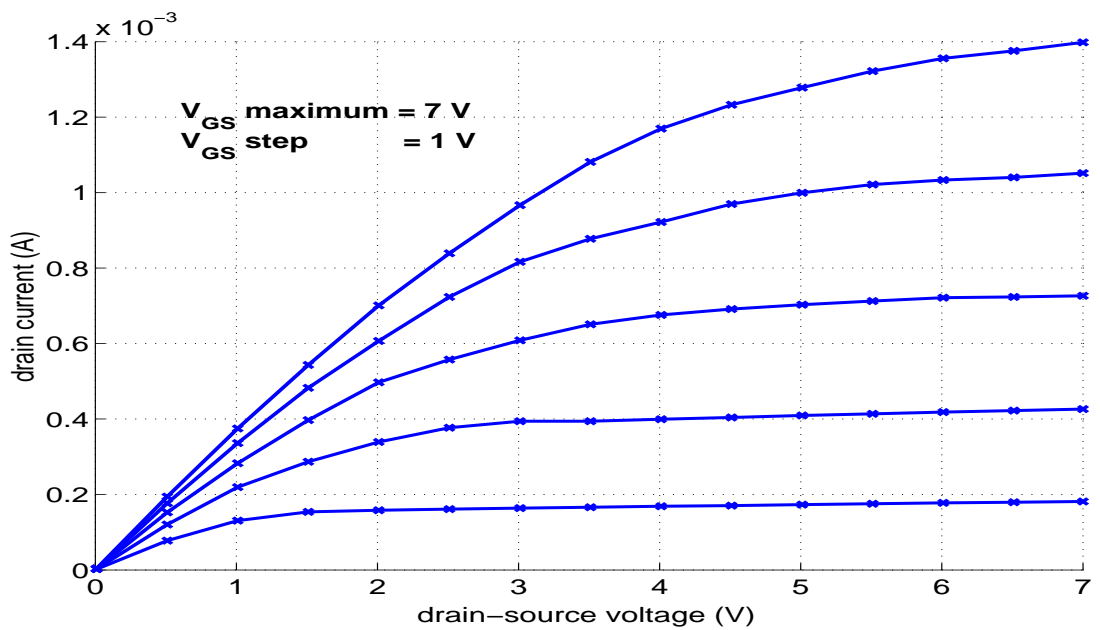


Figure 4.28: Drain current versus drain-source voltage of device C4s at 200 Celsius. The surface roughness of device C4s is reduced by a factor of 10 when compared to C4. Notice that the drain current decreases as a function of temperature.

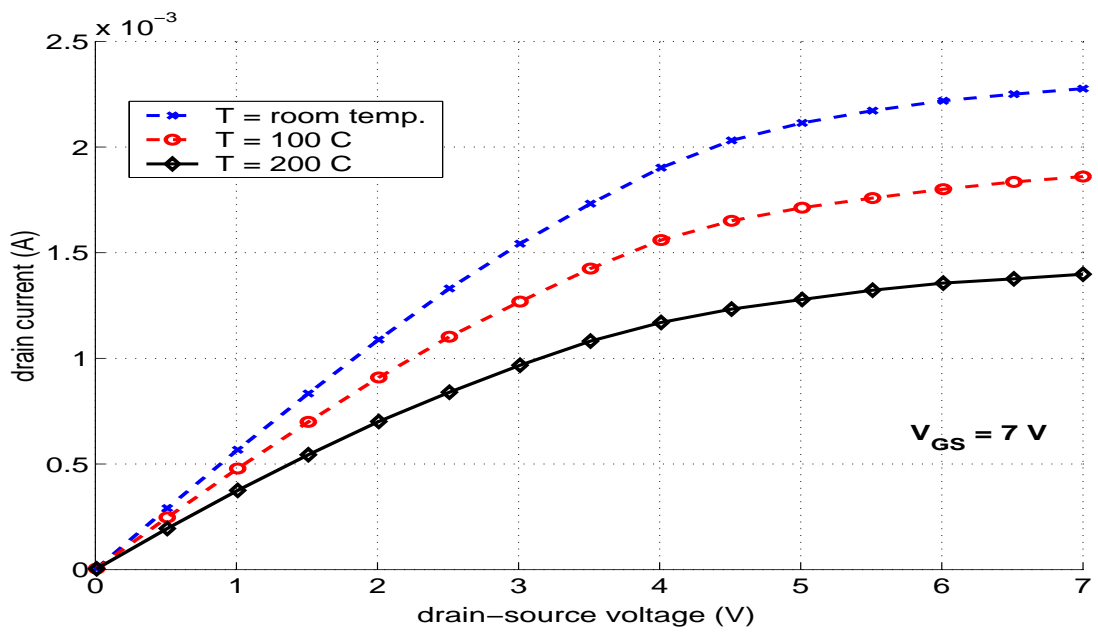


Figure 4.29: Drain current versus drain-source voltage of device C4s at various temperatures. The surface roughness of device C4s is reduced by a factor of 10 when compared to C4. Notice that the drain current decreases as a function of temperature.

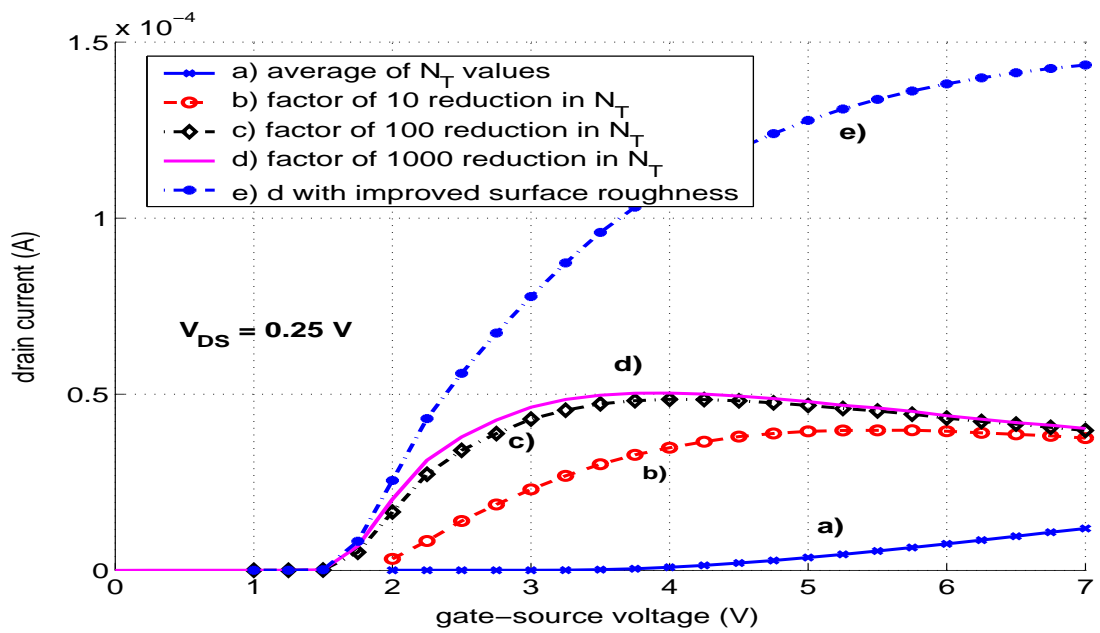


Figure 4.30: Drain current versus gate-source voltage of set C devices at room temperature. Drain current values increase drastically as the interface charge density is decreased by a factor of 100. There is little improvement in drain current once interface charge density values are reduced further than one hundredfold. After this point reduce in surface roughness increases drain current values.

This page intentionally left blank.

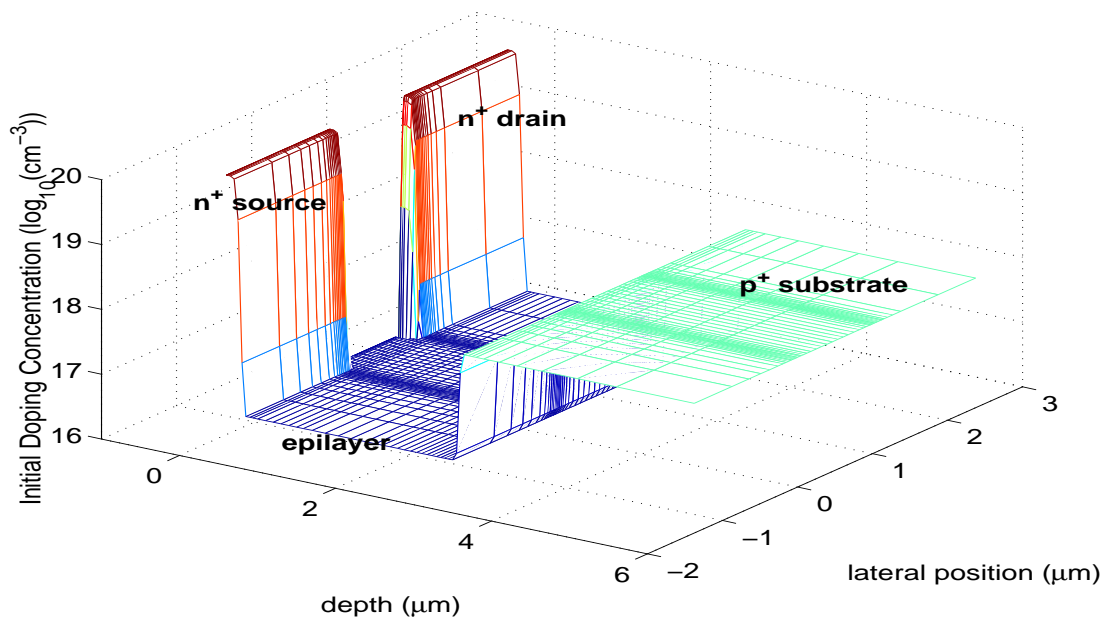


Figure 4.31: Initial Doping Profile for $50\mu\text{m}$ by $1\mu\text{m}$ device

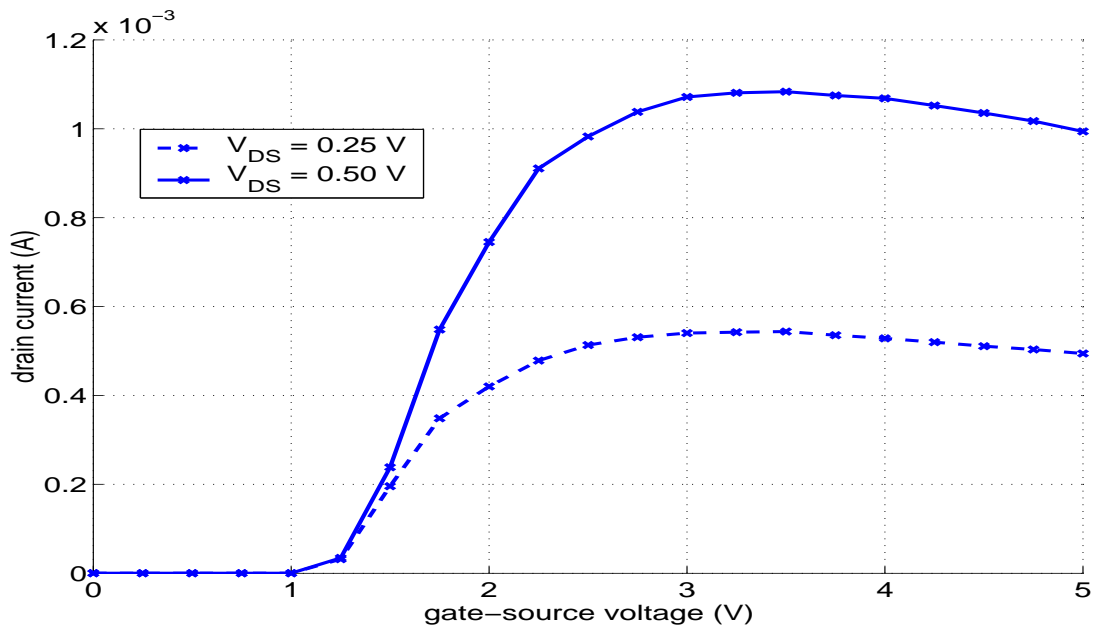


Figure 4.32: Drain current versus gate-source voltage of $1\mu m$ device at room temperature. Notice the decrease in drain current value due to surface roughness after a gate-source voltage of 3 Volts.

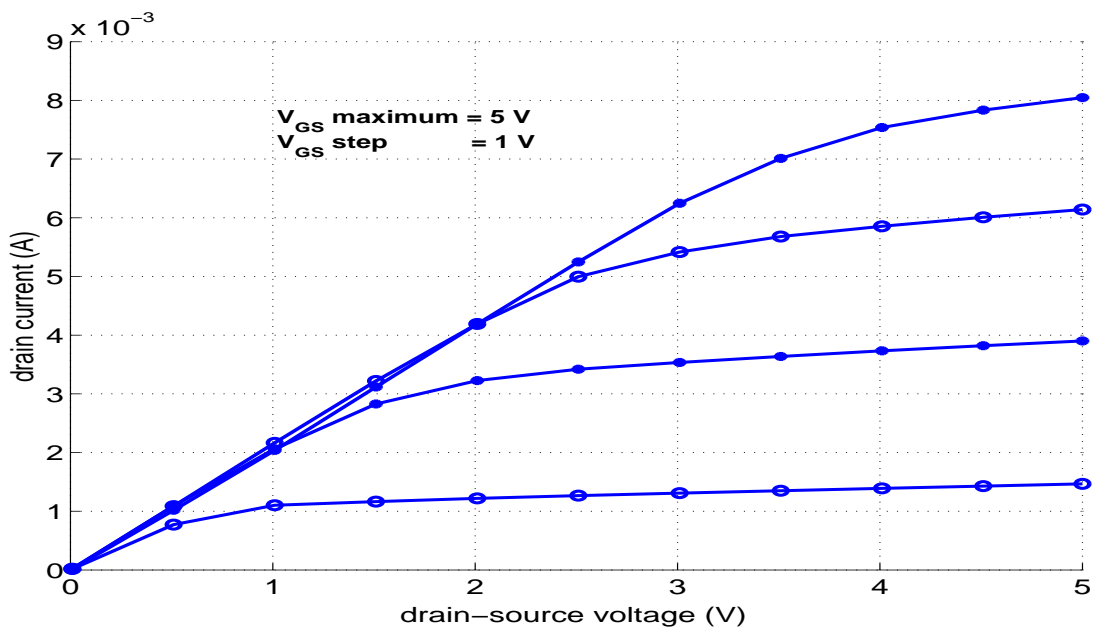


Figure 4.33: Drain current versus drain-source voltage of $1\mu m$ device at room temperature. Notice the slight overlap a drain current values between V_{GS} equal to 4 Volts and V_{GS} equal to 5 Volts due to surface roughness.

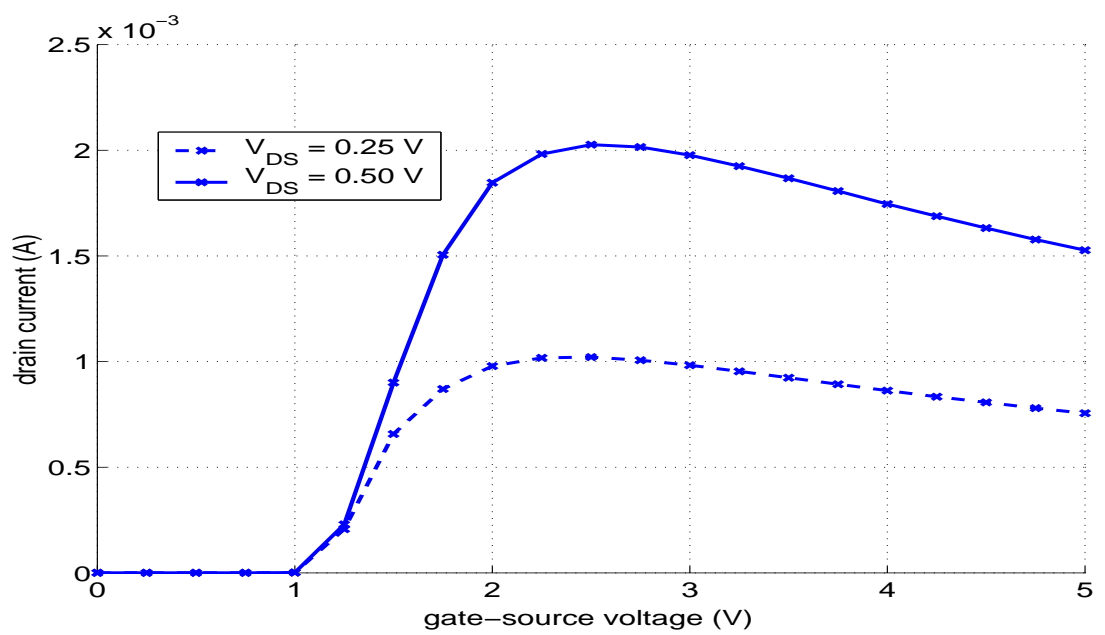


Figure 4.34: Drain current versus gate-source voltage of $0.5\mu m$ device at room temperature. Notice the decrease in drain current value due to surface roughness after a gate-source voltage of 2.5 Volts.

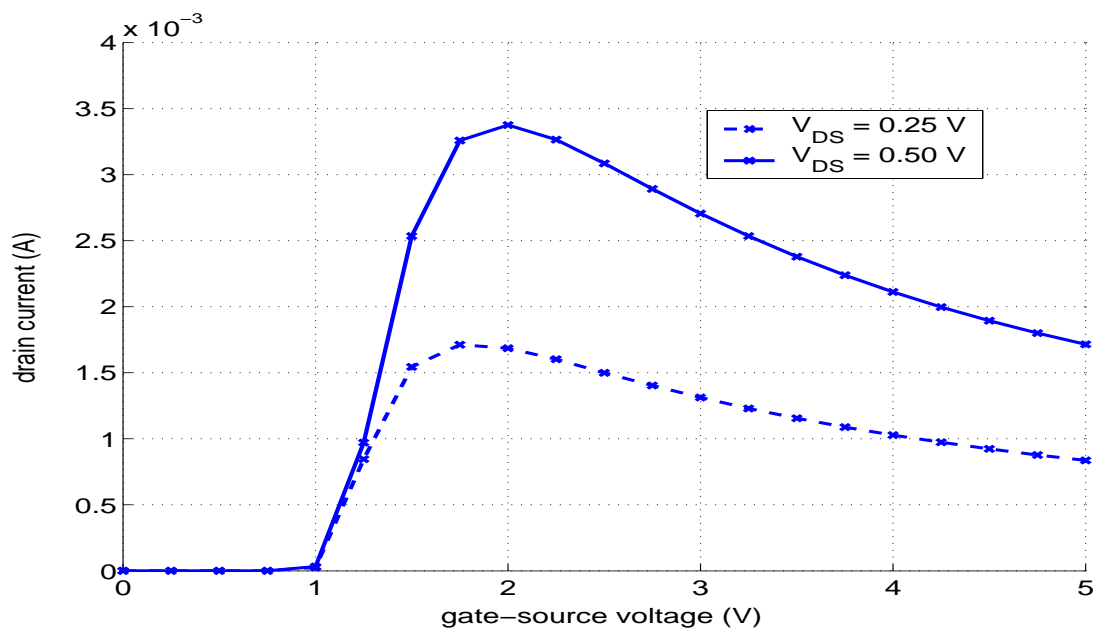


Figure 4.35: Drain current versus gate-source voltage of $0.25\mu\text{m}$ device at room temperature. Notice the decrease in drain current value due to surface roughness after a gate-source voltage of 2 Volts.

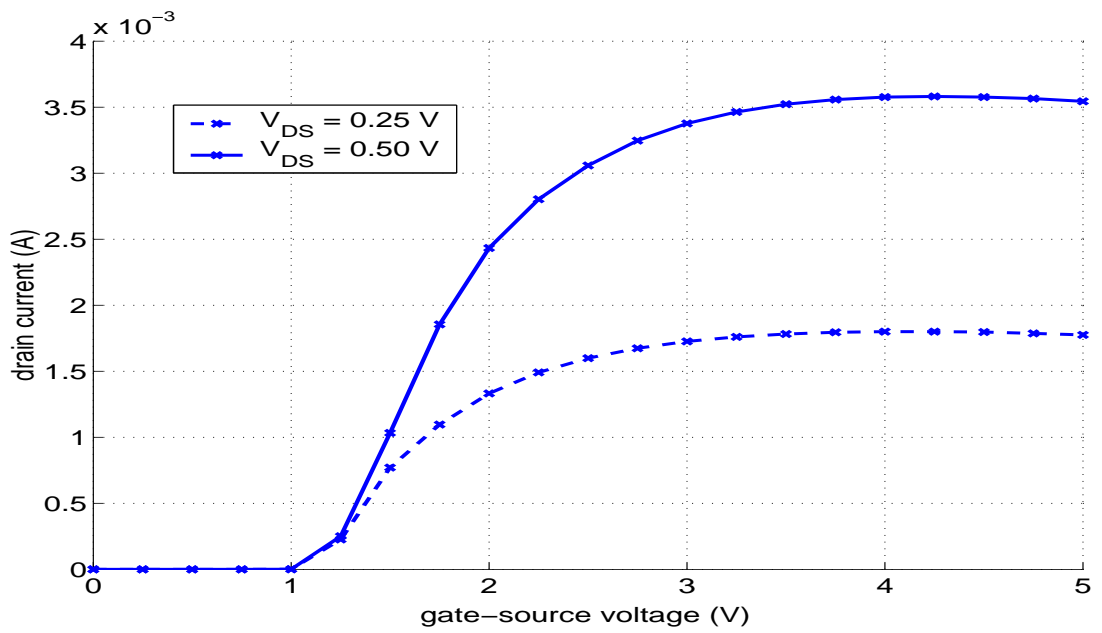


Figure 4.36: Drain current versus gate-source voltage of $0.5\mu\text{m}$ device with improved surface roughness at room temperature. Notice the slight decrease in drain current value due to surface roughness after a gate-source voltage of 4 Volts.

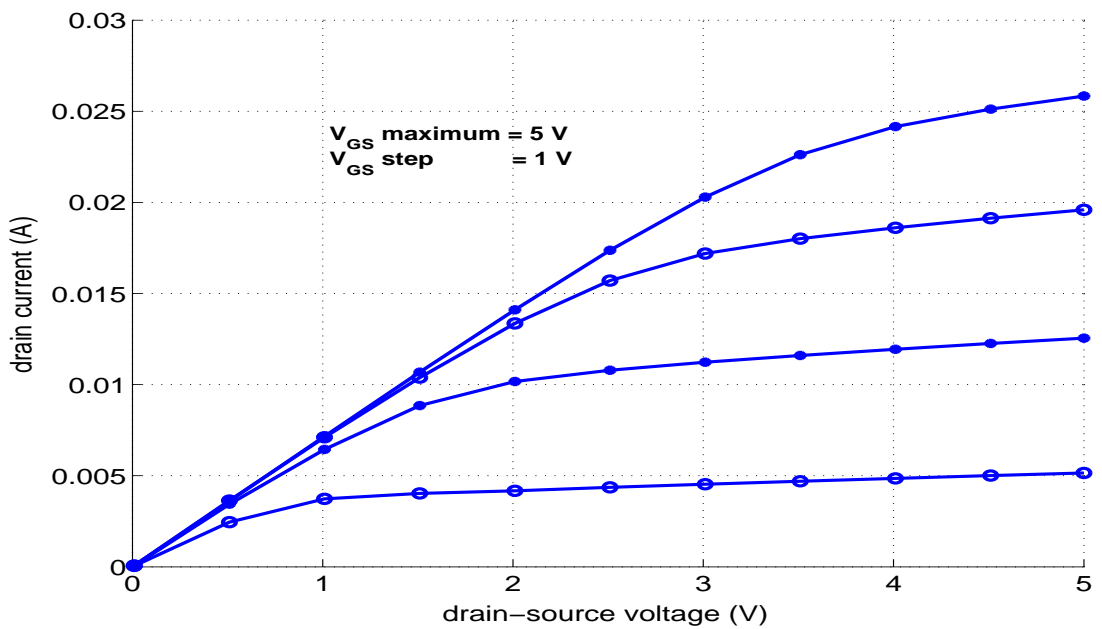


Figure 4.37: Drain current versus gate-source voltage of $0.5\mu\text{m}$ device with improved surface roughness at room temperature.

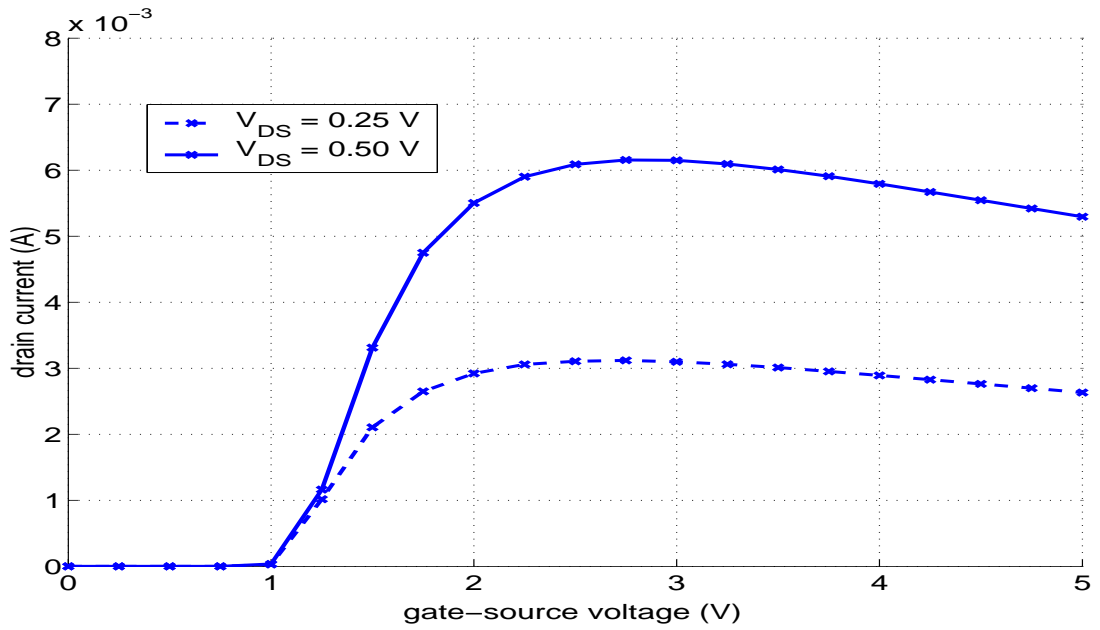


Figure 4.38: Drain current versus gate-source voltage of $0.25\mu\text{m}$ device with improved surface roughness at room temperature. Notice the decrease in drain current value due to surface roughness after a gate-source voltage of 2.5 Volts.

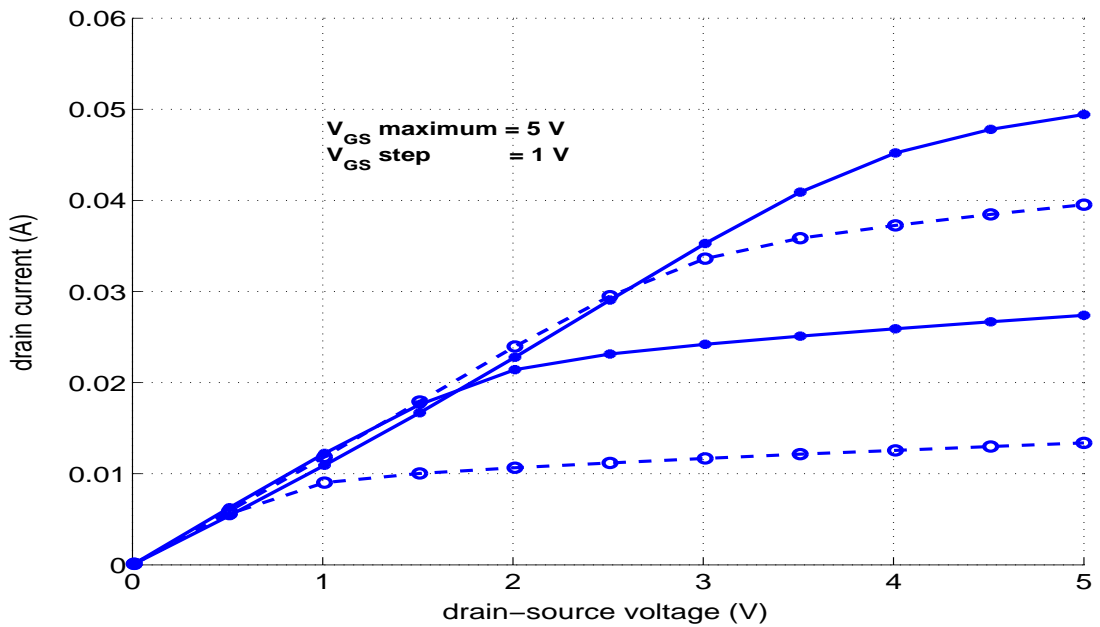


Figure 4.39: Drain current versus gate-source voltage of $0.25\mu\text{m}$ device with improved surface roughness at room temperature.

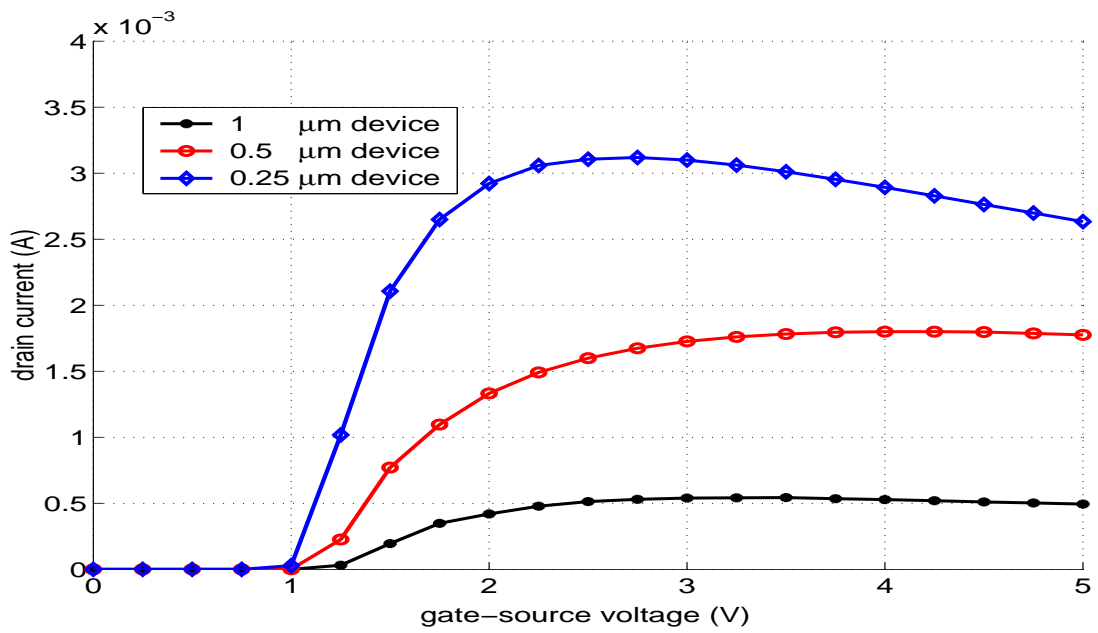


Figure 4.40: Drain current versus gate-source voltage of 1, 0.5, and 0.25 μm devices with improved surface roughness at room temperature.

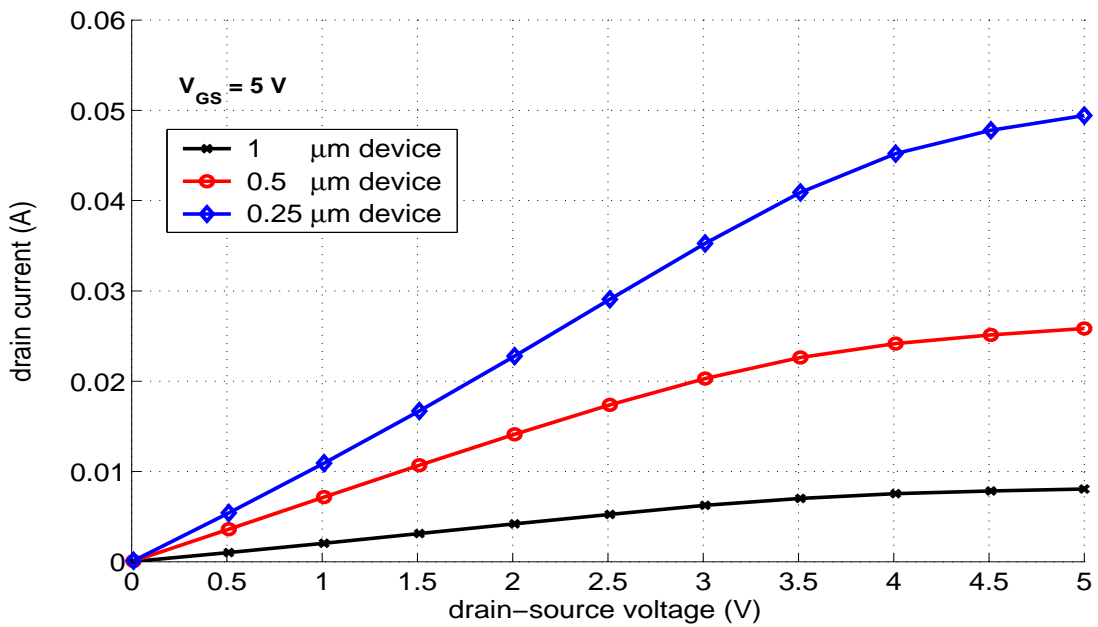


Figure 4.41: Drain current versus drain-source voltage of 1, 0.5, and 0.25 μm devices with improved surface roughness at room temperature. The gate-source voltage is equal to 5 Volts.

Numerical Methods for Drift-Diffusion Heat Flow Simulation in SiC MOSFETs

I have shown the drift-diffusion equations for silicon carbide MOSFETs. Additionally, I have presented data based on this set while never addressing how this set of nonlinear partial differential equations is practically represented and solved. In this chapter, I remove the curtain veiling the wizard known as The Simulator. Namely, I expose my simulation methodologies and implementation techniques which include the following:

- description of the simulation flow process with a qualitative description of each phase of the flow process
- a detailed look of how the world of analytical expressions and symbolic representation is transformed into the realm of numerical approximation with finite difference theory leading the way
- a further look into the two main solving engines of the simulator - the Vectorized Gauss-Seidel (VGS) Engine and the Smart Newton Engine.

5.1 Simulation Flow

Before diving into the specifics of computational mathematics, it is important that readers understand the system flow of the SiC MOSFET drift diffusion heat flow simulator. So, I will spend the next few paragraphs defining the function of each phase of the drift diffusion heat flow Simulator. A flow chart for this system is shown in Figure 5.1.

5.1.1 Phase One - Scoping the Device

In phase one very little computation is done and even less solving is attempted. This phase consists mostly of setting up constraints and conditions based on user input information. First, the user supplies information about the device; the data is formatted then stored into the simulator *Input* structure. This data format contains information such as the device type and geometry, doping profile, device quality metrics (such as surface quality), ambient temperature, simulation specifics, and convergence requirements. Using the *Input* as a recipe for the device to be modelled, the process is ready to *Start*. Following the execution of *Start*, The Simulator computes the *Boundary Conditions* for the device based on information contained in the *Input*. Next, an *Initial Guess* is computed, not only for the electrostatic potential, electron and hole concentrations, and temperature variables but also for variable dependent physical parameters such as mobility, intrinsic carrier concentration, bandgap, etc. The *Initial Guess* results for both variables and variable dependent physical parameters are then passed to the Vectorized Gauss-Seidel

(VGS) Engine, and the process of solving begins. Phase one of the simulation process flow is highlighted in Figure 5.2.

5.1.2 Phase Two - The Vectorized Gauss-Seidel Engine

A flow diagram highlighting phase two of the simulation flow can be found in Figure 5.3, but before the specifics of phase two can be discussed, a review of the Gauss-Seidel method for matrix solving is needed. When using the Gauss-Seidel iterative method for matrix solving, there exists some matrix equation set

$$A\mathbf{x} = \mathbf{b} \quad (5.1)$$

where \mathbf{x} is the unknown vector variable and exact solution to the matrix set, A is the coefficient matrix, and \mathbf{b} is the known product of $A\mathbf{x}$. If a linear iterative method is used, then the problem can be restated as follows:

$$P\mathbf{x}^{(k+1)} = N\mathbf{x}^{(k)} + \mathbf{b}. \quad (5.2)$$

Both P and N are related to A , and

$$\mathbf{x} = \lim_{k \rightarrow \infty} \mathbf{x}^{(k)}. \quad (5.3)$$

If all of the diagonal entries of A are nonzero, the corresponding unknown in each equation can be singled out. Using such a method an equivalent linear system is obtained

$$\mathbf{x}_i = \frac{1}{A_{ii}} \left[b_i - \sum_{j=1, j \neq i}^n A_{ij} x_j \right], \quad i = 1, \dots, n. \quad (5.4)$$

Building on this concept, the Gauss-Seidel linear iterative method uses the available values of $x_i^{(k+1)}$ (values of x_i that have already been computed by the $k + 1$ -th iteration) at the $k + 1$ -th step in order to solve the system. The linear system above is then transformed to

$$\mathbf{x}_i^{(k+1)} = \frac{1}{A_{ii}} \left[b_i - \sum_{j=1}^{i-1} A_{ij} x_j^{(k+1)} - \sum_{j=i+1}^n A_{ij} x_j^{(k)} \right], \quad i = 1, \dots, n. \quad (5.5)$$

In the situation presented in the paragraph above, the variable \vec{x} is computed. The Vectorized Gauss-Seidel Engine uses the principles of Gauss-Seidel, but instead of solving only one variable, it solved for many. For the drift diffusion heat flow equations the matrix set is defined as follows:

$$A_\phi \vec{\phi} = \vec{b}_\phi(\vec{n}, \vec{p}) \quad (5.6)$$

$$A_n(\vec{\phi}) \vec{n} = \vec{b}_n(\vec{p}) \quad (5.7)$$

$$A_p(\vec{\phi}) \vec{p} = \vec{b}_p(\vec{n}) \quad (5.8)$$

where ϕ , n , and p are the electrostatic potential, electron concentration, and hole concentration, respectively. A_ϕ , A_n , and A_p are the coefficient matrices for the Poisson, Electron Continuity, and Hole Continuity equations, respectively ($A_n(\vec{\phi})$ and $A_p(\vec{\phi})$ are functions of ϕ), and $b_\phi(\vec{n}, \vec{p})$, $b_n(\vec{p})$, and $b_p(\vec{n})$ are the respective right

hand sides. Using the concepts of Gauss-Seidel, the following set of equations is obtained

$$P_\phi \vec{\phi}^{(k+1)} = N_\phi \vec{\phi}^{(k)} + \vec{b}_\phi(\vec{n}^{(k)}, \vec{p}^{(k)}) \quad (5.9)$$

$$P_n(\vec{\phi}^{(k+1)}) \vec{n}^{(k+1)} = N_n(\vec{\phi}^{(k+1)}) \vec{n}^{(k)} + \vec{b}_n(\vec{p}^{(k)}) \quad (5.10)$$

$$P_p(\vec{\phi}^{(k+1)}) \vec{p}^{(k+1)} = N_p(\vec{\phi}^{(k+1)}) \vec{p}^{(k)} + \vec{b}_p(\vec{n}^{(k+1)}). \quad (5.11)$$

The details of how matrix sets 5.9-5.11 are solved will be discussed later.

After each of the matrix sets are solved, a *Convergence Test* is conducted in order to determine whether or not The Simulator can move to the next phase. The *Convergence Test* compares the values of ϕ , n , and p before entering the VGS Engine to the values computed after exiting the VGS Engine. If the convergence criteria is not satisfied, this phase moves to the *Update* stage (see Figure 5.3). *Update* sets new pre-VGS values for ϕ , n , and p . After updating is complete, the VGS Engine is re-entered, and this phase is repeated until global convergence is achieved, engine switch convergence is reached, or the maximum number of allowed iteration has been reached.

5.1.3 Phase Three - The Smart Newton Engine

The Smart Newton Engine is used because, like the traditional Newton's Method, it converges faster than Gauss-Seidel based approaches. However, despite

its quickness, Newton's method requires a good initial guess in order for the system variable to converge to the correct solution. In this regard the Smart Newton Engine is not as robust as the VGS Engine. For this reason, I start with the VGS Engine solver and switch to phase three only after the engine switch convergence value has been satisfied for ϕ , n , and p . (Figure 5.5)

Due to the potentially large difference between the electron and hole concentrations in silicon carbide, even a "good Newton guess" can diverge into the numerical abyss. To circumvent this problem, I implement the Smart Newton Engine. Convergence theory dictates that the VGS Engine will eventually converge to the matrix set solution given a reasonable starting point, a well-conditioned coefficient matrix, and enough iterations. Consequently, I know that the VGS Engine is steadily moving towards the numerical solution, and this result has valuable implications. Specifically, I know that the initial Newton guess provided by phase two is moving toward the actual solution. So, if subsequent Smart Newton iterations at particular points in the vector array of ϕ , n , or p begin to diverge greatly from the previous solution at a given point, the newly computed value at that location is rejected and the old one remains. Adding this constraint to Newton's Method requires that memory of the previously computed values must be maintained; thus, the Newton Engine must be *Smart*.

Each time the Smart Newton Engine is executed, a convergence test is done. If global convergence is satisfied, than the system passes to the next phase. Otherwise, phase three moves to the *Update* stage and the Smart Newton process is

repeated.

5.1.4 Phase Four - Calculation of Current and Temperature

Phase four of The Simulator includes calculating the current and solving for the temperature of the SiC MOSFET. Since the variables ϕ , n , and p have been computed to within the error of the pre-specified global convergence and the mobility is known, calculation of electron and hole currents throughout the device is trivial. Using the computed current value, both the heat generation rate and impact ionization rate are computed. After the heat generation rate is calculated, the Simulator solves the heat flow equation for the temperature variable. Once the temperature is computed, another *Convergence Test* is executed comparing the previous and newly calculated values for temperature and the impact ionization rate. If these new values for temperature and impact ionization generation rate have not migrated too far from their pre-phase-four values, the solutions for ϕ , n , p , and T are labelled as accurate and correct. The simulation terminates and output is generated. This path is shown in Figure ???. On the contrary, if the values for temperature or impact ionization generation rate are intolerably different from their pre-phase-four values, *New Boundary Condition* are established (due to the change in temperature), an update is performed, and phase two is re-entered. This path is displayed in Figure ??. The Simulator waives its magic wand again in an effort to solve the drift diffusion heat flow equations until a solution is found or the maximum number of iterations is reached.

5.2 Finite Difference Discretization of the Drift-Diffusion Heat Flow Equations

In order to solve the drift diffusion heat flow equations numerically, each equation must be discretized before the phases mentioned in the previous section can be executed. In this section I present the discretized form for the Poisson, current continuity, and heat flow equations. Formalism of how Poisson's equation and the electron and hole current continuity equation are discretized can be found in [19] and [53]. These same methods are also applied to the heat flow equation.

Each equation is discretized in two dimensions using the finite difference method where each position, (x, y) , in the device is mapped to a mesh point, (i, j) . The position of x , at the i^{th} mesh line is designated by the notation x_i ; likewise, the position of y , at the j^{th} mesh line is designated by the notation y_j . Occasionally, an equation calls for information that has been defined between two mesh points in order to evaluate an expression such as a first order derivative; these points are designated by $(i \pm \frac{1}{2}, j)$ or $(i, j \pm \frac{1}{2})$. The superscript s refers to solutions for the current time iteration while $s + 1$ refers to solutions of the next time iteration where $t^{s+1} = t^s + \Delta t^{s+1}$. Before presenting the discretized equations, I define several variables for convenience of the reader. Presented first is the Bernoulli equation β as a function of the variable γ , and the derivative of the Bernoulli equation, $d\beta$, with respect to γ .

$$\beta(\gamma) = \frac{\gamma}{\exp(\gamma) - 1} \tag{5.12}$$

$$d\beta(\gamma) = \frac{\exp(\gamma) - 1 - \gamma \exp(\gamma)}{(\exp(\gamma) - 1)^2} \quad (5.13)$$

Next are the variables representing the distance between x and y mesh points, respectively.

$$h_i = x_{i+1} - x_i, \quad k_j = y_{j+1} - y_j \quad (5.14)$$

Likewise, I have defined variables that represent the difference between $\phi_{i,j}$ and its neighbors.

$$\begin{aligned} \eta_1 &= \phi_{i,j} - \phi_{i+1,j}, & \eta_3 &= \phi_{i-1,j} - \phi_{i,j} \\ \zeta_1 &= \phi_{i,j} - \phi_{i,j+1}, & \zeta_3 &= \phi_{i,j-1} - \phi_{i,j} \end{aligned} \quad (5.15)$$

Finally, I define variables that are used to combine the mesh and mobility product used in the current continuity equations.

$$\begin{aligned} c_{1n,1p} &= \frac{2k_B}{h_i(h_i + h_{i-1})} \mu_{n,p_{i+\frac{1}{2},j}}, & c_{3n,3p} &= \frac{2k_B}{h_{i-1}(h_i + h_{i-1})} \mu_{n,p_{i-\frac{1}{2},j}} \\ v_{1n,1p} &= \frac{2k_B}{k_j(h_j + h_{j-1})} \mu_{n,p_{i,j+\frac{1}{2}}}, & v_{3n,3p} &= \frac{2k_B}{k_{j-1}(k_j + k_{j-1})} \mu_{n,p_{i,j-\frac{1}{2}}} \end{aligned} \quad (5.16)$$

Poisson's Equation

Poisson's equation gives an analytical representation of the relationship between electrostatic potential, ϕ , and the net charge distribution. For a semicon-

ductor device, this charge distribution is the result of electrons, holes, and ionized dopant sites. Poisson's is shown below.

$$F^\phi = \vec{\nabla}_r^2 \phi - \frac{q}{\epsilon} \{n - p - C(\vec{r}, T)\} = 0 \quad (5.17)$$

Using the principles of centered finite difference, the discretization of Poisson's equation for two dimensional modelling is given by

$$\begin{aligned} F_{i,j}^\phi = & \frac{2}{h_i + h_{i-1}} \left\{ \frac{\phi_{i+1,j}}{h_i} - \left(\frac{1}{h_i} + \frac{1}{h_{i-1}} \right) \phi_{i,j} + \frac{\phi_{i-1,j}}{h_{i-1}} \right\} \\ & + \frac{2}{k_j + k_{j-1}} \left\{ \frac{\phi_{i,j+1}}{k_j} - \left(\frac{1}{k_j} + \frac{1}{k_{j-1}} \right) \phi_{i,j} + \frac{\phi_{i,j-1}}{k_{j-1}} \right\} \\ & - \frac{q}{\epsilon} (n_{i,j} - p_{i,j} - C_{i,j}) = 0. \end{aligned} \quad (5.18)$$

Electron and Hole Continuity Equations

Though Scharfetter and Gummel [54] first formulated the Bernoulli based expression for electron and hole current densities, McAndrew *et al.* [53] derived a current density equation which included both electron and hole temperature. Adding the localized temperature constraint mentioned in chapter 4, I have obtained discretized expressions for both the electron and hole continuity equations.

$$F^n = \vec{\nabla}_r \cdot \vec{J}_n(T) - q \{R(T) - G(T)\} - q \frac{\partial n}{\partial t} = 0 \quad (5.19)$$

and

$$\vec{J}_n(T) = -q\{n\mu_n(T)\vec{\nabla}_r\phi - q\vec{\nabla}_r[nD_n(T)]\} \quad (5.20)$$

are the analytical expressions for both electron continuity and current density equations, respectively. Using the techniques mention above along with the following expressions for midpoint electron current densities

$$J_{n_{i+\frac{1}{2},j}} = \frac{\mu_{n_{i+\frac{1}{2},j}}k_B}{h_i} \left\{ T_{i+1,j}\beta \left(\frac{-\eta_1}{V_{T_{i+1,j}}} \right) n_{i+1,j} - T_{i,j}\beta \left(\frac{\eta_1}{V_{T_{i,j}}} \right) n_{i,j} \right\} \quad (5.21)$$

$$J_{n_{i-\frac{1}{2},j}} = \frac{\mu_{n_{i-\frac{1}{2},j}}k_B}{h_{i-1}} \left\{ T_{i,j}\beta \left(\frac{-\eta_3}{V_{T_{i,j}}} \right) n_{i,j} - T_{i-1,j}\beta \left(\frac{\eta_3}{V_{T_{i-1,j}}} \right) n_{i-1,j} \right\} \quad (5.22)$$

$$J_{n_{i,j+\frac{1}{2}}} = \frac{\mu_{n_{i,j+\frac{1}{2}}}k_B}{k_j} \left\{ T_{i,j+1}\beta \left(\frac{-\zeta_1}{V_{T_{i,j+1}}} \right) n_{i,j+1} - T_{i,j}\beta \left(\frac{\zeta_1}{V_{T_{i,j}}} \right) n_{i,j} \right\} \quad (5.23)$$

$$J_{n_{i,j-\frac{1}{2}}} = \frac{\mu_{n_{i,j-\frac{1}{2}}}k_B}{k_{j-1}} \left\{ T_{i,j}\beta \left(\frac{-\zeta_3}{V_{T_{i,j}}} \right) n_{i,j} - T_{i,j-1}\beta \left(\frac{\zeta_3}{V_{T_{i,j-1}}} \right) n_{i,j-1} \right\} \quad (5.24)$$

the discretized version of the electron continuity equation is represented by

$$\begin{aligned} F_{i,j}^n = & c_{1n}T_{i+1,j}\beta \left(\frac{-\eta_1}{V_{T_{i+1,j}}} \right) n_{i+1,j} + c_{3n}T_{i-1,j}\beta \left(\frac{\eta_3}{V_{T_{i-1,j}}} \right) n_{i-1,j} \\ & - \left\{ c_{1n}\beta \left(\frac{\eta_1}{V_{T_{i,j}}} \right) + c_{3n}\beta \left(\frac{-\eta_3}{V_{T_{i,j}}} \right) \right\} T_{i,j}n_{i,j} \\ & + v_{1n}T_{i,j+1}\beta \left(\frac{-\zeta_1}{V_{T_{i,j+1}}} \right) n_{i,j+1} + v_{3n}T_{i,j-1}\beta \left(\frac{\zeta_3}{V_{T_{i,j-1}}} \right) n_{i,j-1} \\ & - \left\{ v_{1n}\beta \left(\frac{\zeta_1}{V_{T_{i,j}}} \right) + v_{3n}\beta \left(\frac{-\zeta_3}{V_{T_{i,j}}} \right) \right\} T_{i,j}n_{i,j} \\ & - q(R_{i,j} - G_{i,j}) - q \frac{n_{i,j}^{s+1} - n_{i,j}^s}{\Delta t^{s+1}} = 0. \end{aligned} \quad (5.25)$$

Likewise, the hole continuity equation is discretized as follows:

$$\begin{aligned}
F_{i,j}^p &= c_{1p} T_{i+1,j} \beta \left(\frac{\eta_1}{V_{T_{i+1,j}}} \right) p_{i+1,j} + c_{3p} T_{i-1,j} \beta \left(\frac{-\eta_3}{V_{T_{i-1,j}}} \right) p_{i-1,j} \\
&\quad - \left\{ c_{1p} \beta \left(\frac{-\eta_1}{V_{T_{i,j}}} \right) + c_{3p} \beta \left(\frac{\eta_3}{V_{T_{i,j}}} \right) \right\} T_{i,j} p_{i,j} \\
&\quad + v_{1p} T_{i,j+1} \beta \left(\frac{\zeta_1}{V_{T_{i,j+1}}} \right) p_{i,j+1} + v_{3p} T_{i,j-1} \beta \left(\frac{-\zeta_3}{V_{T_{i,j-1}}} \right) p_{i,j-1} \\
&\quad - \left\{ v_{1p} \beta \left(\frac{-\zeta_1}{V_{T_{i,j}}} \right) + v_{3p} \beta \left(\frac{\zeta_3}{V_{T_{i,j}}} \right) \right\} T_{i,j} p_{i,j} \\
&\quad - q(R_{i,j} - G_{i,j}) - q \frac{p_{i,j}^{s+1} - p_{i,j}^s}{\Delta t^{s+1}} = 0.
\end{aligned} \tag{5.26}$$

The midpoint hole current densities are expressed by

$$J_{p_{i+\frac{1}{2},j}} = \frac{-\mu_{p_{i+\frac{1}{2},j}} k_B}{h_i} \left\{ T_{i+1,j} \beta \left(\frac{-\eta_1}{V_{T_{i+1,j}}} \right) p_{i+1,j} - T_{i,j} \beta \left(\frac{\eta_1}{V_{T_{i,j}}} \right) p_{i,j} \right\} \tag{5.27}$$

$$J_{p_{i-\frac{1}{2},j}} = \frac{-\mu_{p_{i-\frac{1}{2},j}} k_B}{h_{i-1}} \left\{ T_{i,j} \beta \left(\frac{-\eta_3}{V_{T_{i,j}}} \right) p_{i,j} - T_{i-1,j} \beta \left(\frac{\eta_3}{V_{T_{i-1,j}}} \right) p_{i-1,j} \right\} \tag{5.28}$$

$$J_{p_{i,j+\frac{1}{2}}} = \frac{-\mu_{p_{i,j+\frac{1}{2}}} k_B}{h_i} \left\{ T_{i,j+1} \beta \left(\frac{-\zeta_1}{V_{T_{i,j+1}}} \right) p_{i,j+1} - T_{i,j} \beta \left(\frac{\zeta_1}{V_{T_{i,j}}} \right) p_{i,j} \right\} \tag{5.29}$$

$$J_{p_{i,j-\frac{1}{2}}} = \frac{-\mu_{p_{i,j-\frac{1}{2}}} k_B}{h_i} \left\{ T_{i,j} \beta \left(\frac{-\zeta_3}{V_{T_{i,j}}} \right) p_{i,j} - T_{i,j-1} \beta \left(\frac{\zeta_3}{V_{T_{i,j-1}}} \right) p_{i,j-1} \right\}. \tag{5.30}$$

Heat Conduction Equation

The heat conduction equation is

$$F^T = \vec{\nabla}_r \cdot \{ \kappa(T) \vec{\nabla}_r T \} + H(T) - c_v \frac{\partial T}{\partial t} = 0 \tag{5.31}$$

where the heat generation rate $H(T)$ is given by

$$H(T) = \{ \vec{J}_n(T) + \vec{J}_p(T) \} \cdot \{ -\vec{\nabla}_r \phi \} + E_g(T) \{ R(T) - G(T) \}, \tag{5.32}$$

T is the lattice temperature, and κ is the thermal conductivity.

First, the partial derivative with respect to x is discretized.

$$\kappa \vec{\nabla}_x T = \kappa \frac{\partial T}{\partial x} \hat{i} = \kappa_{i+\frac{1}{2},j} \frac{T_{i+1,j} - T_{i,j}}{h_i} \hat{i} \quad (5.33)$$

where

$$\kappa_{i+\frac{1}{2},j} = \alpha_T \kappa_0 \left(\frac{0.5 * (T_{i+1,j} + T_{i,j})}{300} \right)^{-\gamma_T}. \quad (5.34)$$

Next, the divergence of $\kappa \frac{\partial T}{\partial x} \hat{i} \big|_{x=i+\frac{1}{2}}$ is evaluated by subtracting the first derivative terms at $(i \pm \frac{1}{2}, j)$ and dividing by the average mesh point difference of h_i and h_{i-1} .

The following is obtained for the x direction,

$$\begin{aligned} \vec{\nabla}_x \cdot \{ \kappa(T) \vec{\nabla}_x T(r) \} &= \frac{\partial}{\partial x} \left(\kappa \frac{\partial T}{\partial x} \right) = \\ &= \frac{\partial}{\partial x} \left(\kappa_{i+\frac{1}{2},j} \frac{T_{i+1,j} - T_{i,j}}{h_i} - \kappa_{i-\frac{1}{2},j} \frac{T_{i,j} - T_{i-1,j}}{h_{i-1}} \right) = \\ &= \frac{2}{h_i + h_{i-1}} \left(\kappa_{i+\frac{1}{2},j} \frac{T_{i+1,j} - T_{i,j}}{h_i} - \kappa_{i-\frac{1}{2},j} \frac{T_{i,j} - T_{i-1,j}}{h_{i-1}} \right). \end{aligned} \quad (5.35)$$

The heat generation rate, $H(T)$, can be discretized directly since values for J_{n_i} , J_{p_i} , E_i (from $-\vec{\nabla}_r \phi$), R_i , G_i , and E_{g_i} have all been evaluated by the time the heat conduction equation is solved. The final form of the two dimensional finite difference discretization of the heat conduction equation is given by

$$\begin{aligned}
F_{i,j}^T = & \frac{2}{h_i + h_{i-1}} \left\{ \frac{\kappa_{i+\frac{1}{2},j}}{h_i} T_{i+1,j} - \left(\frac{\kappa_{i+\frac{1}{2},j}}{h_i} + \frac{\kappa_{i-\frac{1}{2},j}}{h_{i-1}} \right) T_{i,j} + \frac{\kappa_{i-\frac{1}{2},j}}{h_{i-1}} T_{i-1,j} \right\} \\
& + \frac{2}{k_j + k_{j-1}} \left\{ \frac{\kappa_{i,j+\frac{1}{2}}}{k_j} T_{i,j+1} - \left(\frac{\kappa_{i,j+\frac{1}{2}}}{k_j} + \frac{\kappa_{i,j-\frac{1}{2}}}{k_{j-1}} \right) T_{i,j} + \frac{\kappa_{i,j-\frac{1}{2}}}{k_{j-1}} T_{i,j-1} \right\} \\
& + H_{i,j} - c_v \frac{T_{i,j}^{s+1} - T_{i,j}^s}{\Delta t^{s+1}} = 0
\end{aligned} \tag{5.36}$$

$$H_{i,j} = \vec{E}_{i,j} \cdot (\vec{J}_{n_{i,j}} + \vec{J}_{p_{i,j}}) + E_{g_{i,j}}(R_{i,j} - G_{i,j}). \tag{5.37}$$

5.3 Numerical Methods

Up until now I have described the flow process for the drift-diffusion heat flow simulation and presented the discretized versions of each equation used in the simulation process. In this section we will look more closely at the numerical methods used in the VGS, Smart Newton, and Temperature solving phases of the simulator.

Variable Manipulation

Until this point I have presented the drift-diffusion heat flow equations as set of partial differential equations with variables ϕ , n , p , and T . However, the solver implementation used by the Simulator actually solves and performs convergence test on the variables ϕ , ψ_n , ψ_p , and V_T . ϕ , of course, is the electrostatic potential, and V_T is the thermal voltage defined previously as $V_T = \frac{k_B T}{q}$. ψ_n and ψ_p are the quasi-Fermi potential for electrons and holes, respectively.

If the variables ϕ , n , p , and T are solved directly, phase three of the Simulator would have to account for variable variations in the range of 10^{-40} to 10^{20} . Such

a Δ range usually requires additional linear scaling of the equation set in order to achieve convergence. Though this is an acceptable approach, picking the scaling quantities is usually not done *a priori* because it is not known in advance that the computation will fail. In addition to this, scaling constants are sometimes implemented as function of the intrinsic carrier concentration, but this approach is not feasible for two reasons. One, since I have incorporated lattice self-heating, the intrinsic carrier concentration may vary vary drastically within a given group of mesh node, so the scaling is no longer linear, and the equations are no longer valid. Two, for wide bandgap materials such as SiC, the intrinsic carrier concentration is a very low number, and thus does not make a good scaling constant. On the other hand, using ϕ , ψ_n , ψ_p , and V_T , instead, my range variations is limited to approximately $-V_{max}$ to $+V_{max}$ where V_{max} is the absolute value of the maximum applied voltage (assuming that V_{max} is greater than the built-in potential of the device. No scaling is required.

Vectorized Gauss-Seidel Engine

Mentioned earlier, the Vectorized Gauss-Seidel Engine is the first attempt at solving the drift-diffusion equations. At this time I will explain the methods used to solve the Poisson equation as well as the Electron and Hole Continuity Equations.

Poisson Solver Using Fixed Point Newton Method Thus far, I have presented the charge possessing quantities (qn , qp , and qC) of Poisson's equation as though they were independent of the variable ϕ , but this is not true. To the con-

trary, each of these quantities is exponentially dependent on ϕ , and so, for The Simulator, Poisson's equation is more accurately represented by the following

$$F^\phi = \vec{\nabla}_r^2 \phi - \frac{q}{\epsilon} (n(\phi, T) - p(\phi, T) - C(\vec{r}, \phi, T)) = 0 \quad (5.38)$$

where I have now included an explicit ϕ and T dependence on the quantities n , p , and C . Starting with expressing the electron and hole concentrations in terms of quasi-Fermi potentials, I have built on previous work [55, 56] by adding temperature dependence and incomplete ionization.

$$F^\phi = \vec{\nabla}_r^2 \phi - \frac{q}{\epsilon} \left[n_i(T) \exp\left(\frac{\phi - \psi_n}{V_T}\right) - n_i(T) \exp\left(\frac{\psi_p - \phi}{V_T}\right) - \frac{N_d(\vec{r})}{1 + g_d \frac{n_i(T) \exp\left(\frac{\phi - \psi_n}{V_T}\right)}{N_c} \exp\left(\frac{\Delta_d}{k_B T}\right)} + \frac{N_a(\vec{r})}{1 + g_a \frac{n_i(T) \exp\left(\frac{\psi_p - \phi}{V_T}\right)}{N_v} \exp\left(\frac{\Delta_a}{k_B T}\right)} \right] = 0. \quad (5.39)$$

ψ_n and ψ_p are the quasi-Fermi potentials for electrons and holes, respectively. Substituting the appropriate ϕ dependencies, the discretized version of Poisson's equation is

$$\begin{aligned}
F_{i,j}^\phi = & \frac{2}{h_i + h_{i-1}} \left\{ \frac{\phi_{i+1,j}}{h_i} - \left(\frac{1}{h_i} + \frac{1}{h_{i-1}} \right) \phi_{i,j} + \frac{\phi_{i-1,j}}{h_{i-1}} \right\} \\
& + \frac{2}{k_j + k_{j-1}} \left\{ \frac{\phi_{i,j+1}}{k_j} - \left(\frac{1}{k_j} + \frac{1}{k_{j-1}} \right) \phi_{i,j} + \frac{\phi_{i,j-1}}{k_{j-1}} \right\} \\
& - \frac{q}{\epsilon} \left[n_{i,i,j} \exp \left(\frac{\phi_{i,j} - \psi_{n_{i,j}}}{V_{T_{i,j}}} \right) - n_{i,i,j} \exp \left(\frac{\psi_{p_{i,j}} - \phi_{i,j}}{V_{T_{i,j}}} \right) \right. \\
& \quad \left. - \frac{N_{d_{i,j}}}{1 + g_d \frac{n_{i,i,j}}{N_c} \exp \left(\frac{\phi_{i,j} - \psi_{n_{i,j}}}{V_{T_{i,j}}} \right) \exp \left(\frac{\Delta_d}{k_B T_{i,j}} \right)} \right. \\
& \quad \left. + \frac{N_{a_{i,j}}}{1 + g_a \frac{n_{i,i,j}}{N_v} \exp \left(\frac{\psi_{p_{i,j}} - \phi_{i,j}}{V_{T_{i,j}}} \right) \exp \left(\frac{\Delta_a}{k_B T_{i,j}} \right)} \right] = 0.
\end{aligned} \tag{5.40}$$

A closer coupling of the variable $\phi_{i,j}$ to the charge carrying parameters has been achieved, but a nonlinear dependence in $F_{i,j}^\phi$ with respect to $\phi_{i,j}$ has been produced.

In order to handle this issue, I use a variation of the iterative fixed-point method describe in [57, 55, 56]. Because Poisson's equation is presented in such a manner that the entire expression is equal to zero, I need only to solve for the roots of the equation, and since there is a nonlinear dependence on the sought after variable, Newton's method is a prime candidate for solving this set of equations. I begin by solving $f_{i,j}^\phi$ - the partial derivative of $F_{i,j}^\phi$ with respect to $\phi_{i,j}$. $f_{i,j}^\phi$ is shown below.

$$\begin{aligned}
f_{i,j}^\phi = \frac{\partial F_{i,j}^\phi}{\partial \phi_{i,j}} = & -\frac{2}{h_i + h_{i-1}} \left(\frac{1}{h_i} + \frac{1}{h_{i-1}} \right) - \frac{2}{k_j + k_{j-1}} \left(\frac{1}{k_j} + \frac{1}{k_{j-1}} \right) \\
& - \frac{q}{\epsilon} \left[\frac{n_{i,j}}{V_{T_{i,j}}} \exp \left(\frac{\phi_{i,j} - \psi_{n_{i,j}}}{V_{T_{i,j}}} \right) + \frac{n_{i,j}}{V_{T_{i,j}}} \exp \left(\frac{\psi_{p_{i,j}} - \phi_{i,j}}{V_{T_{i,j}}} \right) \right. \\
& \quad + \frac{\frac{g_d}{V_{T_{i,j}}} \frac{n_{i,j}}{N_c} \exp \left(\frac{\Delta_d}{k_B T_{i,j}} \right) N_{d_{i,j}}}{\left[1 + g_d \frac{n_{i,j}}{N_c} \exp \left(\frac{\Delta_d}{k_B T_{i,j}} \right) \exp \left(\frac{\phi_{i,j} - \psi_{n_{i,j}}}{V_{T_{i,j}}} \right) \right]^2} \\
& \quad \left. + \frac{\frac{g_a}{V_{T_{i,j}}} \frac{n_{i,j}}{N_v} \exp \left(\frac{\Delta_a}{k_B T_{i,j}} \right) N_{a_{i,j}}}{\left[1 + g_a \frac{n_{i,j}}{N_v} \exp \left(\frac{\Delta_a}{k_B T_{i,j}} \right) \exp \left(\frac{\psi_{p_{i,j}} - \phi_{i,j}}{V_{T_{i,j}}} \right) \right]^2} \right].
\end{aligned} \tag{5.41}$$

Applying the principles of Newton's method, I obtain

$$F_{i,j}^\phi(\phi_{i,j} + \Delta\phi_{i,j}) = F_{i,j}^\phi(\phi_{i,j}) + f_{i,j}^\phi(\phi_{i,j})\Delta\phi_{i,j} = 0 \tag{5.42}$$

and use this relationship to solve for the change in $\phi_{i,j}$, $\Delta\phi_{i,j}$. Specifically,

$$\Delta\phi_{i,j} = \frac{F_{i,j}^\phi(\phi_{i,j})}{f_{i,j}^\phi(\phi_{i,j})}. \tag{5.43}$$

For a given mesh point (i, j) , $\Delta\phi_{i,j}$ is continually computed and $\phi_{i,j}$ continually updated until $|\Delta\phi_{i,j}|$ is smaller than some pre-specified convergence value or a maximum iteration value is reached. This process is repeated for every mesh point not on the boundary. Once all non-boundary points in $\vec{\phi}$ have been computed, The Simulator exits the Poisson solver portion of the VGS Engine.

Linear Iteration and the Continuity Equations As stated in the section on simulation process flow, once the fixed-point Newton method is used to solve

Poisson's equation, the computed values of $\vec{\phi}$ are used to solve the Electron and Hole Continuity equations. Like Poisson's equation the Electron and Hole Continuity equations are non-linear, but unlike Poisson's equation, the non-linearity in the continuity equations very subtle and can be ignored without reeking havoc on linear iterative solving techniques. For convenience I have included the discretized electron current continuity equation below.

$$\begin{aligned}
& c_{1n}T_{i+1,j}\beta \left(\frac{-\eta_1}{V_{T_{i+1,j}}} \right) n_{i+1,j} + c_{3n}T_{i-1,j}\beta \left(\frac{\eta_3}{V_{T_{i-1,j}}} \right) n_{i-1,j} \\
& + v_{1n}T_{i,j+1}\beta \left(\frac{-\zeta_1}{V_{T_{i,j+1}}} \right) n_{i,j+1} + v_{3n}T_{i,j-1}\beta \left(\frac{\zeta_3}{V_{T_{i,j-1}}} \right) n_{i,j-1} \\
& \hspace{20em} + qG_{i,j} \\
& = \left\{ c_{1n}\beta \left(\frac{\eta_1}{V_{T_{i,j}}} \right) + c_{3n}\beta \left(\frac{-\eta_3}{V_{T_{i,j}}} \right) \right. \\
& \quad \left. + v_{1n}\beta \left(\frac{\zeta_1}{V_{T_{i,j}}} \right) + v_{3n}\beta \left(\frac{-\zeta_3}{V_{T_{i,j}}} \right) \right\} T_{i,j}n_{i,j} \\
& \hspace{20em} + qR_{i,j}
\end{aligned} \tag{5.44}$$

where the carrier recombination rate is defined as follows:

$$\begin{aligned}
R_{i,j} = & \frac{(n_{i,j}p_{i,j} - n_{i,j}^2)}{\tau_{n_{i,j}}(p_{i,j} + n_{i,j}) + \tau_{p_{i,j}}(n_{i,j} + n_{i,j})} \\
& + (n_{i,j}p_{i,j} - n_{i,j}^2)(C_n n + C_p p).
\end{aligned} \tag{5.45}$$

Rearranging the equality so that the only $n_{i,j}$ is present on the left hand side results in the following

$$\begin{aligned}
& n_{i,j} = \tag{5.46} \\
& \frac{\alpha_{i+1,j}n_{i+1,j} + \beta_{i-1,j}n_{i-1,j} + \gamma_{i,j+1}n_{i,j+1} + \delta_{i,j-1}n_{i,j-1} + qG_{i,j} + qn_{i,j}^2 \left(\frac{1}{\Gamma_{i,j}} + \Pi_{i,j} \right)}{\left\{ \alpha_{i,j} + \beta_{i,j} + \gamma_{i,j} + \delta_{i,j} \right\} T_{i,j} + qp_{i,j} \left(\frac{1}{\Gamma_{i,j}} + \Pi_{i,j} \right)}.
\end{aligned}$$

α , β , γ , δ , Γ , and Π are defined below.

$$\begin{aligned}
\alpha_{i+1,j} &= c_{1n} T_{i+1,j} \beta \left(\frac{-\eta_1}{V_{T_{i+1,j}}} \right), & \alpha_{i,j} &= c_{1n} \beta \left(\frac{\eta_1}{V_{T_{i,j}}} \right) & \tag{5.47} \\
\beta_{i-1,j} &= c_{3n} T_{i-1,j} \beta \left(\frac{\eta_3}{V_{T_{i-1,j}}} \right), & \beta_{i,j} &= c_{3n} \beta \left(\frac{-\eta_3}{V_{T_{i,j}}} \right) \\
\gamma_{i,j+1} &= v_{1n} T_{i,j+1} \beta \left(\frac{-\zeta_1}{V_{T_{i,j+1}}} \right), & \gamma_{i,j} &= v_{1n} \beta \left(\frac{\zeta_1}{V_{T_{i,j}}} \right) \\
\delta_{i,j-1} &= v_{3n} T_{i,j-1} \beta \left(\frac{\zeta_3}{V_{T_{i,j-1}}} \right), & \delta_{i,j} &= v_{3n} T_{i,j-1} \beta \left(\frac{-\zeta_3}{V_{T_{i,j}}} \right) \\
\Gamma_{i,j} &= \tau_{n_{i,j}}(p_{i,j} + n_{i,j}) + \tau_{p_{i,j}}(n_{i,j} + n_{i,j}) & \Pi_{i,j} &= (C_n n_{i,j} + C_p p_{i,j}).
\end{aligned}$$

Arranging the electron current continuity equation this way, transforming it to a form suitable for linear iteration is trivial. This form is shown below.

$$n_{i,j}^{k+1} = \left. \frac{1}{\left\{ \alpha_{i,j}^m + \beta_{i,j}^m + \gamma_{i,j}^m + \delta_{i,j}^m \right\} T_{i,j} + qP_{i,j}^m \left(\frac{1}{\Gamma_{i,j}^k} + \Pi_{i,j}^k \right)} \right\} \quad (5.48)$$

$$\begin{aligned} & \alpha_{i+1,j}^m n_{i+1,j} \exp \left(\frac{\phi_{i+1,j}^m - \psi_{n_{i+1,j}}^k}{V_{T_{i+1,j}}} \right) \\ & + \beta_{i-1,j}^m n_{i-1,j} \exp \left(\frac{\phi_{i-1,j}^m - \psi_{n_{i-1,j}}^k}{V_{T_{i-1,j}}} \right) \\ & + \gamma_{i,j+1}^m n_{i,j+1} \exp \left(\frac{\phi_{i,j+1}^m - \psi_{n_{i,j+1}}^k}{V_{T_{i,j+1}}} \right) \\ & + \delta_{i,j-1}^m n_{i,j-1} \exp \left(\frac{\phi_{i,j-1}^m - \psi_{n_{i,j-1}}^k}{V_{T_{i,j-1}}} \right) \\ & \left. + qG_{i,j} + qn_{i,j}^2 \left(\frac{1}{\Gamma_{i,j}^k} + \Pi_{i,j}^k \right) \right\} \end{aligned}$$

In Equation 5.49 m refers to the most recently computed value of the electrostatic potential gained by solving Poisson's equation. k refers to values of $\psi_{n_{i,j}}$ and $n_{i,j}$ from the previous linear iteration of the electron current continuity equation. $k + 1$ is the current linear iteration in which $n_{i,j}$ is being solved. Due to the small impact of changes in $\Gamma_{i,j}$ and $\Pi_{i,j}$ as a result of changes in $n_{i,j}$, these $n_{i,j}$ dependent terms are kept on the left right hand side of the equation. After each step of a particular iteration is completed, the electron concentration is converted to quasi-Fermi potential (Equation 5.49), and a converge test is performed on the quasi-Fermi potential. Mentioned previously, this process is repeated for each non-boundary mesh point node until convergence is achieved or the maximum number of solving attempts is reached. A similar process is done for the hole current continuity equation.

$$\psi_{n_{i,j}}^{k+1} = \phi_{i,j}^m - V_{T_{i,j}} \ln \left(\frac{n_{i,j}^{k+1}}{n_{i,j}} \right) \quad (5.49)$$

Smart Newton Engine

Once the errors between VGS Engine iterations for ϕ , ψ_n , and ψ_p have dropped below the specified threshold (the engine switch value), the Smart Newton Engine is entered. Unlike the VGS Engine, the drift-diffusion heat flow equations remain coupled, and so ϕ , ψ_n , and ψ_p must be computed simultaneously. This is accomplished by defining a Jacobian matrix and solving for the changes in the three variable between iterations. This process is represented mathematically in Equation 5.50. The vector symbol \vec{x} (x is used in place of ϕ , ψ_n , and ψ_p) is used to signify that an operation is performed for all non-boundary mesh points of the variables ϕ , ψ_n , and ψ_p .

$$\begin{bmatrix} \frac{\partial F_\phi^k}{\partial \vec{\phi}} & \frac{\partial F_\phi^k}{\partial \vec{\psi}_n} & \frac{\partial F_\phi^k}{\partial \vec{\psi}_p} \\ \frac{\partial F_n^\psi^k}{\partial \vec{\phi}} & \frac{\partial F_n^\psi^k}{\partial \vec{\psi}_n} & \frac{\partial F_n^\psi^k}{\partial \vec{\psi}_p} \\ \frac{\partial F_p^\psi^k}{\partial \vec{\phi}} & \frac{\partial F_p^\psi^k}{\partial \vec{\psi}_n} & \frac{\partial F_p^\psi^k}{\partial \vec{\psi}_p} \end{bmatrix} \begin{bmatrix} \Delta \vec{\phi}^k \\ \Delta \vec{\psi}_n^k \\ \Delta \vec{\psi}_p^k \end{bmatrix} = \begin{bmatrix} -F_\phi^k \\ -F_n^\psi^k \\ -F_p^\psi^k \end{bmatrix}. \quad (5.50)$$

Once the Smart Newton matrix is solved, updates to the variables are made using the following

$$\vec{x}^{k+1} = \vec{x}^k + \Delta \vec{x}^k \quad (5.51)$$

where \vec{x} may be the vector variable ϕ , ψ_n , or ψ_p .

I have already shown that the functions F^ϕ , F^{ψ_n} , and F^{ψ_p} are equal to zero; thus, the Smart Newton Engine is a root solver. In the following pages, I present the matrix elements of the Smart Newton Jacobi, starting with the partial derivatives of F^ϕ , the first row. Rewriting the first row using products and summations, the following is obtained.

$$F_{i,j}^\phi(\vec{\phi} + \Delta\vec{\phi}, \vec{\psi}_n + \Delta\vec{\psi}_n, \vec{\psi}_p + \Delta\vec{\psi}_p) = \quad (5.52)$$

$$F_{i,j}^\phi(\vec{\phi}, \vec{\psi}_n, \vec{\psi}_p) + \frac{\partial F_{i,j}^\phi}{\partial \vec{\phi}} \Delta\vec{\phi} + \frac{\partial F_{i,j}^\phi}{\partial \vec{\psi}_n} \Delta\vec{\psi}_n + \frac{\partial F_{i,j}^\phi}{\partial \vec{\psi}_p} \Delta\vec{\psi}_p = 0.$$

Each of the partial differential expressions for $F_{i,j}^\phi$ is given below, explicitly.

$$\begin{aligned} \frac{\partial F_{i,j}^\phi}{\partial \phi_{i,j}} = & -\frac{2}{h_i + h_{i-1}} \left(\frac{1}{h_i} + \frac{1}{h_{i-1}} \right) - \frac{2}{k_j + k_{j-1}} \left(\frac{1}{k_j} + \frac{1}{k_{j-1}} \right) \quad (5.53) \\ & -\frac{q}{\epsilon} \left[\frac{n_{i,j}}{V_{T_{i,j}}} \exp\left(\frac{\phi_{i,j} - \psi_{n_{i,j}}}{V_{T_{i,j}}}\right) + \frac{n_{i,j}}{V_{T_{i,j}}} \exp\left(\frac{\psi_{p_{i,j}} - \phi_{i,j}}{V_{T_{i,j}}}\right) \right. \\ & \quad \left. + \frac{\frac{g_d}{V_{T_{i,j}}} \frac{n_{i,j}}{N_c} \exp\left(\frac{\Delta_d}{k_B T_{i,j}}\right) N_{d_{i,j}}}{\left[1 + g_d \frac{n_{i,j}}{N_c} \exp\left(\frac{\Delta_d}{k_B T_{i,j}}\right) \exp\left(\frac{\phi_{i,j} - \psi_{n_{i,j}}}{V_{T_{i,j}}}\right)\right]^2} \right. \\ & \quad \left. + \frac{\frac{g_a}{V_{T_{i,j}}} \frac{n_{i,j}}{N_v} \exp\left(\frac{\Delta_a}{k_B T_{i,j}}\right) N_{a_{i,j}}}{\left[1 + g_a \frac{n_{i,j}}{N_v} \exp\left(\frac{\Delta_a}{k_B T_{i,j}}\right) \exp\left(\frac{\psi_{p_{i,j}} - \phi_{i,j}}{V_{T_{i,j}}}\right)\right]^2} \right] \end{aligned}$$

$$\frac{\partial F_{i,j}^\phi}{\partial \phi_{i+1,j}} = \frac{2}{h_i(h_i + h_{i-1})} \quad (5.54)$$

$$\frac{\partial F_{i,j}^\phi}{\partial \phi_{i-1,j}} = \frac{2}{h_{i-1}(h_i + h_{i-1})} \quad (5.55)$$

$$\frac{\partial F_{i,j}^\phi}{\partial \phi_{i,j+1}} = \frac{2}{k_j(k_j + k_{j-1})} \quad (5.56)$$

$$\frac{\partial F_{i,j}^\phi}{\partial \phi_{i,j-1}} = \frac{2}{k_{j-1}(k_j + k_{j-1})} \quad (5.57)$$

$$\frac{\partial F_{i,j}^\phi}{\partial \psi_{n_{i,j}}} = \frac{q}{\epsilon} \frac{n_{i,j}}{V_{T_{i,j}}} \exp\left(\frac{\phi_{i,j} - \psi_{n_{i,j}}}{V_{T_{i,j}}}\right) \quad (5.58)$$

$$\frac{\partial F_{i,j}^\phi}{\partial \psi_{n_{i+1,j}}} = \frac{\partial F_{i,j}^\phi}{\partial \psi_{n_{i-1,j}}} = \frac{\partial F_{i,j}^\phi}{\partial \psi_{n_{i,j+1}}} = \frac{\partial F_{i,j}^\phi}{\partial \psi_{n_{i,j-1}}} = 0 \quad (5.59)$$

$$\frac{\partial F_{i,j}^\phi}{\partial \psi_{p_{i,j}}} = \frac{q}{\epsilon} \frac{n_{i,j}}{V_{T_{i,j}}} \exp\left(\frac{\psi_{p_{i,j}} - \phi_{i,j}}{V_{T_{i,j}}}\right) \quad (5.60)$$

$$\frac{\partial F_{i,j}^\phi}{\partial \psi_{p_{i+1,j}}} = \frac{\partial F_{i,j}^\phi}{\partial \psi_{p_{i-1,j}}} = \frac{\partial F_{i,j}^\phi}{\partial \psi_{p_{i,j+1}}} = \frac{\partial F_{i,j}^\phi}{\partial \psi_{p_{i,j-1}}} = 0 \quad (5.61)$$

Recalling the relationship between the electron concentration $n_{i,j}$ and electron quasi-Fermi potential $\psi_{n_{i,j}}$ (Equation 5.62), a direct translation from $F_{i,j}^n$ to $F_{i,j}^{\psi_n}$ can be easily made,

$$n_{i,j} = n_{i,j} \exp\left(\frac{\phi_{i,j} - \psi_{n_{i,j}}}{V_{T_{i,j}}}\right) \quad (5.62)$$

$$F_{i,j}^n = F_{i,j}^{\psi_n} \quad (5.63)$$

and the partial derivatives are computed as they were for the electrostatic potential.

$$F_{i,j}^{\psi_n}(\vec{\phi} + \Delta\vec{\phi}, \vec{\psi}_n + \Delta\vec{\psi}_n, \vec{\psi}_p + \Delta\vec{\psi}_p) = \quad (5.64)$$

$$F_{i,j}^{\psi_n}(\vec{\phi}, \vec{\psi}_n, \vec{\psi}_p) + \frac{\partial F_{i,j}^{\psi_n}}{\partial \vec{\phi}} \Delta\vec{\phi} + \frac{\partial F_{i,j}^{\psi_n}}{\partial \vec{\psi}_n} \Delta\vec{\psi}_n + \frac{\partial F_{i,j}^{\psi_n}}{\partial \vec{\psi}_p} \Delta\vec{\psi}_p = 0$$

$$\frac{\partial F_{i,j}^{\psi_n}}{\partial \psi_{n_{i,j}}} = \frac{T_{i,j}}{V_{T_{i,j}}} n_{i,j} \left\{ c_{1n} \beta \left(\frac{\eta_1}{V_{T_{i,j}}} \right) + c_{3n} \beta \left(\frac{-\eta_3}{V_{T_{i,j}}} \right) \right. \quad (5.65)$$

$$\left. + v_{1n} \beta \left(\frac{\zeta_1}{V_{T_{i,j}}} \right) + v_{3n} \beta \left(\frac{-\zeta_3}{V_{T_{i,j}}} \right) \right\}$$

$$+ \frac{q}{V_{T_{i,j}}} \frac{(n_{i,j} \tau_{p_{i,j}} + p_{i,j} \tau_{n_{i,j}})(n_{i,j} + p_{i,j})}{\left((n_{i,j} + n_{i,j}) \tau_{p_{i,j}} + (p_{i,j} + n_{i,j}) \tau_{n_{i,j}} \right)^2}$$

$$+ \frac{q}{V_{T_{i,j}}} \left(p_{i,j} (C_n n_{i,j} + C_p p_{i,j}) + C_n (n_{i,j} p_{i,j}) - n_{i,j}^2 \right)$$

$$\frac{\partial F_{i,j}^{\psi_n}}{\partial \psi_{n_{i+1,j}}} = -c_{1n} \frac{T_{i+1,j}}{V_{T_{i+1,j}}} \beta \left(\frac{-\eta_1}{V_{T_{i+1,j}}} \right) n_{i+1,j} \quad (5.66)$$

$$\frac{\partial F_{i,j}^{\psi_n}}{\partial \psi_{n_{i-1,j}}} = -c_{3n} \frac{T_{i-1,j}}{V_{T_{i-1,j}}} \beta \left(\frac{\eta_3}{V_{T_{i-1,j}}} \right) n_{i-1,j} \quad (5.67)$$

$$\frac{\partial F_{i,j}^{\psi_n}}{\partial \psi_{n_{i,j+1}}} = -v_{1n} \frac{T_{i,j+1}}{V_{T_{i,j+1}}} \beta \left(\frac{-\zeta_1}{V_{T_{i,j+1}}} \right) n_{i,j+1} \quad (5.68)$$

$$\frac{\partial F_{i,j}^{\psi_n}}{\partial \psi_{n_{i,j-1}}} = -v_{3n} \frac{T_{i,j-1}}{V_{T_{i,j-1}}} \beta \left(\frac{\zeta_3}{V_{T_{i,j-1}}} \right) n_{i,j-1} \quad (5.69)$$

$$\begin{aligned} \frac{\partial F_{i,j}^{\psi_n}}{\partial \phi_{i,j}} &= -c_{1n} \frac{T_{i+1,j}}{V_{T_{i+1,j}}} d\beta \left(\frac{-\eta_1}{V_{T_{i+1,j}}} \right) n_{i+1,j} \\ &\quad - c_{3n} \frac{T_{i-1,j}}{V_{T_{i-1,j}}} d\beta \left(\frac{\eta_3}{V_{T_{i-1,j}}} \right) n_{i-1,j} \\ &\quad - \frac{T_{i,j}}{V_{T_{i,j}}} n_{i,j} \left\{ c_{1n} \left[d\beta \left(\frac{\eta_1}{V_{T_{i,j}}} \right) + \beta \left(\frac{\eta_1}{V_{T_{i,j}}} \right) \right] \right. \\ &\quad \left. + c_{3n} \left[d\beta \left(\frac{-\eta_3}{V_{T_{i,j}}} \right) + \beta \left(\frac{-\eta_3}{V_{T_{i,j}}} \right) \right] \right\} \\ &\quad - v_{1n} \frac{T_{i,j+1}}{V_{T_{i,j+1}}} d\beta \left(\frac{-\zeta_1}{V_{T_{i,j+1}}} \right) n_{i,j+1} \\ &\quad - v_{3n} \frac{T_{i,j-1}}{V_{T_{i,j-1}}} d\beta \left(\frac{\zeta_3}{V_{T_{i,j-1}}} \right) n_{i,j-1} \\ &\quad - \frac{T_{i,j}}{V_{T_{i,j}}} n_{i,j} \left\{ v_{1n} \left[d\beta \left(\frac{\zeta_1}{V_{T_{i,j}}} \right) + \beta \left(\frac{\zeta_1}{V_{T_{i,j}}} \right) \right] \right. \\ &\quad \left. + v_{3n} \left[d\beta \left(\frac{-\zeta_3}{V_{T_{i,j}}} \right) + \beta \left(\frac{-\zeta_3}{V_{T_{i,j}}} \right) \right] \right\} \\ &\quad - \frac{\frac{q}{V_{T_{i,j}}} (n_{i,j} \tau_{p_{i,j}} + p_{i,j} \tau_{n_{i,j}}) (n_{i,j} + p_{i,j})}{\left((n_{i,j} + n_{i,j}) \tau_{p_{i,j}} + (p_{i,j} + n_{i,j}) \tau_{n_{i,j}} \right)^2} \\ &\quad - \frac{q}{V_{T_{i,j}}} (n_{i,j} p_{i,j} - n_{i,j}^2) (C_p p_{i,j} - C_n n_{i,j}) \end{aligned} \quad (5.70)$$

$$\begin{aligned} \frac{\partial F_{i,j}^{\psi_n}}{\partial \phi_{i+1,j}} &= c_{1n} \frac{T_{i,j}}{V_{T_{i,j}}} n_{i,j} d\beta \left(\frac{\eta_1}{V_{T_{i,j}}} \right) \\ &\quad + c_{1n} \frac{T_{i+1,j}}{V_{T_{i+1,j}}} n_{i+1,j} \left[d\beta \left(\frac{-\eta_1}{V_{T_{i+1,j}}} \right) + \beta \left(\frac{-\eta_1}{V_{T_{i+1,j}}} \right) \right] \end{aligned} \quad (5.71)$$

$$\begin{aligned} \frac{\partial F_{i,j}^{\psi_n}}{\partial \phi_{i-1,j}} &= c_{3n} \frac{T_{i,j}}{V_{T_{i,j}}} n_{i,j} d\beta \left(\frac{-\eta_3}{V_{T_{i,j}}} \right) \\ &+ c_{3n} \frac{T_{i-1,j}}{V_{T_{i-1,j}}} n_{i-1,j} \left[d\beta \left(\frac{\eta_3}{V_{T_{i-1,j}}} \right) + \beta \left(\frac{\eta_3}{V_{T_{i-1,j}}} \right) \right] \end{aligned} \quad (5.72)$$

$$\begin{aligned} \frac{\partial F_{i,j}^{\psi_n}}{\partial \phi_{i,j+1}} &= v_{1n} \frac{T_{i,j}}{V_{T_{i,j}}} n_{i,j} d\beta \left(\frac{\zeta_1}{V_{T_{i,j}}} \right) \\ &+ v_{1n} \frac{T_{i,j+1}}{V_{T_{i,j+1}}} n_{i,j+1} \left[d\beta \left(\frac{-\zeta_1}{V_{T_{i,j+1}}} \right) + \beta \left(\frac{-\zeta_1}{V_{T_{i,j+1}}} \right) \right] \end{aligned} \quad (5.73)$$

$$\begin{aligned} \frac{\partial F_{i,j}^{\psi_n}}{\partial \phi_{i,j-1}} &= v_{3n} \frac{T_{i,j}}{V_{T_{i,j}}} n_{i,j} d\beta \left(\frac{-\zeta_3}{V_{T_{i,j}}} \right) \\ &+ v_{3n} \frac{T_{i,j-1}}{V_{T_{i,j-1}}} n_{i,j-1} \left[d\beta \left(\frac{\zeta_3}{V_{T_{i,j-1}}} \right) + \beta \left(\frac{\zeta_3}{V_{T_{i,j-1}}} \right) \right] \end{aligned} \quad (5.74)$$

$$\begin{aligned} \frac{\partial F_{i,j}^{\psi_n}}{\partial \psi_{p_{i,j}}} &= \frac{-\frac{q}{V_{T_{i,j}}} (n_{i,i,j} \tau_{p_{i,j}} + n_{i,j} \tau_{n_{i,j}}) (n_{i,i,j} + n_{i,j})}{\left((p_{i,j} + n_{i,i,j}) \tau_{n_{i,j}} + (n_{i,j} + n_{i,i,j}) \tau_{p_{i,j}} \right)^2} \\ &- \frac{q}{V_{T_{i,j}}} \left(p_{i,j} (C_n n_{i,j} + C_p p_{i,j}) + C_n (n_{i,j} p_{i,j} - n_{i,i,j}^2) \right) \end{aligned} \quad (5.75)$$

$$\frac{\partial F_{i,j}^{\psi_n}}{\partial \psi_{p_{i+1,j}}} = \frac{\partial F_{i,j}^{\psi_n}}{\partial \psi_{p_{i-1,j}}} = \frac{\partial F_{i,j}^{\psi_n}}{\partial \psi_{p_{i,j+1}}} = \frac{\partial F_{i,j}^{\psi_n}}{\partial \psi_{p_{i,j-1}}} = 0 \quad (5.76)$$

Similarly, the derivatives of the hole function are computed.

$$p_{i,j} = n_{i,i,j} \exp \left(\frac{\psi_{p_{i,j}} - \phi_{i,j}}{V_{T_{i,j}}} \right) \quad (5.77)$$

$$F_{i,j}^p = F_{i,j}^{\psi_p} \quad (5.78)$$

$$\begin{aligned} F_{i,j}^{\psi_p}(\vec{\phi} + \Delta\vec{\phi}, \vec{\psi}_n + \Delta\vec{\psi}_n, \vec{\psi}_p + \Delta\vec{\psi}_p) = \\ \frac{\partial F_{i,j}^{\psi_p}}{\partial \vec{\phi}} \Delta\vec{\phi} + \frac{\partial F_{i,j}^{\psi_p}}{\partial \vec{\psi}_n} \Delta\vec{\psi}_n + \frac{\partial F_{i,j}^{\psi_p}}{\partial \vec{\psi}_p} \Delta\vec{\psi}_p = 0 \end{aligned} \quad (5.79)$$

$$\begin{aligned} \frac{\partial F_{i,j}^{\psi_p}}{\partial \psi_{p_{i,j}}} = -\frac{T_{i,j}}{V_{T_{i,j}}} p_{i,j} \left\{ c_{1n}\beta \left(\frac{-\eta_1}{V_{T_{i,j}}} \right) + c_{3n}\beta \left(\frac{\eta_3}{V_{T_{i,j}}} \right) \right. \\ \left. + v_{1n}\beta \left(\frac{-\zeta_1}{V_{T_{i,j}}} \right) + v_{3n}\beta \left(\frac{\zeta_3}{V_{T_{i,j}}} \right) \right\} \\ - \frac{\frac{q}{V_{T_{i,j}}} (n_{i,j}\tau_{p_{i,j}} + n_{i,j}\tau_{n_{i,j}})(n_{i,j} + n_{i,j})}{\left((n_{i,j} + n_{i,j})\tau_{p_{i,j}} + (p_{i,j} + n_{i,j})\tau_{n_{i,j}} \right)^2} \\ - \frac{q}{V_{T_{i,j}}} \left(ni, j(C_n n_{i,j} + C_p p_{i,j}) + C_p(n_{i,j} p_{i,j} - n_{i,j}^2) \right) \end{aligned} \quad (5.80)$$

$$\frac{\partial F_{i,j}^{\psi_p}}{\partial \psi_{p_{i+1,j}}} = c_{1n} \frac{T_{i+1,j}}{V_{T_{i+1,j}}} \beta \left(\frac{\eta_1}{V_{T_{i+1,j}}} \right) p_{i+1,j} \quad (5.81)$$

$$\frac{\partial F_{i,j}^{\psi_p}}{\partial \psi_{p_{i-1,j}}} = c_{3n} \frac{T_{i-1,j}}{V_{T_{i-1,j}}} \beta \left(\frac{-\eta_3}{V_{T_{i-1,j}}} \right) p_{i-1,j} \quad (5.82)$$

$$\frac{\partial F_{i,j}^{\psi_p}}{\partial \psi_{p_{i,j+1}}} = v_{1n} \frac{T_{i,j+1}}{V_{T_{i,j+1}}} \beta \left(\frac{\zeta_1}{V_{T_{i,j+1}}} \right) p_{i,j+1} \quad (5.83)$$

$$\frac{\partial F_{i,j}^{\psi_p}}{\partial \psi_{p_{i,j-1}}} = v_{3n} \frac{T_{i,j-1}}{V_{T_{i,j-1}}} \beta \left(\frac{-\zeta_3}{V_{T_{i,j-1}}} \right) p_{i,j-1} \quad (5.84)$$

$$\begin{aligned} \frac{\partial F_{i,j}^{\psi_p}}{\partial \phi_{i,j}} &= c_{1n} \frac{T_{i+1,j}}{V_{T_{i+1,j}}} d\beta \left(\frac{\eta_1}{V_{T_{i+1,j}}} \right) p_{i+1,j} \\ &\quad c_{3n} \frac{T_{i-1,j}}{V_{T_{i-1,j}}} d\beta \left(\frac{-\eta_3}{V_{T_{i-1,j}}} \right) p_{i-1,j} \\ &\quad \frac{T_{i,j}}{V_{T_{i,j}}} p_{i,j} \left\{ c_{1n} \left[d\beta \left(\frac{-\eta_1}{V_{T_{i,j}}} \right) + \beta \left(\frac{-\eta_1}{V_{T_{i,j}}} \right) \right] \right. \\ &\quad \left. + c_{3n} \left[d\beta \left(\frac{\eta_3}{V_{T_{i,j}}} \right) + \beta \left(\frac{\eta_3}{V_{T_{i,j}}} \right) \right] \right\} \\ &\quad v_{1n} \frac{T_{i,j+1}}{V_{T_{i,j+1}}} d\beta \left(\frac{\zeta_1}{V_{T_{i,j+1}}} \right) p_{i,j+1} \\ &\quad v_{3n} \frac{T_{i,j-1}}{V_{T_{i,j-1}}} d\beta \left(\frac{-\zeta_3}{V_{T_{i,j-1}}} \right) p_{i,j-1} \\ &\quad \frac{T_{i,j}}{V_{T_{i,j}}} p_{i,j} \left\{ v_{1n} \left[d\beta \left(\frac{-\zeta_1}{V_{T_{i,j}}} \right) + \beta \left(\frac{-\zeta_1}{V_{T_{i,j}}} \right) \right] \right. \\ &\quad \left. v_{3n} \left[d\beta \left(\frac{\zeta_3}{V_{T_{i,j}}} \right) + \beta \left(\frac{\zeta_3}{V_{T_{i,j}}} \right) \right] \right\} \\ &\quad + \frac{q}{V_{T_{i,j}}} (n_{i,j} \tau_{p_{i,j}} + n_{i,j} \tau_{n_{i,j}}) (n_{i,j} + n_{i,j}) \\ &\quad \left((n_{i,j} + n_{i,j}) \tau_{p_{i,j}} + (p_{i,j} + n_{i,j}) \tau_{n_{i,j}} \right)^2 \\ &\quad \frac{q}{V_{T_{i,j}}} (n_{i,j} p_{i,j} - n_{i,j}^2) (C_p p_{i,j} - C_n n_{i,j}) \end{aligned} \quad (5.85)$$

$$\begin{aligned} \frac{\partial F_{i,j}^{\psi_p}}{\partial \phi_{i+1,j}} &= -c_{1n} \frac{T_{i,j}}{V_{T_{i,j}}} p_{i,j} d\beta \left(\frac{-\eta_1}{V_{T_{i,j}}} \right) \\ &\quad - c_{1n} \frac{T_{i+1,j}}{V_{T_{i+1,j}}} p_{i+1,j} \left[d\beta \left(\frac{\eta_1}{V_{T_{i+1,j}}} \right) + \beta \left(\frac{\eta_1}{V_{T_{i+1,j}}} \right) \right] \end{aligned} \quad (5.86)$$

$$\begin{aligned} \frac{\partial F_{i,j}^{\psi_p}}{\partial \phi_{i-1,j}} &= -c_{3n} \frac{T_{i,j}}{V_{T_{i,j}}} p_{i,j} d\beta \left(\frac{\eta_3}{V_{T_{i,j}}} \right) \\ &- c_{3n} \frac{T_{i-1,j}}{V_{T_{i-1,j}}} p_{i-1,j} \left[d\beta \left(\frac{-\eta_3}{V_{T_{i-1,j}}} \right) + \beta \left(\frac{-\eta_3}{V_{T_{i-1,j}}} \right) \right] \end{aligned} \quad (5.87)$$

$$\begin{aligned} \frac{\partial F_{i,j}^{\psi_p}}{\partial \phi_{i,j+1}} &= -v_{1n} \frac{T_{i,j}}{V_{T_{i,j}}} p_{i,j} d\beta \left(\frac{-\zeta_1}{V_{T_{i,j}}} \right) \\ &- v_{1n} \frac{T_{i,j+1}}{V_{T_{i,j+1}}} p_{i,j+1} \left[d\beta \left(\frac{\zeta_1}{V_{T_{i,j+1}}} \right) + \beta \left(\frac{\zeta_1}{V_{T_{i,j+1}}} \right) \right] \end{aligned} \quad (5.88)$$

$$\begin{aligned} \frac{\partial F_{i,j}^{\psi_p}}{\partial \phi_{i,j-1}} &= -v_{3n} \frac{T_{i,j}}{V_{T_{i,j}}} p_{i,j} d\beta \left(\frac{\zeta_3}{V_{T_{i,j}}} \right) \\ &- v_{3n} \frac{T_{i,j-1}}{V_{T_{i,j-1}}} p_{i,j-1} \left[d\beta \left(\frac{-\zeta_3}{V_{T_{i,j-1}}} \right) + \beta \left(\frac{-\zeta_3}{V_{T_{i,j-1}}} \right) \right] \end{aligned} \quad (5.89)$$

$$\begin{aligned} \frac{\partial F_{i,j}^{\psi_p}}{\partial \psi_{n_{i,j}}} &= \frac{-\frac{q}{V_{T_{i,j}}} (n_{i,j} \tau_{p_{i,j}} + n_{i,j} \tau_{n_{i,j}}) (n_{i,j} + n_{i,j})}{\left((p_{i,j} + n_{i,j}) \tau_{n_{i,j}} + (n_{i,j} + n_{i,j}) \tau_{p_{i,j}} \right)^2} \\ &- \frac{q}{V_{T_{i,j}}} \left(p_{i,j} (C_n n_{i,j} + C_p p_{i,j}) + C_n (n_{i,j} p_{i,j} - n_{i,j}^2) \right) \end{aligned} \quad (5.90)$$

$$\frac{\partial F_{i,j}^{\psi_p}}{\partial \psi_{n_{i+1,j}}} = \frac{\partial F_{i,j}^{\psi_p}}{\partial \psi_{n_{i-1,j}}} = \frac{\partial F_{i,j}^{\psi_p}}{\partial \psi_{n_{i,j+1}}} = \frac{\partial F_{i,j}^{\psi_p}}{\partial \psi_{n_{i,j-1}}} = 0 \quad (5.91)$$

Current Computation and Heat Flow

Once the Smart Newton Engine produces values that meet the specified error condition, phase four, current calculation and temperature computation, is

entered. Like the Vectorized-Gauss-Seidel of phase two, the Heat Flow equation is solved using a linear iteration method. The Step used to acquire the numerical representation of the Heat Flow linear iteration are given below.

$$\begin{aligned} J_{n_{i,j}}^x &= \frac{h_i J_{n_{i+\frac{1}{2},j}} + h_{i-1} J_{n_{i-\frac{1}{2},j}}}{h_i + h_{i-1}} \\ J_{n_{i,j}}^y &= \frac{k_j J_{n_{i,j+\frac{1}{2}}} + k_{j-1} J_{n_{i,j-\frac{1}{2}}}}{k_j + k_{j-1}} \end{aligned} \quad (5.92)$$

$$\begin{aligned} J_{p_{i,j}}^x &= \frac{h_i J_{p_{i+\frac{1}{2},j}} + h_{i-1} J_{p_{i-\frac{1}{2},j}}}{h_i + h_{i-1}} \\ J_{p_{i,j}}^y &= \frac{k_j J_{p_{i,j+\frac{1}{2}}} + k_{j-1} J_{p_{i,j-\frac{1}{2}}}}{k_j + k_{j-1}} \end{aligned} \quad (5.93)$$

$$\begin{aligned} & \frac{2}{h_i + h_{i-1}} \left\{ \frac{\kappa_{i+\frac{1}{2},j}}{h_i} T_{i+1,j} + \frac{\kappa_{i-\frac{1}{2},j}}{h_{i-1}} T_{i-1,j} \right\} \\ & + \frac{2}{k_j + k_{j-1}} \left\{ \frac{\kappa_{i,j+\frac{1}{2}}}{k_j} T_{i,j+1} + \frac{\kappa_{i,j-\frac{1}{2}}}{k_{j-1}} T_{i,j-1} \right\} \\ & \qquad \qquad \qquad + H_{i,j} \\ & = \left[\frac{2}{h_i + h_{i-1}} \left(\frac{\kappa_{i+\frac{1}{2},j}}{h_i} + \frac{\kappa_{i-\frac{1}{2},j}}{h_{i-1}} \right) \right. \\ & \quad \left. + \frac{2}{k_j + k_{j-1}} \left(\frac{\kappa_{i,j+\frac{1}{2}}}{k_j} + \frac{\kappa_{i,j-\frac{1}{2}}}{k_{j-1}} \right) \right] T_{i,j} \end{aligned} \quad (5.94)$$

$$\begin{aligned} & \alpha T_{i+1,j} + \beta T_{i-1,j} + \delta T_{i,j+1} + \gamma T_{i,j-1} + H_{i,j} \\ & \qquad \qquad \qquad = (\alpha + \beta + \delta + \gamma) T_{i,j} \end{aligned} \quad (5.95)$$

$$\begin{aligned}
\alpha &= \frac{2}{h_i + h_{i-1}} \frac{\kappa_{i+\frac{1}{2},j}}{h_i} \\
\beta &= \frac{2}{h_i + h_{i-1}} \frac{\kappa_{i-\frac{1}{2},j}}{h_{i-1}} \\
\delta &= \frac{2}{k_j + k_{j-1}} \frac{\kappa_{i,j+\frac{1}{2}}}{k_j} \\
\gamma &= \frac{2}{k_j + k_{j-1}} \frac{\kappa_{i,j-\frac{1}{2}}}{k_{j-1}}
\end{aligned} \tag{5.96}$$

$$\begin{aligned}
&T_{i,j}^{k+1} = \\
&\frac{\alpha^k T_{i+1,j}^k + \beta^k T_{i-1,j}^k + \delta^k T_{i,j+1}^k + \gamma^k T_{i,j-1}^k + H_{i,j}^k}{\alpha^k + \beta^k + \delta^k + \gamma^k}
\end{aligned} \tag{5.97}$$

$$V_{T_{i,j}} = \frac{k_B T_{i,j}}{q} \tag{5.98}$$

After the temperature is computed, the thermal voltage is calculated and a convergence test is performed. If the convergence test produces errors that are less than the specific maximum error value, output is generated, and the simulation is terminate. Otherwise, the Simulator returns to phase two.

5.4 Chapter Summary

In this chapter the simulation flow process for solving the drift-diffusion heat flow equations was presented. In addition, the numerical details associated with each of these processes and their finite difference representation have been discussed.

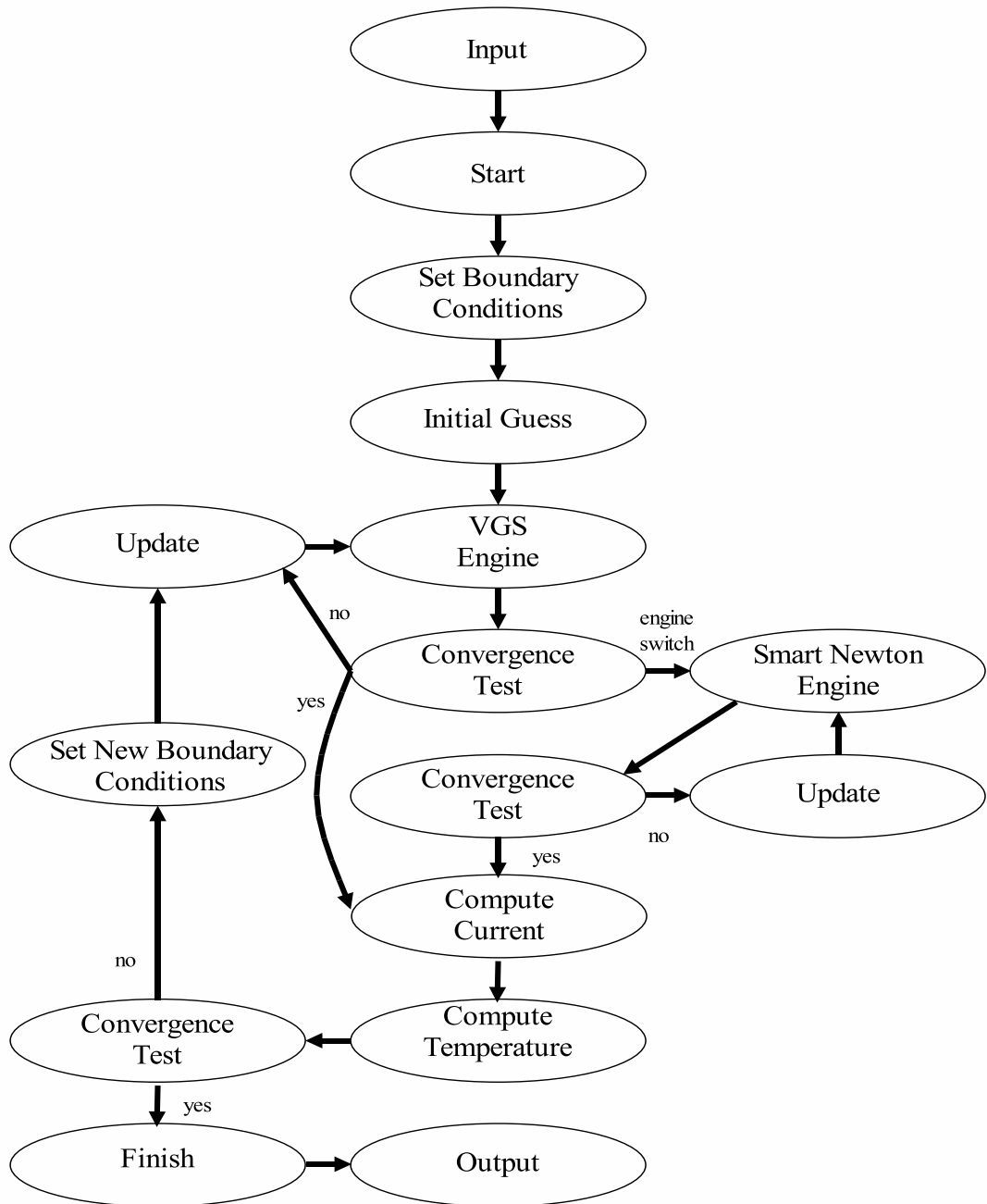


Figure 5.1: Drift-diffusion heat flow simulation flow chart showing the various phases and conditional loops.

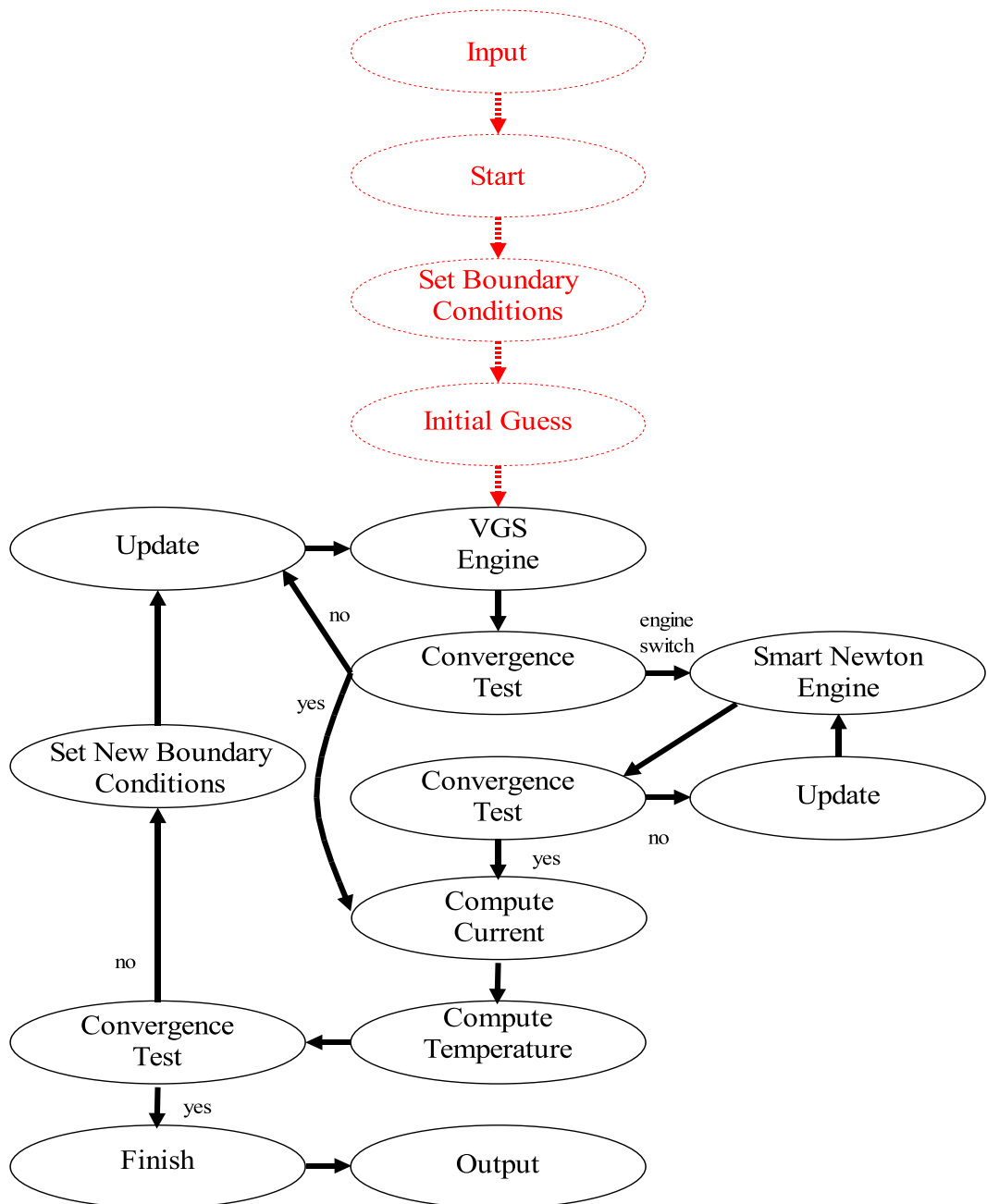


Figure 5.2: Phase 1 - initializing the Simulator. This phase of the simulation process consist of defining the device, setting the boundary condition, and computing the initial guess solution to the drift-diffusion heat flow equations.

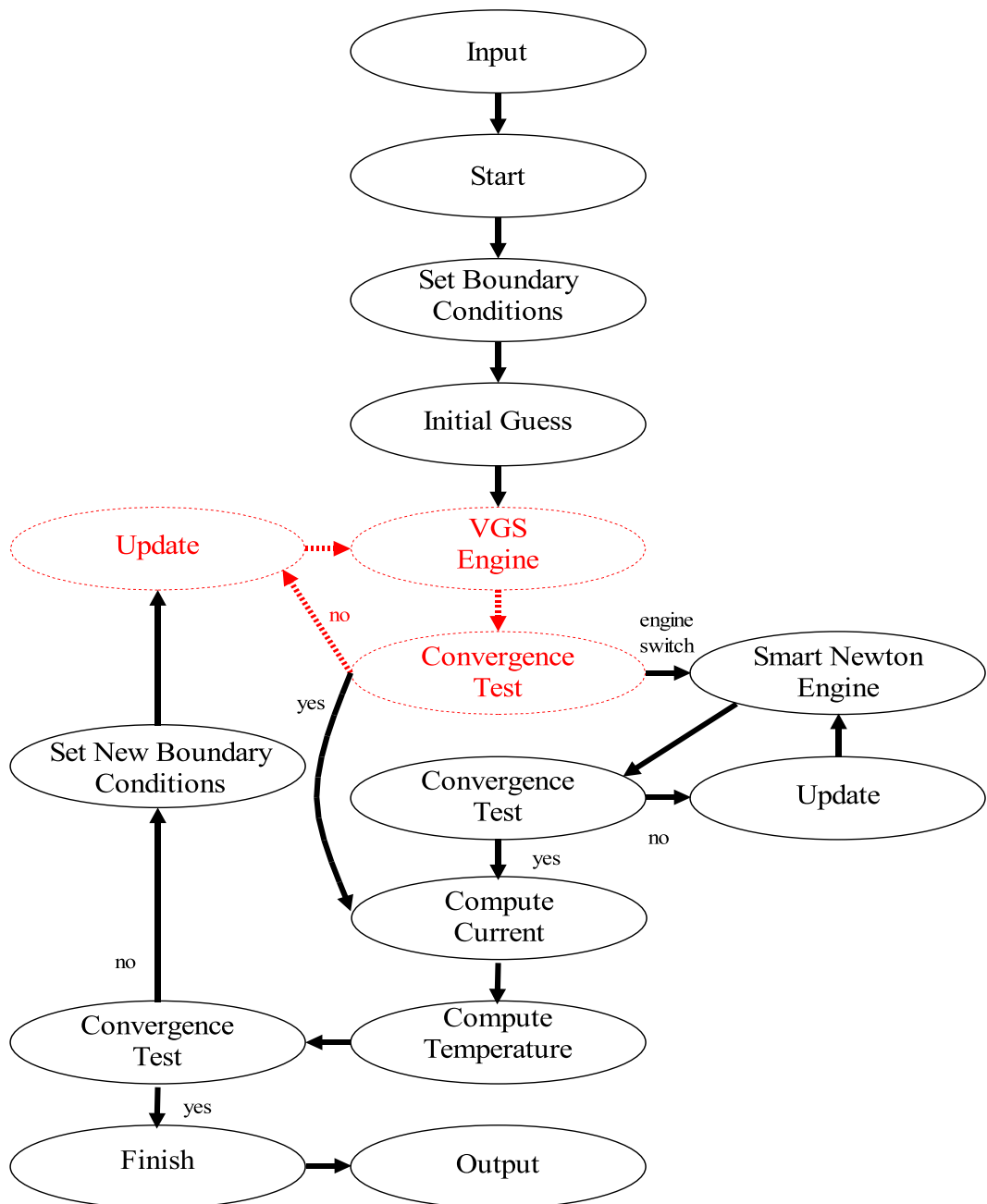


Figure 5.3: Phase 2 - Vectorized Gauss-Seidel Engine. During this phase, linear iteration techniques are used to solve the Poisson equation as well as the electron and hole continuity equations.

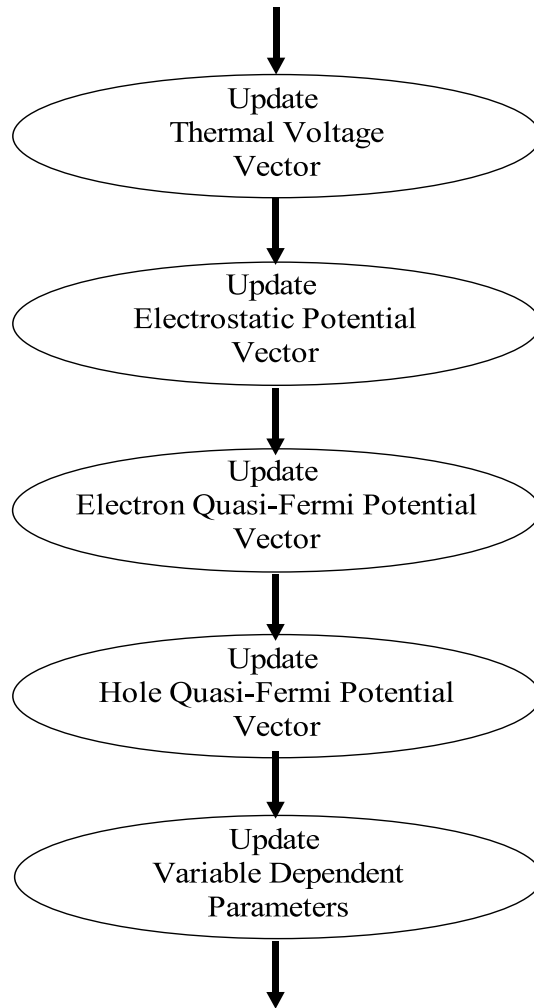


Figure 5.4: The Update Flow is used to reseed the thermal voltage, electrostatic potential, electron and hole quasi-Fermi potentials, and any models that depend on the other values mentioned before entering a computation phase.

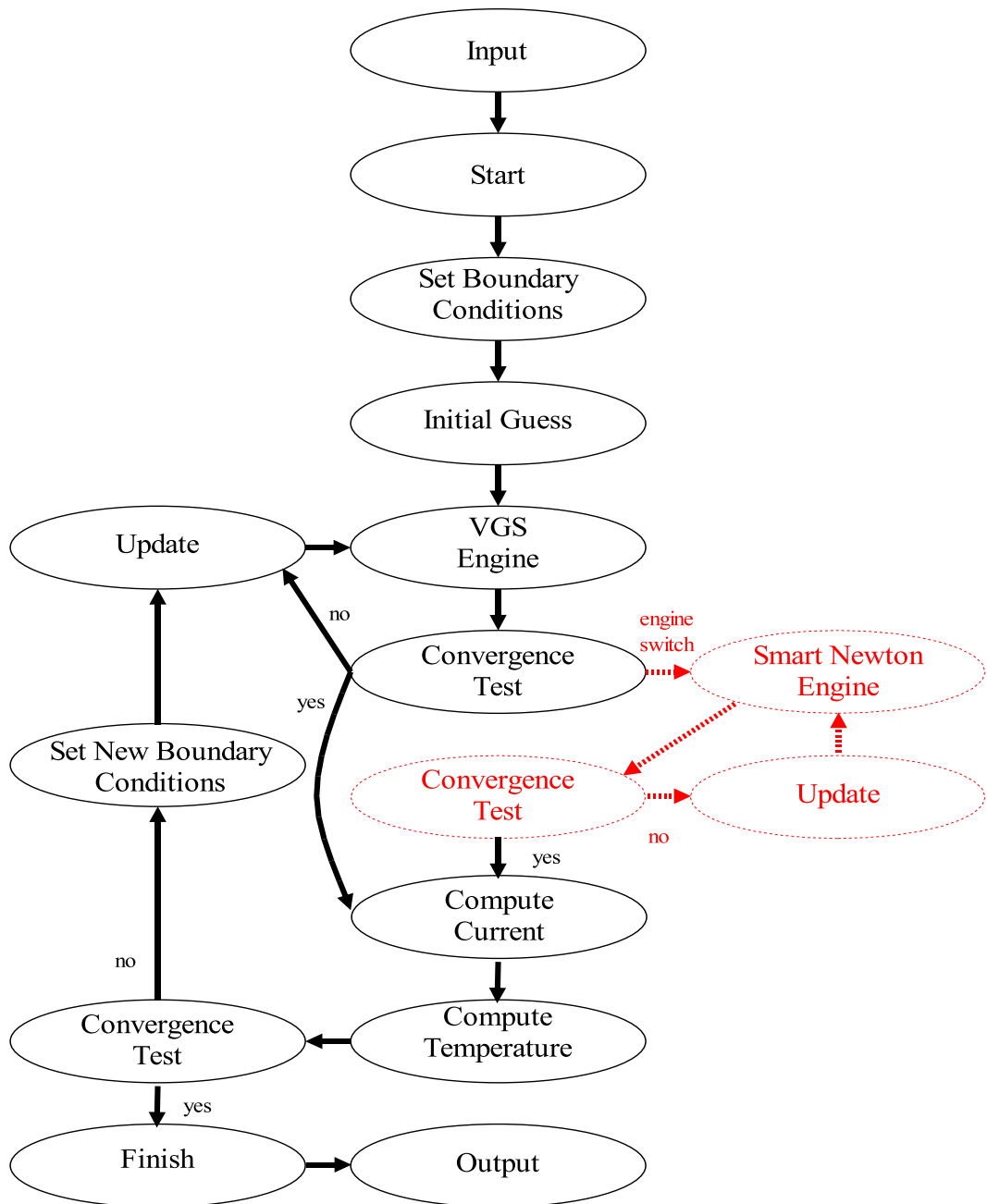


Figure 5.5: Phase 3 - Smart Newton Engine Flow. In this phase traditional drift-diffusion equations are coupled and solved. If the newly computed value at a given mesh point strays drastically from the previous value, the new value is rejected as the old one maintained.

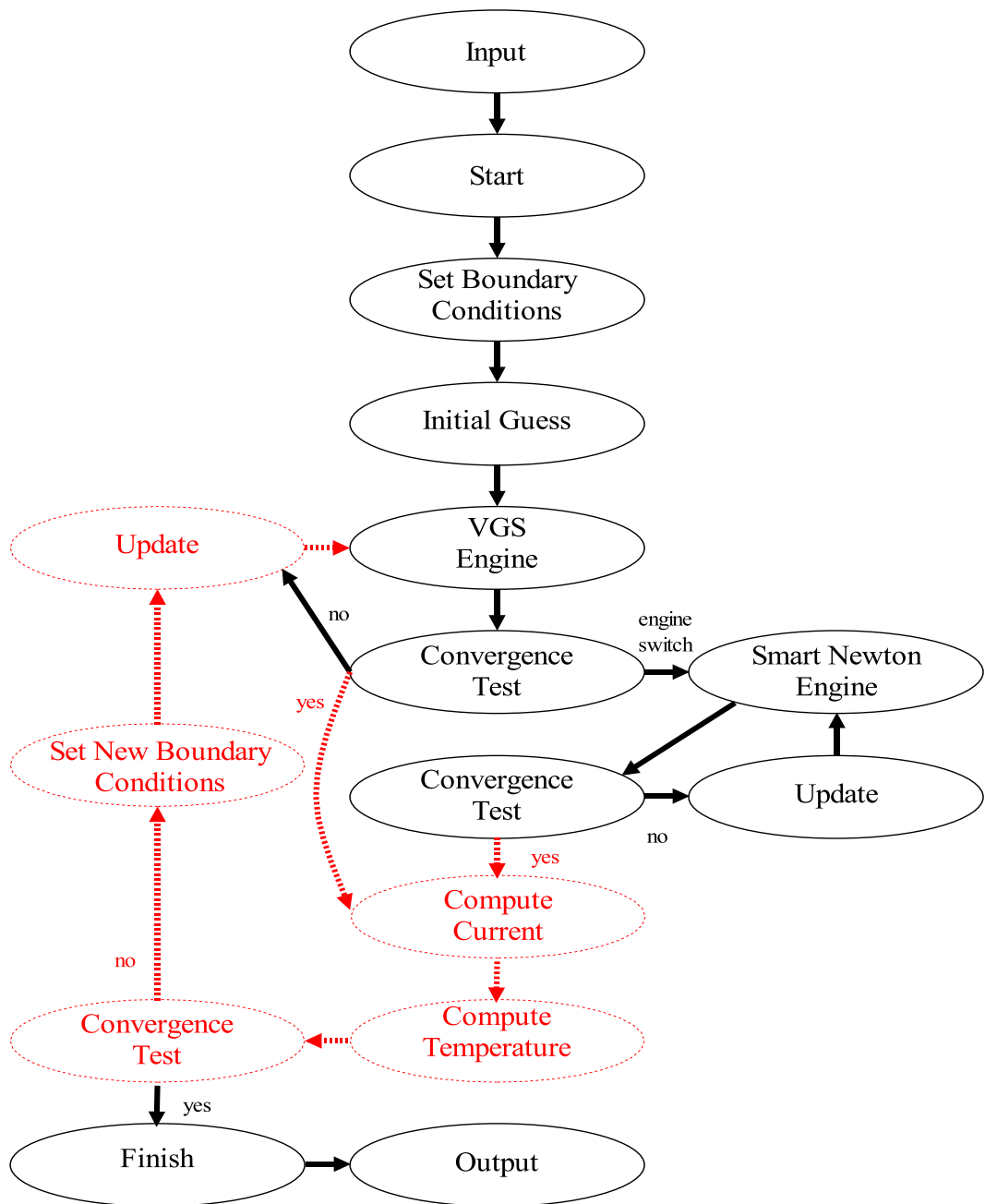


Figure 5.6: Phase 4a - Current Calculation and Heat Flow. During this phase the current and impact ionization rate are computed and the heat flow equation is solved.

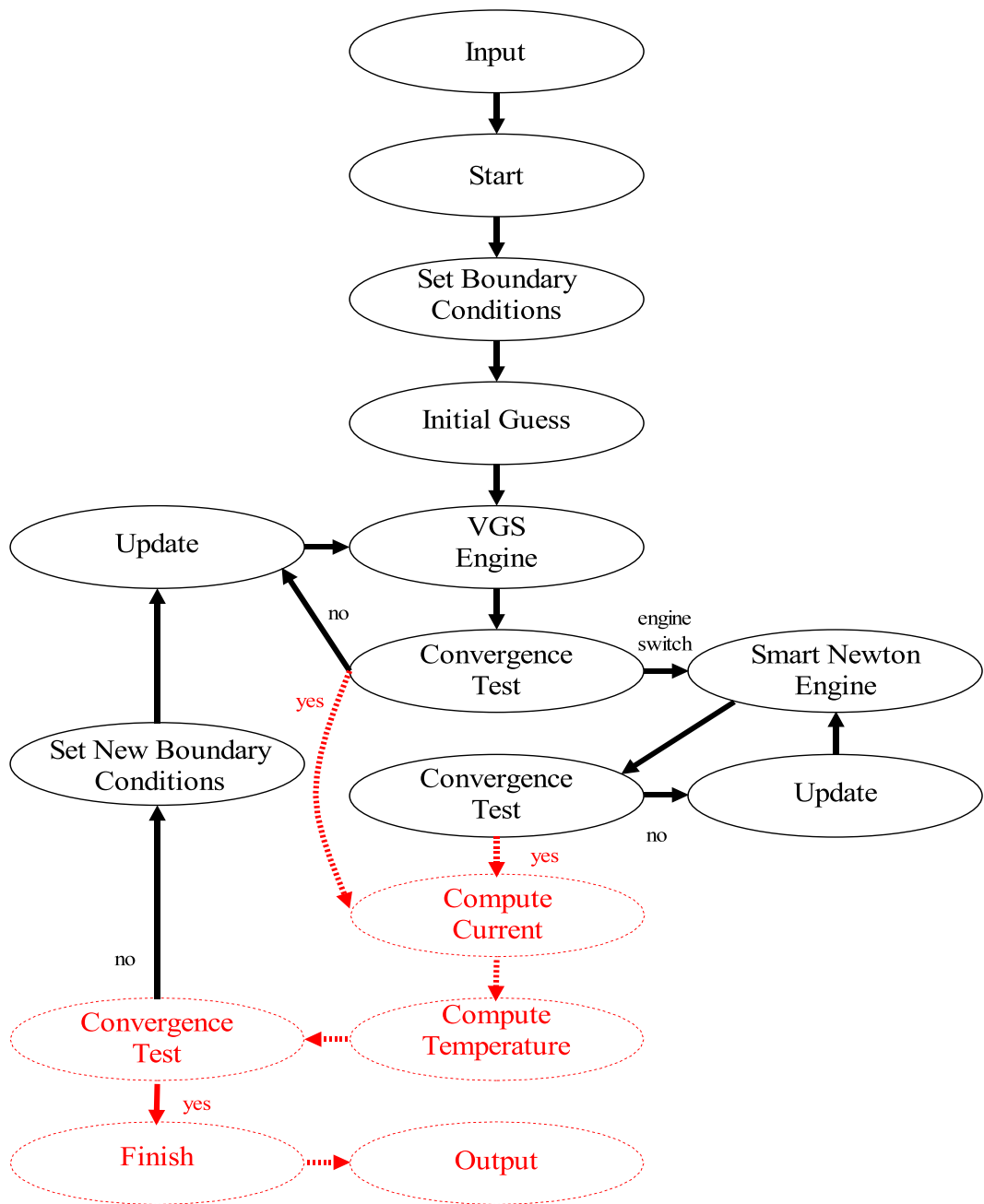


Figure 5.7: Phase 4b - Terminating the Simulation. If all convergence requirements have been achieved, or the maximum number of iterations has been reached, the simulation is terminated.

Chapter 6

Summary and Closing Remarks

In closing I present a short summary of my work and accomplishments in the dissertation. Additionally, I draw conclusions and suggest future work.

6.1 The Method Behind the Madness

Chapters 2 and 4 describe the drift-diffusion heat flow model specialized for silicon carbide MOSFETs. It is here that I first proposed the incorporation of energy and temperature dependent device physics and transport models. This is significant because, to my knowledge, the inclusion of both energy dependence and temperature dependence due to lattice self-heating has never been included in the drift-diffusion set. More important, agreement between experimental and simulated data may have proven to be impossible without the inclusion of these dependencies due to the relationship between temperature, energy, and the occupied trap density. Of equal importance is my implementation of the SiC surface mobility model which separates each of the scattering mechanisms allowing me to observe and directly correlate surface quality to experimental MOSFET performance. This mobility model, together with experimental data, allowed me to isolate and identify

the dominant scattering mechanisms, thus giving fabrication experts much needed knowledge and/or confirmation regarding the focus of their efforts.

Devising a methodology is one thing; implementing it is another. In chapter 5 I presented the process flow for my SiC MOSFET drift-diffusion heat flow simulator that was used to both match current state-of-the-art 6H-SiC MOSFET behavior and predict the performance of next generation devices. My simulator is unique in that it includes all relevant MOSFET scattering processes without blurring the underlying physics; a feature not yet reported in other SiC MOSFET simulation tools. Furthermore, in order to achieve such a task, I had to implore a numerical technique that, in some regard, monitored its own convergence behavior. This was implemented via the Smart Newton solver. The reason for this memory based implementation is found in the fact that numerical approaches to problems involving wide bandgap materials like SiC have a range of values to consider. Nonetheless, this hurdle was also surpassed.

6.2 SiC MOSFET Characterization

I have shown that, by matching experimentally observed electrical characteristics of the devices at both room temperature (Chapter 3) and elevated temperatures (Chapter 4), my simulator can be used to provide insight into the physics behavior of current state-of-the-art silicon carbide devices. This is possible because, using the methodology mentioned in the previous section, I was able to more accurately extract the interface trap physical attributes of the devices stud-

ied. Since interface charge scattering is the dominant degradation mechanism of many SiC MOSFETs, being able to accurately model the behavior of this charge in a tractable manor is of great value. For the first time, a simulation tool has used a control set of experimental 6H-SiC MOSFETs to extract physical surface attributes that reasonably characterize a device lot of extremely volatile behavior.

Interested in the possibility of using SiC MOSFETs as a basis of integrated power electronic circuit design, I also examined the performance and scalability of 6H-SiC MOSFET as their surface quality improves and its ambient temperature increases (from room temperature to 200 Celsius). My results (Chapter 4) show that, though it is not the dominant cause of performance degradation in the state-of-the-art devices studied, surface roughness is indeed the next contender. As the interface charge densities reduce, surface roughness begins to display its degradation potential, especially when gate oxide thickness begins to shrink. Furthermore, my results indicate that the impact of surface roughness induced degradation is much worse than that of interface charge because of its square law dependence on applied electric field. Several years ago a debate arose as to whether the performance degradation seen in SiC MOSFETs was a result of interface charge or surface roughness. Though many seemed to quietly lean towards interface charge, no definitively answer was reached. I believe that my work in this dissertation has not only answered the aforementioned question (in favor of interface charge) but has also asked - and quantitatively answered - two others, "What should our interface charge reduction goal be?" and "When do we need to worry at the effects of

surface roughness?”

6.3 Closing Remarks and What’s Left to Do

In this work I have taken a detailed look at the behavior of 6H-SiC MOSFETs and examined the reasons for their unexpectedly poor performance. From this study I have been able to determine which factors contribute to their degradation. Now that the causes have been identified, directed efforts can be made towards improvement, but this is not enough. In order for SiC MOSFETs to have a significant impact on the CMOS revolution, they must demonstrate improved performance with longevity. As a result, long term transient simulations with proper modelling must be designed, implemented, and performed. Only after the long term reliability has been investigated will the future and fate of SiC MOSFET technology be determined.

In closing I would like to say thank you to all of those who have taken the time to read my work. I hope that this has been somewhat educational and mildly entertaining.

REFERENCES

- [1] S. K. Powell, N. Goldsman, J. M. McGarrity, J. Bernstein, A. Lelis, and C. J. Scozzie, “Physics-based Numerical Modeling and Characterization of 6H-Silicon-Carbide Metal-Oxide-Semiconductor Field-effect Transistors,” *Journal of Applied Physics*, vol. 92, no. 7, pp. 4053–61, 2002.
- [2] E. Dubaric, M. Hjelm, H.-E. Nilsson, and P. K. C. S. Petersson, “The Effects of Different Transport Models in Simulations of a 4H-SiC Ultra Short Channel MOSFET,” in *ICM’99: The Eleventh International Conference on Microelectronics*, 1999.
- [3] J. B. Roldán, F. Gámiz, and J. A. López-Villanueva, “A Detailed Simulation Study of the Performance of β -Silicon Carbide MOSFETs and a Comparison with their Silicon Counterparts,” *Semiconductor Science and Technology*, vol. 12, pp. 655–61, 1997.
- [4] F. Nallet, A. Sénès, D. Planson, M. L. Locatelli, J. P. Chante, and D. Renault, “Electrical and Electrothermal 2D Simulations of 4H-SiC High Voltage Current Limiting Device for Serial Protection Application,” in *2000 International Symposium on Power Semiconductor Devices and IC’s*, pp. 287–90, 2000.

- [5] Y. Wang and K. F. Brennan, "Semiclassical Study of the Wave Vector Dependence of the Interband Impact Ionization Rate in Bulk Silicon," *Journal of Applied Physics*, vol. 75, no. 1, p. 313, 1994.
- [6] C. J. Scozzie, F. B. McLean, and J. M. McGarrity, "Modeling the Temperature Response of 4H Silicon Carbide Junction Field-Effect Transistors," *Journal of Applied Physics*, vol. 81, p. 7687, 1997.
- [7] N. S. Saks, S. S. Mani, and A. K. Agarwal, "Interface Trap Profiles Near the Band Edges in 6H-SiC MOSFETs," *Materials Science Forum*, vol. 338-342, pp. 1113–16, 2000.
- [8] M. Bassler, V. V. Afanas'ev, G. Pensi, and M. Schulz, "Electrically Active Traps at the 4H-SiC/SiO₂ Interface Responsible for the Limitation of the Channel Mobility," *Materials Science Forum*, vol. 338-342, pp. 1065–68, 2000.
- [9] J. N. Shenoy, G. L. Chindalore, M. R. Melloch, J. J. A. Cooper, J. W. Palmour, and K. G. Irvine, "Characterization and Optimization of the SiO₂/SiC Metal-oxide Semiconductor Interface," *Journal of Electronic Materials*, vol. 24, no. 4, pp. 303–9, 1995.
- [10] J. N. Shenoy, M. K. Das, J. J. A. Cooper, and M. R. Melloch, "Effects of Substrate Orientation and Crystal Anisotropy on the Thermal Oxidized SiO₂/SiC Interface," *Journal of Applied Physics*, vol. 79, no. 6, pp. 3042–45, 1996.

- [11] Y. Shi, Y. Luo, J. Campi, F. Yan, Y. K. Lee, and J. H. Zhao, "Effect of PMA on Effective Fixed Charge in Thermally Grown Oxide on 6H-SiC," *Electronics Letters*, vol. 34, no. 7, pp. 698–700, 1998.
- [12] C. J. Scozzie, A. J. Lelis, and F. B. McLean, "Mobility in 6H-SiC n-Channel MOSFETs," *Material Science Forum*, vol. 338-342, p. 1121, 2000.
- [13] V. R. Vathulya and M. H. White, "Characterization of Inversion and Accumulation Layer Electrons Transport in 4H and 6H-SiC MOSFETs on Implanted P-Type Regions," *IEEE Transactions on Electron Devices*, vol. 47, no. 11, 2000.
- [14] H. Yano, F. Katafuchi, T. Kimoto, and H. Matsunami, "Effects of Wet Oxidation/Anneal on Interface Properties of Thermally Oxidized SiO₂/SiC MOS System and MOSFETs," *IEEE Transactions on Electron Devices*, vol. 46, no. 3, pp. 504–10, 1999.
- [15] I. W. E. Wagner and M. H. White, "Characterization of Silicon Carbide (SiC) Epitaxial Channel Mosfets," *IEEE Transactions on Electronic Devices*, vol. 47, no. 11, pp. 2214–20, 2000.
- [16] U. Schmid, S. T. Sheppard, W. Wondrak, and E. Niemann, "Electrical Characterization of 6H-SiC Enhancement-Mode Mosfets at high Temperatures," *Materials Science and Engineering*, vol. B61-62, pp. 493–96, 1999.

- [17] R. Schorner, P. Friedrichs, and D. Peters, “Detailed Investigation of N-Channel Enhancement 6H-SiC MOSFETs,” *IEEE Transactions on Electron Devices*, vol. 46, no. 3, pp. 533–41, 1999.
- [18] U. Schmid, S. T. Sheppard, and W. Wondrak, “Circular and Linear Enhancement-Mode 6H-SiC MOSFETs at High Temperatures Applications,” *Journal of Electronic Materials*, vol. 23, no. 3, pp. 148–53, 1999.
- [19] S. Selberherr, *Analysis and Simulation of Semiconductor Devices*. Wien: Springer-Verlag, 1984.
- [20] S. M. Sze, *Physics of Semiconductor Devices*. New York: John Wiley & Sons, 1981.
- [21] M. Bakowski, U. Gustafsson, and U. Lindefelt, “Simulation of SiC High Power Devices,” *Phys. Stat. Sol. (a)*, vol. 162, pp. 421–47, 1997.
- [22] Y.-Z. Chen and T.-W. Tang, “Impact Ionization Coefficient and Energy Distribution Function at High Fields in Semiconductors,” *Journal of Applied Physics*, vol. 65, no. 11, pp. 4279–4286, 1989.
- [23] M. E. Levinshtein, S. L. Rumyantsev, and M. S. Shur, *Properties of Advanced Semiconductor Materials: GaN, AlN, InN, BN, SiC, SiGe*. New York: John Wiley & Sons, Inc., 2001.

- [24] R. Raghunathan and B. J. Baliga, "Temperature Dependence of Hole Impact Ionization Coefficients in 4H and 6H-SiC," *Solid-State Electronics*, vol. 43, no. 2, pp. 199–211, 1999.
- [25] C. Lombardi, S. Manzini, A. Saporito, and M. Vanzi, "A Physically Based Mobility Model for Numerical Simulation of Nonplanar Devices," *IEEE Transactions on CAD*, vol. 7, pp. 1164–1171, 1988.
- [26] C. Jacoboni and L. Reggiani, "The Monte Carlo Method for the Solution of Charge Transport in Semiconductors with Applications to Covalent Materials," *Reviews of Modern Physics*, vol. 55, no. 3, pp. 645–705, 1983.
- [27] G. Baccarani and M. R. Wordeman, "An Investigation of Steady-state Velocity Overshoot in Silicon," *Solid-State Electron.*, vol. 28, pp. 407–416, 1985.
- [28] K. K. Thornber, "Relation of Drift Velocity to Low-Field Mobility and High-Field Saturation Velocity," *Journal of Applied Physics*, vol. 51, no. 4, 1980.
- [29] M. Lundstrom, *Fundamentals of Carrier Transport*. Modular Series on Solid State Devices, New York: Addison-Wesley, 1990.
- [30] D. Caughey and R. Thomas, "Carrier Mobilities in Silicon Empirically Related to Doping and Field," *Proceedings IEEE* 52, 1967.
- [31] R. Mickevičius and J. H. Zhao, "Monte Carlo Study of Transport in SiC," *Journal of Applied Physics*, vol. 83, no. 6, 1998.

- [32] G. Pennington and N. Goldsman, “Empirical Pseudopotential Band Structure of 3C, 4H, and 6H SiC Using Transferable Semiempirical Si and C Model Potentials,” *Phy. Rev. B*, vol. 64, 2001.
- [33] C. Sah, T. Ning, and L. Tschopp, “The Scattering of Electrons by Surface Charges and by Lattice Vibrations at the Silicon-Silicon Dioxide Interface,” *Surface Science*, vol. 32, pp. 561–575, 1972.
- [34] A. Hiroki, S. Odanaka, K. Ohe, and H. Esaki, “A mobility model for submicrometer MOSFET simulations including hot-carrier-induced device degradation,” *IEEE Trans. Electron Devices*, vol. 35, no. 9, pp. 1487–1493, 1988.
- [35] S. Schwarz and S. Russek, “Semi-empirical equations for electron velocity in silicon: Part II-MOS inversion layer,” *IEEE Transactions on Elec. Dev.*, vol. 30, pp. 1634–1639, 1983.
- [36] A. Harstein, T. H. Ning, and A. B. Fowler, “Electron Scattering in Silicon Inversion Layers by Oxide and Surface Roughness,” *Surface Science*, vol. 58, pp. 178–81, 1976.
- [37] W. Liang, N. Goldsman, I. Mayergoyz, and P. Oldiges, “2-DMOSFET Modeling Including Surface Effects and Impact Ionization by Self-Consistent Solution of the Boltzmann, Poisson and Hole-Continuity Equations,” *IEEE Transactions on Elec. Dev.*, vol. 44, pp. 257–276, 1997.

- [38] R. P. Joshi, “Monte Carlo calculations of the temperature and field-dependent electron transport parameters for 4H-SiC,” *J. Appl. Phys.*, vol. 78, pp. 5518–5521, 1995.
- [39] N. Goldsman, L. Henrickson, and J. Frey, “A Physics-Based Analytical/Numerical Solution to the Boltzmann Transport Equation for Use in Device Simulation,” *Solid-State Electronics*, vol. 34, no. 4, pp. 389–396, 1991.
- [40] G. Groeseneken, H. Maes, N. Beltran, and R. F. DeKeersmaecker, “A Reliable Approach to Charge-Pumping Measurements in MOS Transistors,” *IEEE Transactions on Electron Devices*, vol. ED-31, 1984.
- [41] C. J. Scozzie and J. M. McGarrity, “Effects of Interface-Trapped Charge on the SiC MOSFET Characteristics,” *Proceedings: 4th International High Temperature Electrons Conference*, p. 23, 1998.
- [42] EnvironmentalChemistry.com. <http://environmentalchemistry.com/yogi/periodic/Mo.htm> 2002.
- [43] R. Muller and T. Kamins, *Device Electronics for Integrated Circuits*. New York: John Wiley & Sons, 1986.
- [44] S. K. Powell. Master of Science Thesis, University of Maryland, College Park, 2000.

- [45] N. S. Saks, S. S. Mani, and A. K. Agarwal, "Interface Trap Profile Near the Band Edges at the 4H-SiC/SiO₂ Interface," *Applied Physics Letters*, vol. 76, no. 16, pp. 2250–2, 2000.
- [46] W. Shockley, *Electrons and Holes in Semiconductors*. Princeton, NJ: D. Van Nostrand, 1950.
- [47] L. A. Lipkin, D. B. S. Jr., and J. W. Palmour, "Low Interface State Density Oxides of P-Type SiC," in *IOP Poroc. Inter. Conf. on Silicon Carbide III-nitrides and Related Materials*, 1997.
- [48] G. K. Wachutka, "Rigorous Thermodynamic Treatment of Heat Generation and Conduction in Semiconductor Device Modeling," *IEEE Transactions on Computer-Aided Design of Integrated Circuits and Systems*, vol. 9, no. 11, pp. 1141–9, 1990.
- [49] D. A. Dallman and K. Shenai, "Scaling Constraints Imposed by Self-heating in Submicron SOI MOSFET's," *IEEE Transactions on Electron Devices*, vol. 42, no. 3, pp. 489–96, 1995.
- [50] P. D. Maycock, "Thermal Conductivity of Silicon, Germanium, III-V Compounds and III-V Alloys," *Solid-State Electronics*, vol. 10, pp. 161–8, 1967.
- [51] H. Momosa, M. Ono, T. Yoshitomi, T. Ohguro, S. Nakamura, M. Saito, and H. Iwai, "1.5 nm Direct Tunelling Gate Oxide Si MOSFETS," *IEEE Transactions on Electron Devices*, vol. ED-43, no. 8, p. 1233, 1996.

- [52] M. P. Lam and K. T. Kornegay, "Punchthrough Behavior in Short Channel NMOS and PMOS 6H-Silicon Carbide Transistors at Elevated Temperatures," *IEEE Transactions on Components and Packaging Technology*, vol. 22, no. 3, pp. 433–38, 1999.
- [53] C. C. McAndrew, K. Singhal, and E. L. Heasell, "A Consistent Nonisothermal Extension of the Scharfetter-Gummel Stable Difference Approximation," *IEEE Electron Device Letters*, vol. EDL-6, no. 9, pp. 446–7, 1985.
- [54] D. L. Scharfetter and H. K. Gummel, "Large-Scale Analysis of a Silicon Read Diode Oscillator," *IEEE Trans. Electron Devices*, vol. ED-16, p. 64, 1969.
- [55] Q. Lin, N. Goldsman, and G.-C. Tai, "Highly Stable and Routinely Convergent 2-Dimensional Hydrodynamic Device Simulation," *Solid State Electronics*, vol. 37, pp. 899–908, 1994.
- [56] W. Liang, N. Goldsman, and I. Mayergoyz, "Hydrodynamic Device Simulation Using New State Variables Tailored for a Gummel Iterative Approach," *Solid State Electronics*, vol. 39, pp. 1213–20, 1996.
- [57] C. E. Korman and I. D. Mayergoyz, "A Globally Convergent Algorithm for the Solution of the Steady-State Semiconductor Device," *Journal of Applied Physics*, vol. 68, no. 3, p. 1324, 1990.